University of Alberta

Transient Streaming Potential and Streaming Current Phenomena in Finite Length Microchannels and Structured Porous Media

by

Ali Mansouri ©

A thesis submitted to the Faculty of Graduate Studies and Research in partial fulfillment of the requirements for the degree of **Doctor of Philosophy.**

Department of Mechanical Engineering

Edmonton, Alberta
Spring 2008

Library and
Archives Canada

Published Heritage
Branch

395 Wellington Street
Ottawa ON K1A 0N4
Canada

Bibliothèque et
Archives Canada

Direction du
Patrimoine de l'édition

395, rue Wellington
Ottawa ON K1A 0N4
Canada

Your file Votre référence
ISBN: 978-0-494-45563-0
Our file Notre référence
ISBN: 978-0-494-45563-0

NOTICE:
The author has granted a non-exclusive license allowing Library and Archives Canada to reproduce, publish, archive, preserve, conserve, communicate to the public by telecommunication or on the Internet, loan, distribute and sell theses worldwide, for commercial or non-commercial purposes, in microform, paper, electronic and/or any other formats.

The author retains copyright ownership and moral rights in this thesis. Neither the thesis nor substantial extracts from it may be printed or otherwise reproduced without the author's permission.

AVIS:
L'auteur a accordé une licence non exclusive permettant à la Bibliothèque et Archives Canada de reproduire, publier, archiver, sauvegarder, conserver, transmettre au public par télécommunication ou par l'Internet, prêter, distribuer et vendre des thèses partout dans le monde, à des fins commerciales ou autres, sur support microforme, papier, électronique et/ou autres formats.

L'auteur conserve la propriété du droit d'auteur et des droits moraux qui protège cette thèse. Ni la thèse ni des extraits substantiels de celle-ci ne doivent être imprimés ou autrement reproduits sans son autorisation.

In compliance with the Canadian Privacy Act some supporting forms may have been removed from this thesis.

While these forms may be included in the document page count, their removal does not represent any loss of content from the thesis.

Conformément à la loi canadienne sur la protection de la vie privée, quelques formulaires secondaires ont été enlevés de cette thèse.

Bien que ces formulaires aient inclus dans la pagination, il n'y aura aucun contenu manquant.

Canada

ABSTRACT

The objectives of this thesis are (1) to provide a comprehensive understanding of transient behavior and evolution of streaming potential phenomena in a finite length circular cylindrical microchannel, (2) to propose an equivalent electrical analogy of a finite length microchannel and to reduce the complexities associated with solving the coupled set of transient Navier-Stokes and Poisson-Nernst-Planck equations to solving a simple electrical analogy, (3) to elaborate on issues related with streaming current and streaming potential measurements in porous media and (4) to study the electrokinetic energy conversion in a multi microchannel array that was coated with a nano layer of gold on both sides (Nanogold Electrodes).

A time-dependent numerical model governed by Navier-Stokes and Poisson-Nernst-Planck equations was developed and solved for a finite length microchannel domain. This model addresses the transient behavior and evolution of streaming potential in a finite length microchannel and clearly shows how and where an electrokinetic flow influences ions concentration during the evolution of streaming potential. The analysis of streaming potential was continued by carefully following the transient behavior of convection, migration and net currents. Based on unsteady characteristics of streaming current, capacitance and electrical resistance a parallel resistive-capacitive circuit to a DC current source was proposed as an equivalent electrical analogy of a finite length microchannel. The appropriateness of electrical analogy was examined and comparisons were made between charging behavior of a parallel plate capacitor and a finite length microchannel. In order to use the electrical analogy independently, sub-models were developed for current source, capacitive and resistive elements employing dimensional analysis.

On the experimental side, in order to determine interfacial characteristics, streaming potential and streaming current techniques were studied and their benefits and drawbacks were examined. A custom experimental apparatus was employed to explore the consequence of changing the number of microchannels, electrolyte, placement and material of electrodes while using these techniques. Two types of electrodes (platinized platinum and silver mesh) served as conducting probes to measure either electrical potential or current. Experimental observations were discussed and interpreted by aid of the equivalent electrical analogy. The proposed electrical analogy describes a general electrokinetic flow through porous media that is coupled with an external circuit to mimic and explain physical phenomena at electrodes and nature of external electrical devices.

Finally, an extended study on electrokinetic energy conversion was made. A specifically made microchannel array coated with a nano layer of gold (Nanogold electrodes) was used in this work. Due to polarization and failure of Nanogold electrodes in direct streaming current experiments, practical ways of streaming current measurements in porous media were proposed.

Dedicated to my parents;

Hassan and Zahra

ACKNOWLEDGEMENTS

The work on this thesis has been an inspiring, often exciting, sometimes challenging, but always an interesting experience. It has been made possible by many other people, who have supported me.

I am very grateful to my supervisors Prof. **Larry Kostiuk** and Prof. **Subir Bhattacharjee** who have given me the chance to participate in several interesting research projects and attend various international conferences. They have been supporting me with their encouragement and many fruitful discussions. I would also like to express my gratitude to Prof. Daniel Kwok presently at University of Calgary for his advice. The close cooperation with F. Lu, K. Isaacson, C. Haung, C. Scheuerman, A. Mahmoodi and A. Jafarnejad was a great experience. I thank Tery Nord, Greg Miller and other people who made my experimental apparatus and supported me in the workshop during my program. I am also thankful to my supervisors for arranging my defence and reading my thesis. The committee members were of a great help and support; Dr.Carlos Lange, Dr.Payam Rahimi, Dr.Charles Lucy and Dr.Eric M. V. Hoek.

Financial supports from Queen Elizabeth II doctoral scholarship, teaching and research assistantships, travel grants; education abroad program in Germany and Mary Louise Imrie Graduate Student award and Iranian Ministry of Science and Technology studentship are also acknowledged.

At the end, my deepest gratitude to my lovely parents, brothers and sisters; Hassan, Zahra, Shahram, Shermin, Amir and Mahtab.

Table of Contents

1 Introduction **1**

1.1 Background 2

1.1.1 Low Reynolds Number Flows 2

1.1.2 Continuum Approach, Is It Valid in Microfluidics ? . . . 2

1.1.3 The Electric Double Layer and Boltzmann Distribution . 3

1.1.4 The ζ potential 7

1.2 Electrokinetic Flow 8

1.2.1 Streaming Current 11

1.2.2 Streaming Potential 13

1.3 Objectives and Scope of the Thesis 17

1.4 Organization of the Thesis 18

2 Evolution of Streaming Potentials in a Finite Length Microchannel: A Transient Study **20**

2.1 Introduction 20

2.2 Problem Statement 25

2.2.1 Geometry 25

2.2.2 Governing Equations 26

2.2.3 Non-Dimensional Equations 29

2.2.4 Boundary and Initial Conditions 30

2.3 Numerical Methodology and Validation 33
2.3.1 Numerical Solution Methodology 33
2.3.2 Analytical Model for Low Surface Potentials 34
2.3.3 Comparison of Numerical and Analytical Results 37
2.4 Development of Streaming Potential: Transient Study 43
2.4.1 Transient Electrochemical Transport Behavior 43
2.4.2 Ion Concentration Variation with Time 49
2.5 Effects of Surface Charge Variation of Microchannel Walls on Streaming Potentials 52
2.6 Conclusions 55

3 Transient Currents, Capacitance and Electrical Analogy of a Finite Length Microchannel 58
3.1 Introduction 58
3.2 Geometry 60
3.2.1 Governing Equations, Boundary and Initial Conditions . 60
3.3 Current, Net Transported Charge, and Capacitance 63
3.4 Numerical Methodology and Validation 66
3.4.1 Methodology 66
3.4.2 Validation 67
3.5 Results and Discussions 68
3.5.1 Behavior of Transient Currents; convection, migration and net currents 69
3.5.2 Equivalent Electrical Analogy 74
3.5.3 Parametric Study of Net Transient Current 78
3.5.4 Sub-Models for Capacitance, Convection Current and Resistance 81

3.6 Conclusions 89

4 Interpretations of Streaming Current and Potential Measurements in a Multi Microchannel Array: An Electrical Analogy Approach 91

4.1 Introduction 91

4.2 Electrical Analogy of a Multi Microchannel Array 93

4.2.1 Current Source: A Parallel Network of Microchannels . . 94

4.2.2 Capacitance, Resistance and Conduction Current 95

4.2.3 Electrodes 96

4.2.4 Measuring Electrical Potentials and Currents 99

4.3 Experimental Section 100

4.3.1 The Setup; Multi Microchannel Cell 100

4.3.2 Flow System 105

4.3.3 Measurement System 106

4.3.4 Working Electrolytes 107

4.3.5 Experimental Procedure 107

4.4 Results and Discussions 109

4.4.1 Validation Tests 109

4.4.2 Effect of Electrode Material, Surface Area and Location on the Measured Electrical Properties in a Multi Microchannel Array 109

4.4.3 Effect of Electrode Material, Surface Area and Location on the Measured Electrical Properties in Single Microchannels 113

4.5 Conclusions 116

5 Nanogold Electrodes: Characterization and its Impact on Streaming Current Devices 117
5.1 Introduction 117
5.2 Experimental Apparatus 119
5.3 Electrical Analogy of a Streaming Current Device 121
5.3.1 Estimation of a Multi Microchannel Array Capacitance . 124
5.3.2 Estimation of a Multi Microchannel Array Electrical Resistance 125
5.4 Capacitance and Resistance of Nanogold Electrodes 128
5.5 Estimation of Streaming Currents in a Multi Microchannel Array 131
5.6 Energy Conversion in a Streaming Current Device 136
5.7 Conclusions 139

6 Summary and Future Work 141
6.1 Summary 141
6.2 Future Work 142
6.2.1 Incorporation of Electrodes into Numerical Model 142
6.2.2 On the Electrical Analogy of Electrodes 142
6.2.3 Estimation of Streaming Currents using Magnetic Fields 143
6.2.4 Streaming Current Devices: What is next ? 144

Bibliography 146

List of Tables

2.1 Nondimensional and scaled parameters 28

3.1 Parametric study on five non-dimensional groups; L/a, Re, κa, $\frac{-e\zeta}{kT}$ and Sc for a single finite length microchannel. In all simulations a; microchannel radius kept constant (0.5 μm) and the rest of information extracted from numerical code. 69

5.1 Characteristics of NGEs and multi microchannel array for three different electrolytes. R and C represent the total resistance and total capacitance of the microchannel array. R_t and C_t are the corresponding total resistance and capacitance of NGEs. $R_{res,t}$ is the total bulk electrolyte resistance between NGEs and multi microchannel array. τ is the time constant of decay of current obtained from experimental data. 130

5.2 Experimental data obtained by NGEs for various electrolytes. Values are average of four successive measurements. Streaming potentials/currents were measured after the interface between liquid-solid surface reached the equilibrium state. Steady state streaming currents and potential were reported. Maximum of power was estimated on the basis of external currents and streaming potentials. Efficiency was estimated based on the traditional definition of efficiency; $\eta=\frac{Electricalwork}{Flowwork}$ 137

LIST OF FIGURES

1.1 Schematic of Electrical Double Layer: (Left) Distribution of ions next to a negatively charged surface; Stern layer and diffuse layer are shown. (Right) A negative potential profile from a negatively charged surface towards the bulk, showing the ζ potential on the shear plane. Debye length; represents the thickness of electrical double layer and is in the order of a few hundreds nano meters (reproduced from ref. [1]) 6

1.2 Qualitative comparison of velocity, free charge density, streaming current and conduction current profiles for a microchannel with κa = 1, 5 and 25 in a steady state flow condition. The first row of the graph shows the parabolic velocity profiles induced by pressure driven flow in the microchannels; zero velocity at the wall (no-slip boundary condition) and maximum velocity at the center. Velocity profiles as expected are similar in different κa. In the second row, a negatively charged surface (ψ = -25 mV) attracts the counter-ions and repels the co-ions. In the third row, streaming current profile which is the product of free charge density and velocity. In large κa streaming currents are negligible and limited to transport of ions next to the wall. The last row represents the conduction current profiles. Since the electrical resistance of the double layer is relatively lower than bulk electrolyte, the conduction currents migrate through Stern and diffuse layers next to the charged wall. 14

1.3 A typical run of the streaming current measurement in a porous media. Transient behavior of the streaming current and electrode polarization are depicted (electrolyte is 10^{-4}M KCl). The inset shows pressure versus streaming current for ideal (dash line) and real electrodes (solid line). Steady state external currents do not represent the streaming currents 15

2.1 Schematic of microchannel pressure-driven flow geometry 25

2.2 Boundary Conditions for (a) N-S equation (b) Poisson equation and (c) Nernst Planck equations 32

2.3 Comparison of the velocity profiles at the mid-plane ($\bar{z} = 50$) of the capillary microchannel. Solid lines are the predictions obtained from Eq. (2.14) while symbols are predictions from the numerical simulations. Results are shown for three values of scaled capillary radius. 38

2.4 (a) Variation of the scaled electric potential with scaled axial position along the capillary centerline ($\bar{r} = 0$). The vertical dashed lines are the demarcations between the inlet reservoir, the capillary, and the outlet reservoir. The potential difference between the inlet and outlet reservoirs is denoted as the streaming potential. The result was obtained for $\kappa a = 5$. (b) Comparison of the numerical and analytical predictions of the streaming potential for different κa. See text for details. 41

2.5 Influence of the exit plane boundary condition (at the plane GH in Fig. 2.2) on (a) ion concentration and (b) electric potential distributions along the capillary centerline ($\bar{r} = 0$). The results were obtained for $\kappa a = 5$. 42

2.6 Axial variations of the (a) electric potential, (b) field, (c) co-ion concentration, and (d) counter-ion concentration along the capillary centerline ($\bar{r} = 0$) during the initial stages of the transient electrochemical transport. The results were obtained for $\kappa a = 5$. The scaled time is given as $\tau = \kappa^2 Dt$, where t is the time. 47

2.7 Axial variations of the (a) electric potential, (b) field, (c) co-ion concentration, and (d) counter-ion concentration along the capillary centerline ($\bar{r} = 0$) during the later stages of the transient electrochemical transport. The results were obtained for $\kappa a = 5$. The scaled time is given as $\tau = \kappa^2 Dt$, where t is the time. . . . 48

2.8 Changes in the ion concentrations relative to the initial concentration distribution along the channel centerline ($\bar{r} = 0$) at different instants. (a) counter-ion (positive ion in this case) and (b) co-ion (negative ions). All simulation parameters are identical to those used for Fig. 2.6. Due to near symmetry between inlet and outlet, the time labels are only identified once. 53

2.9 Local perturbation in the charge densities at the inlet and outlet of a finite length microchannel. This imbalance of charge manifests itself in Poisson equation and induces a transcapillary potential and conduction current. See text for detail. 54

2.10 Variation of streaming potential with different surface charges on the inlet and outlet faces and the walls of the capillary. Considering the geometry of Fig. 2.2, the scaled charge densities on the boundaries CD (front face), DE (capillary wall), and EF (back face) were varied independently between zero and $\bar{\sigma}_w = 2.0\sinh(0.5\bar{\psi}_w)$, where $\bar{\psi}_w = -1$. Case (a): both front and rear faces with zero charge density. Case (b): back face with zero. Case (c): Front face with zero. Case (d): all faces equally charged. In (a) to (d), the capillary wall was always charged. For comparison, the simulation with capillary wall charge density set to zero, is also shown. In this last case, the front and back faces are charged. 56

3.1 Schematic of pressure-driven flow geometry, which includes the microchannel, and inlet and outlet reservoirs. The planes II, JJ, and KK denote locations where the current is integrated over the channel cross section. 61

3.2 Transient numerical results for geometry and flow conditions for the base case. Panels (a)-(c) show the transient convective, migration and net currents calculated at the mid-length of the channel, and also include the transport of the positive and negative ions at the same location 72

3.2 Continued, Transient numerical results for geometry and flow conditions for the base case. Panel (d) shows the transient transcapillary potential with the inlet reservoir defined as ground. Panel (e) compares the normalized rise in transcapillary potential to the rise in migration current at the channel mid-length. Panel (f) shows the transient development of the centerline hydrodynamic velocity at the mid-length of the channel 73

3.3 Time sequences (0.1, 1, 10 and 100 μs) of spatial variation in free charge density relative to the no flow (continued on next page). 75

3.3 Continued: 2D representation of time sequences (0.1, 1, 10 and 100 μs) of spatial variation in free charge density relative to the no flow 76

3.4 Temporal variation in (a) the characteristic resistance, (b) the characteristic capacitance, (c), and R-C characteristics of the microchannel system. 77

3.5 Electrical analogy of a microchannel. The current source, S, is analogous to the convection current, the capacitor (C) allows for the accumulation of charge and development of a potential difference, and the resistor (R) makes the migration current respond synchronously to the potential difference. 79

3.6 Comparison of Navier-Stokes, Poisson-Nernst-Planck model for transient microchannel flow with an electrical analogy based on a current source, capacitor and resistor in terms of the transcapillary potential, which is represented by a voltmeter; V, in the analogy. 80

3.7 Transient response of net current at the mid-length of the channel and transcapillary potential for the systematic variation in the parameter L/a , which was altered through varying the channel length. The lines without symbols are the full numerical simulation results, while symbols connected by lines are the results of electrical analogy model. The capacitances shown are a calculated quantity. 82

3.8 Transient response of net current at the mid-length of the channel and transcapillary potential for the systematic variation in the parameter κa, which was altered through varying the Debye length. The lines without symbols are the full numerical simulation results, while symbols connected by lines are the results of electrical analogy model. The capacitances shown are a calculated quantity independent of κa. 83

3.9 Transient response of net current at the mid-length of the channel and transcapillary potential for the systematic variation in Re , which was altered through varying the pressure difference across the channel. The lines without symbols are the full numerical simulation results, while symbols connected by lines are the results of electrical analogy model. The capacitances shown are a calculated quantity independent of Re. 84

3.10 Transient response of net current at the mid-length of the channel and transcapillary potential for the systematic variation in the surface potential parameter, which was altered through varying the surface charge density. The lines without symbols are the full numerical simulation results, while symbols connected by lines are the results of electrical analogy model. The capacitances shown are a calculated quantity independent of the surface potential parameter. 85

4.1 Parallel array of individual current sources which comprises a multi microchannel array. Since current is additive, the summation of all currents represents the total current; I_{array} 95

4.2 Schematic of the proposed electrical analogy for a multi microchannel array and electrodes associated with external circuits. The circuit is divided into two parts based on the whether the charge carriers are ions or electrons, and the interface in the surface of the electrodes (points A and C). Re-distribution of ions by flow fields at L and R planes induces the transcapillary-potentials. R_B and R_E are the bulk and electrode electrical resistance, respectively. R_L is the external load and the extremes of this load represents the ideal measurement devices such as a voltmeter ($R_L -> \infty$) or an ammeter ($R_L -> 0$) 97

4.3 Simplified schematic of a multi microchannel array and electrodes associated with external circuits. $R_{effective}$ equals to $\frac{R_1}{N}$ where R_1 and N are the electrical resistance of a single microchannel and number of microchannels, respectively. $C_{effective}$ equals to $N \times C_1$ where C_1 represents the capacitance of a single microchannel. . 98

4.4 Schematic of an equivalent electrical analogy in the open circuit mode, namely, streaming potential. 101

4.5 A digital image of the experimental apparatus. Electrolyte is pumped from reservoir, controlled by a flow control valve, passes through the 3-way valves, the setup and the flow meter and finally returns to reservoir. The purpose of the 3-way valves are to enable an alternating flow direction in the setup. The inset shows the setup, constructed from three independent acrylic sections; an inlet reservoir, a cylinder that surrounded and held the microchannel array in place, and an outlet reservoir. The PTD, represents the pressure transducer. 102

4.6 Schematic of the multi microchannel cell. The electrodes are movable across the reservoirs. The multi microchannel array thickness is 2 mm and the length of the reservoir is 36 mm. See text for details. 104

4.7 SEM images of a typical microchannel array which show an array of single, straight and circular microchannels. The array being used in this study has a pore size of 10 μm. Its thickness and diameter are 2 mm and 25 mm, respectively. Courtesy of Burle Electro-Optics, Sturbridge, Massachusetts. 108

4.8 Streaming potentials vs. pressure drops, streaming potentials were measured for 0.1, 1 and 2 mM KCl all at pH of 6.6 ± 0.3 using the platinized platinum electrodes. ζ potential of the employed untreated glass was estimated to be -57 ± 3 mV at 2 mM KCl, pH =6.6. Comparison of Smoluchoswki equation and experimental data shows excellent agreement. Error bars are standard deviations. 110

4.9 External current and streaming potential measurements in a multi microchannel array with 3,475,500 microchannels. The experiments were performed for 1mM KCl solution in identical flow rates, using platinized platinum and silver mesh electrodes. In order to avoid electrode polarization, the electrolyte solution was pumped into the array in alternating flow directions for a total of four times (two times in each direction) 112

4.10 External current measurements in a multi microchannel array with 3,475,500 microchannels. The experiments were performed for 0.04 and 1 mM KCl solutions in identical flow filed conditions using platinized platinum electrodes. In order to avoid electrode polarization, the electrolyte solution was pumped into the array in alternating flow directions for a total of four times (two times in each direction) 114

4.11 (a) Experimental external current values obtained for 1 mM KCl in a multi microchannel array with only 550 pores. (b) Experimental streaming potential values obtained for 1 mM KCl. Platinized platinum electrodes were used for both experiments. In order to avoid electrode polarization, the electrolyte solution was pumped into the array in alternating directions for a total of four times (two times in each direction) 115

5.1 (a) Schematic of the experimental apparatus. 3,437,500 of parallel microchannels formed a multi microchannel array (25 mm effective diameter) akin to a porous medium. In experiments platinized platinum electrodes (25 mm diameter) were movable within the reservoirs. Nanogold electrodes (NGEs) were on the faces of the microchannel array. The microchannel array thickness was 2 mm and the length of the reservoirs was 36 mm, . . . 119

5.2 (a) A SEM image of a multi microchannel array coated with a nano layer of gold. It shows an array of single, straight and circular microchannels. It is made of untreated lead silicate glass with 55% porosity. (b) Longitudinal cross section of the microchannels. Metal penetration depth inside the capillaries is shown. Bright area indicates the gold deposited area. In the current sample the penetration depth is 0.3-0.7 times of channel diameters on both sides. Penetration depth is negligible compared to the thickness of the multi microchannel array (2 mm). The sample has a pore size of 10 μm and thickness and effective diameter of 2 mm and 25 mm, respectively. (Courtesy of Burle Electro-Optics, Sturbridge, Massachusetts.) 120

5.3 An equivalent electrical analogy of the streaming current device. I_s, R and C represent the current source, total electrical resistance and total capacitance of the multi microchannel array. R_g, C_g, R_p and C_p are the electrical resistance and capacitance of NGEs and platinum electrodes. R_{res} and $R_{res,p}$ are the bulk electrolyte resistance inside the reservoirs 121

5.4 A simplified version of electrical analogy. See text for details . . 122

5.5 Final simplified version of the electrical analogy. R_t and C_t show the total electrical resistance and capacitance of the NGEs and $R_{res,t}$ is the total bulk electrolyte resistance. 123

5.6 Equivalent electrical circuit of microchannel array coated with a nano layer of gold in parallel with an external resistance. R and C are the electrical resistance and capacitance of the multi microchannel array, R_1 and R_2 represent the nanogold electrodes resistance. R_{res} shows the reservoir electrolyte resistance. R_{ext} is the external resistance parallel to the multi microchannel array. 126

5.7 Electrical resistance of the multi microchannel array vs. Concentration of the KCl electrolyte solution. 127

5.8 Simultaneous measurement of current and voltage by NGEs and platinized platinum electrodes across the multi microchannel array. An electrolyte solution of 0.1 mM KCl was pumped through the multi microchannel array in alternating flow directions. Since electrodes were unable to digest all the free charges, consequently a potential developed and detected by platinum electrodes. In streaming current measurements using NGEs, value of first peak was smaller compared to other peaks due to presence of stationary electrical double layer in first cycle of experiments. 129

5.9 Comparison of Current-Voltage plot with Smoluchoswki equation. The Current-Voltage plot extracted from transient response of current and voltage measured by NGEs and platinized platinum electrodes simultaneously. Smoluchoswki equation was plotted using independent values of streaming potential and conductance of the multi microchannel array. The intersection of Y axis and Smoluchoswki equation represents an estimate of streaming current in the multi microchannel array for electrolyte solution of 0.05 mM KCl. 133

5.10 Comparison of Current-Voltage plot with Smoluchoswki equation. The Current-Voltage plot extracted from transient response of current and voltage measured by NGEs and platinized platinum electrodes simultaneously. Smoluchoswki equation was plotted using independent values of streaming potential and conductance of the multi microchannel array. The intersection of Y axis and Smoluchoswki equation represents an estimate of streaming current in the multi microchannel array for electrolyte solution of 0.1 mM KCl. 134

5.11 Comparison of Current-Voltage plot with Smoluchoswki equation. The Current-Voltage plot extracted from transient response of current and voltage measured by NGEs and platinized platinum electrodes simultaneously. Smoluchoswki equation was plotted using independent values of streaming potential and conductance of the multi microchannel array. The intersection of Y axis and Smoluchoswki equation represents an estimate of streaming current in the multi microchannel array for electrolyte solution of 0.5 mM KCl. 135

5.12 a) Streaming potentials measured with platinized platinum electrodes and NGEs across the reservoirs and right at the multi microchannel array faces for 0 M KCl and 0.5 mM KCl. b) Corresponding external current obtained by platinized platinum electrodes (inside reservoirs) and NGEs (at multi microchannel array faces) for the same electrolyte solutions. Experiments were conducted in an identical flow rate of 0.72 l/min. 138

5.13 Power of the streaming current device vs. Total external resistance. The maximum power occurred at the point where total external resistance becomes identical to electrical resistance of the device. Addition of salt virtually reduced device performance (inset). 139

6.1 The Integrated Parametric Current Transformer (IPCT) employed in this study is a current sensor which works on the principle of the Direct Current Current Transducer, DCCT. Courtesy of GMW Associates, Inc. 144

CHAPTER 1

INTRODUCTION

Flow under the combined influence of pressure and electrical fields (electrokinetic flow) is of great interest and central to micro and nanofluidic devices [1–4], membrane characterization [5, 6], biological systems [7–10], mapping of groundwater contamination [11], oil recovery [12], and even earthquake and volcano prediction [13, 14]. The scientific community's interest in the topic of electrokinetic transport phenomena - a field which has been known for many years (first observations by Quincke, 1859) - has renewed by emergence of the microfluidics. Microfluidic systems are governed by viscosity, diffusion and interfacial phenomena rather than gravity and inertia. The large ratio of surface area to volume of microfluidic systems strongly affects fluid behavior, particularly at the solid-liquid interfaces. The nonlinearity and instabilities of macroscopic flows due to non-linear inertia component do not exist in microfluidic systems, so one might think dealing with microfluidics is trivial. By contrast, microfluidics is rich in physics and chemistry as evidenced by the occurrence of several multiphysics phenomena [1, 15]. Understanding of electrostatics, thermodynamics and fluid dynamics along with transport of charged species is required to explain microfluidic phenomena.

1.1 Background

The intrinsic characteristic and nature of fluid flow in the micro scale is different from the macro scale in several aspects. We shall briefly discuss and explain these differences in the following sections.

1.1.1 Low Reynolds Number Flows

Some of the flow physics underlying the microfluidics systems is dictated by competition between different phenomena and can be captured by the Reynolds number, a dimensionless number defined as the ratio of the inertial forces over the viscous forces

$$\mathrm{Re} = \frac{\rho V^2/d}{\mu V/d^2} = \frac{\rho V d}{\mu} \tag{1.1}$$

Low Reynolds number flows ($\mathrm{Re} < 1$) are dominated by viscous forces rather than inertia. In microchannels, flow is laminar, viscous forces are dominant and momentum balance, normally described by the Navier-Stokes equation, can be simplified to the Stokes equation. Due to the dominance of viscous forces in low Reynolds number flows, the location of every fluid's elements is mainly determined by the forces that currently exist on each element and not by the past [16]. For typical microchannel simulations, fluid properties and validation used in this work the Reynolds number was around $0.5 < \mathrm{Re} < 1$.

1.1.2 Continuum Approach, Is It Valid in Microfluidics ?

Macroscopic flows are described by momentum and continuity equations and are based on the assumption that a fluid is a continuum. Microfluidic phenomena can also be treated by a continuum approach. To verify the validity of the continuum approach one needs to calculate the Knudsen number ($\mathrm{Kn}=\lambda/\mathrm{L}$, where λ is the mean free path and L is the characteristic length of the flow). For fluids λ is the intermolecular distance. For instance, for water the average molecular distance; $\lambda = 0.3$ nm which obtained by [17]

$$\lambda \sim (\frac{M}{\rho N_A})^{1/3} \tag{1.2}$$

where ρ is density, M is molar mass and N_A is Avogadro's number. While for Kn$>$ 0.1 the continuum assumptions are no longer valid, the continuum approach is still applicable considering the solid-liquid interaction (slip boundary condition) for the momentum equation when 0.01 $<$Kn$<$ 0.1. In this study, since we are dealing with microfluidics; (microchannel diameter $\sim$ 1 μm), Kn is relatively small $\sim 3 \times 10^{-4}$ and therefore the continuum assumptions are applicable.

1.1.3 The Electric Double Layer and Boltzmann Distribution

Liquid-solid interactions generally do not extend beyond the micrometer and nanometer scales and hence their existence can be the key importance for microfluidics. Usually solid surfaces (such as glass, silica, acrylic and even metals such as gold) in contact with polar liquids (such as water) acquire surface electric charges. The formation of spontaneously charged layers at the interface are due to several mechanisms, namely, differential adsorption of ions from an electrolyte onto the solid surfaces, deprotonation of surface groups and surface ionization. For instance, in the case of glass (Glass has two types of surface groups; Siloxal groups; SiO_2 and Silanol groups; SiOH), the deprotonation of silanol groups (SiOH) governs the surface charge density. The Siloxal groups can be considered as inert. The equilibrium reaction associated with charge formation of Silanol groups exposed to a typical salt solution (NaCl) can be written as [18]

$$SiOH \leftrightarrows SiO^{-} + H^{+} \tag{1.3}$$

$$SiO^{-} + Na^{+} \leftrightarrows SiONa \tag{1.4}$$

The equilibrium constant of Eq. 1.3 is K=$\frac{[H^{+}][SiO^{-}]}{[SiOH]}$ and is a function of local pH, while Eq. 1.4 involves electrolyte concentration. Surface charge densities are shown to increase with increasing the temperature and pH and to decrease with increasing the electrolyte concentration. The idea of the electrical double layer was proposed by Helmholtz (1879)[18, 19]. Helmholtz considered the electrical double layer mathematically as a simple capacitor, based on a physical model in which a single layer of ions is adsorbed at the solid-liquid interface. Later Gouy and Chapman (1910-1913) introduced a diffuse model of the electrical double layer. The current understanding of the electrical double layer is based on the Gouy-Chapman-Stern model, which combines the Helmholtz single adsorbed layer with the Gouy-Chapman diffuse layer [18]. Fig. 1.1 illustrates the electrical double layer and distribution of co-ions and counter-ions next to a negatively charged surface. The ions in the diffuse layer are mobile, while the Stern layer is stationary. The Debye length represents the characteristic thickness of the electric double layer and is created by a balance between the diffusion and electrical forces. An equivalent thermodynamic equilibrium condition for such a balance is given by $\nabla\overline{\mu}_i$=0 where $\overline{\mu}_i$ is the electrochemical potential. The electrochemical potential is defined as

$$\overline{\mu}_i = \mu_i + \nu_i e\psi, \tag{1.5}$$

where μ_i, ν_i and e are the chemical potential, valence of type-i ions and elementary charge and ψ is the electrical potential, respectively. The chemical potential of the ions can be express by

$$\mu_i = \mu_i^0 + k_b T \ln(n_i), \tag{1.6}$$

where μ_i^0 is a constant for type-i ions, k_b is the Boltzmann constant, T is the temperature and n_i is the ionic concentration number of the type-i ions. From Eq.1.5 and Eq.1.6 and having $\nabla\overline{\mu}_i$=0, the Nernst equation is obtained

$$\frac{1}{n}\frac{dn_i}{dy} = -\frac{\nu_i e}{k_b T}\frac{d\psi}{dy}, \tag{1.7}$$

Integration of the Nernst equation employing appropriate boundary condition; (ψ=0, n_i=n_0) yields the Boltzmann distribution

$$n_i = n_0 \exp\langle -\frac{\nu_i e \psi}{k_b T}\rangle, \tag{1.8}$$

where n_0 is the bulk concentration. It should be keep in mind that Boltzmann distribution solely represents the ion distribution of a stationary system. In this work, the Poisson-Nernst-Planck (PNP) equation is employed instead of Poisson-Boltzmann (see Chapters 2 and 3). To our knowledge, most analytical and numerical studies of electrokinetic transport phenomena were based on Poisson-Boltzmann equation and are subject to inaccuracies [20–22]. The PNP equation, however, predicts the disturbance of Boltzmann distribution subject to a flow field and allows prediction of axial concentration variation (see Chapter 2 and 3 for details). Having the Boltzmann distribution and invoking the Poisson equation ($\nabla^2\psi = -\frac{\rho_c}{\epsilon}$), which relates the charge densities (ρ_c) to electrical potential (ψ); the electric double layer thickness (κ^{-1}) can be estimated

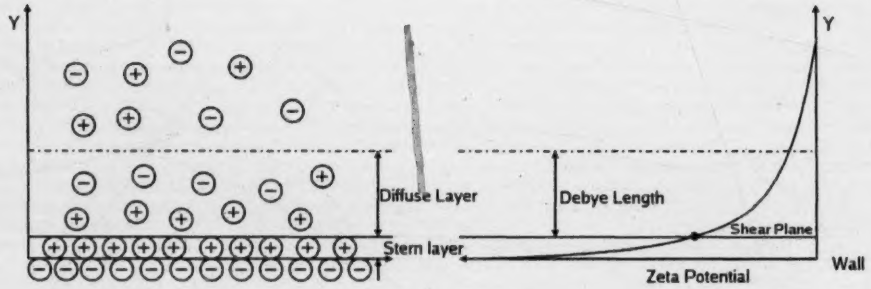

Figure 1.1: Schematic of Electrical Double Layer: (Left) Distribution of ions next to a negatively charged surface; Stern layer and diffuse layer are shown. (Right) A negative potential profile from a negatively charged surface towards the bulk, showing the ζ potential on the shear plane. Debye length; represents the thickness of electrical double layer and is in the order of a few hundreds nano meters (reproduced from ref. [1])

(for more details see Hunter [18]).

$$\kappa^{-1} = \sqrt{\frac{\varepsilon k_b T}{2e^2\nu^2 n_0}} \tag{1.9}$$

The important assumptions in the derivation of the electric double layer thickness are: a) ions are effectively point charges; b) interactions are Columbic; and c) electrical permittivity is constant throughout the electric double layer. This approximation is valid for low surface potentials (Debye-Huckel approximation, $\frac{\nu\psi}{k_b T} \leq 1$) and symmetric electrolytes. The ratio of double layer thickness to the microchannel radius (a); "κa" is of importance in microfluidics. For instance, when $\kappa a = 5$; double layer thickness is five times smaller than microchannel radius.

1.1.4 The ζ potential

As noted above, the Gouy-Chapman-Stern model renders the ion distributions and the Boltzmann equation provides the electrical potential profiles. The magnitude of such potential reaches its maximum at the solid surface, drops sharply through the Stern layer and asymptotically approaches zero in the bulk electrolyte. The potential at the interface of the Stern layer and diffuse layer (shear plane) is called the ζ potential (see Fig.1.1). In other words, the ζ potential represents the relative magnitude of the counter-ions surrounding a charged surface with respect to the bulk and represents an electrical boundary condition of the fluid phase. The ζ potential of a typical solid surface can not be determined directly and several methods (*i.e.* Streaming current and potential, Electroosmosis and Electrophoresis) have been applied to assess the interfacial properties of particles, solid surfaces and membranes [5, 18, 23–28]. We wish to point out that the reported ζ potentials in the literature are rather scattered [23–27, 29–36]. For instance, reported ζ potentials of a glass surface subject to similar environment and obtained with streaming potential technique spans from -55 to -177 mV [37, 38]. Also the ζ potential values determined from streaming potential and streaming current technique have been shown to be different [39, 40]. These two techniques share the same basic setup and sample preparation, thereby making excuses for the inconsistencies more difficult. Review of literature suggests that such discrepancies are typically attributed to either errors in the theoretical assumptions/models or in the sample preparation [40]. What appeared to be missing in the existing literature was a systematic exploration of streaming current measurements in structured porous media and interaction of fluidic systems with external circuit and electrodes. Conventional measurements of such processes do not confer much attention to these factors, instead focussing on the unknown pore structures of the porous media to analyze the results. The intrinsic uncertainty associated with unstructured porous media is significantly reduced in this work. Chapters 4 and 5 elaborate on issues associated with the streaming current technique in structured porous media.

1.2 Electrokinetic Flow

Electrokinetic flow, *i.e.*, flow of an electrolyte solution in microchannels driven by the combined influence of transcapillary potential and pressure results in observable effects, namely, streaming currents and streaming potentials [20, 41–45](see later). The formulation of streaming potential phenomena is based on several assumptions. These include: a steady state analysis; an infinite length microchannel; a linearized PoissonBoltzmann equation, and neglecting the end effects. In this thesis (Chapters 2 and 3) none of these assumptions were invoked. To gain more insight, a transient study of the full non-linear equations was performed and to make the result comparable with experiments, a finite length microchannel domain was considered. Observation of electrical and flow properties inside the reservoirs, analysis of end effects and tracking the ion transport in a small "κa" system shed some light on the current understanding of streaming potential phenomena. In the following sections, an introductory review and derivation of electrokinetic flows are given.

From a theoretical view point, for a cylindrical microchannel, the total current; I_{total} caused by pressure driven flow and induced transcapillary potential can be estimated by summation of convection (I_{conv}) and conduction (I_{cond})

currents (diffusion current is shown to be negligible, see later). The convection current is calculated by integration of the product of velocity and free charge density

$$\mathrm{I}_{conv} = 2\pi \int_{0}^{r} \rho_c(r)u(r)r\,dr \tag{1.10}$$

where r is the radius of the pore, $\rho_c(r)$ is the free charge density, $u(r)$ is the hydrodynamic velocity profile. Eq.1.10 shows that the magnitude of charge separation and convection current can be influenced by altering the velocity profile and double layer thickness. By inserting the velocity (obtained from the Navier-Stokes equation) and free charge density (obtained from the Poisson-Boltzmann equation) Eq.1.10 (see Chapter 2 for details); the convection current in a single microchannel can be estimated [42]

$$\mathrm{I}_{conv} = \frac{-\epsilon}{\mu}\zeta P_z A \cdot f(\kappa a) - \frac{\epsilon^2\zeta^2}{\mu}\kappa^2 E_z A \cdot f'(\kappa a), \tag{1.11}$$

where ϵ is permittivity, μ is the viscosity, P_z is pressure gradient, A is cross-sectional area of streaming channel, f is a correction function, κ^{-1} is the Debye length and a is the radius of the microchannel. For $\kappa a \gg 1$, $f(\kappa a)$ and $f'(\kappa a)$ $= 1$; and for low κa, $f(\kappa a) = [1 - \frac{2I_1(\kappa a)}{\kappa a I_0(\kappa a)}]$ and $f'(\kappa a) = [1 - \frac{2I_1(\kappa a)}{\kappa a I_0(\kappa a)} - \frac{I_1^2(\kappa a)}{I_0^2(\kappa a)}]$. I_0 and I_1 are the zeroth and first order modified Bessel functions of the first kind, respectively.

Conduction current or migration refers to transport of ions under an applied or induced electrical field. The flux (j_i^*) based on the number concentration of species (n_i) bearing a charge ($q_i = \nu_i e$) in presence of an electrical field $\mathrm{E} = -\nabla\psi$ is given by

$$\mathrm{j}_i^* = -\frac{D_i}{k_b T} n_i(\nu_i e)\nabla\psi, \tag{1.12}$$

where D is the diffusivity and $\frac{D_i}{k_b T}$ is the mobility of i^{th} solute species. The current as a result of migration then becomes; $\mathrm{I}_{cond} = e\sum \nu_i j_i$ which can be simplified to [17]

$$\mathrm{I}_{cond} = A\sigma^{\infty} E_z, \tag{1.13}$$

where A is the cross section of microchannel and $\sigma^{\infty} = \frac{2e^2\nu^2 D n_{\infty}}{k_B T}$ is the bulk conductance (S/m). Conduction current profiles are shown in Fig.1.2 for different κa in a steady state flow. At steady state, the total conduction and convection currents are equal (a condition of the Smoluchoswki equation). Due to excess of charges in double layer, the electrical resistance of the Stern and diffuse layer are lower compared to the bulk (*i.e.* surface conductance) and hence conduction current are favored to pass through the double layer rather than bulk electrolyte. The concept of surface conductance manifests itself in Eq.1.13 as following

$$\mathrm{I}_{cond} = A\sigma^{\infty} E_z F_{cc}, \tag{1.14}$$

The term F_{cc} is a correction factor which accounts for the conduction current through the electrical double layer and for a circular microchannel is given by

$$\mathrm{F}_{cc} = 1 + \frac{2\sigma^s}{a\sigma^{\infty}},$$

where σ^s is the surface conductance. When $\mathrm{F}_{cc} = 1$, the conduction current becomes constant across the channel cross section. In typical analysis of the streaming potential [42], the term F_{cc} is often assigned a value of unity, which is a valid assumption for sufficiently large κa. F_{cc} is usually greater than unity for small κa. In Chapter 3, the transient behavior and evolution of conduction currents will be explained. Summing both the convection current Eq. 1.11 and the conduction current Eq. 1.14, total current becomes

$$I_{total} = \frac{-\epsilon}{\mu}\zeta P_z A \cdot f(\kappa a) - E_z A \sigma F_{cc} \langle 1 - \frac{\epsilon^2 \zeta^2 \kappa^2}{\mu \sigma F_{cc}} \cdot f'(\kappa a) \rangle, \tag{1.15}$$

Eq. 1.15 provides a general formulation for pressure driven electrokinetic flows under influence of transcapillary potentials and can be simplified into two specific cases, namely, streaming current and streaming potential as described in the following sections.

1.2.1 Streaming Current

1.2.1.1 Definition and Derivation

When the electrical double layer thickness becomes comparable with the microchannel dimensions, solid-liquid interactions are no longer negligible. Streaming currents and potentials are consequences of pressure driven flows in microchannels with charged walls. Streaming current represents an ionic convective flux; the fluid flow generates a force on the hydrodynamically mobile part of electrical double layer and the transport of free charge along the flow direction is the streaming current. When there is no transcapillary potential as such $E_z = 0$, and Eq. 1.15 simplifies to

$$I_{str} = \frac{-\epsilon}{\mu}\zeta P_x A \cdot f(\kappa a), \tag{1.16}$$

where I_{str} is the streaming current. Considering Eq. 1.16, the ζ potential can be calculated from the slope of the pressure-current line. In streaming current measurement, the electroviscous (flow retardation) effect is usually negligible and the flow rate has a linear relationship with the pressure gradient. Now let us discuss the physical picture of ions and current transport in microchannels with different κa. The thought experiment is based on considering the motion of ions along the flow field and then rendering the velocity, free charge density, streaming currents and conduction profiles which are of importance in understanding the concept of streaming potential. Fig. 1.2 depicts a qualitative comparison of streaming current profiles and corresponding free charge density and velocity profiles for a microchannel with $\kappa a = 1$, 5 and 25. Depending on the κa of the system, the free charge density and the corresponding streaming and conduction current can be limited to the motion of ions next to the wall or can disturb the flow field significantly. As expected, parabolic velocity profiles are not affected by these variations of κa yet free charge density and streaming current profiles are a function of κa. At $\kappa a = 1$, the double layers extend to the core of circular microchannel and the streaming current profile becomes relatively similar to the velocity profile. In Chapter 3, early transient behavior and evolution of currents, namely, convection, migration and net currents will be discussed with the aid of numerical models.

1.2.1.2 Streaming Current and Electrode Polarization

Experimentally, direct streaming current measurements are conducted with an ammeter with negligible internal resistance and that is connected to standard electrodes at the end of a microchannel or porous media. A typical run of such an experiment is shown in Fig. 1.3. When an electrode is immersed in an electrolyte solution, the ζ potential develops at the electrode-electrolyte interface. In order to neutralize the excess charges, the counter ions in the medium adsorb to the electrode surface forming a double layer. The electrode impedance and capacitance caused by the unwanted accumulation of the ions on the electrode surface, attenuates the measured electrical properties, namely the streaming currents. This phenomenon is referred to as electrode polarization. In other words, if the ionic flux toward the electrodes is not ***always*** balanced by the electric flow through the short circuit wire/ammeter, then charges will accumulate causing a non-steady state where the streaming current will decay with time, as shown in Fig.1.3 [46, 47]. The polarization potential induces a conduction current in microchannels and therefore contradicts the assumption of zero potential difference in the streaming current measurement. In Chapter 5, the transient response and characterization of polarizable nanogold electrodes with the aid of an equivalent electrical analogy is presented. The electrochemical reactions occurring at electrode-electrolyte interface were not considered in this study and is beyond the scope of this thesis.

1.2.2 Streaming Potential

1.2.2.1 Definition and Derivation

A common textbook description of the streaming potential is "when a liquid is forced through a microchannel under hydrostatic pressure, the ions in the mobile part of the EDL are carried towards one end. The accumulation of ions downstream sets up an electrical field with an electrical potential called streaming potential" [18, 48]. Another description of the phenomenon is, "the phenomena of streaming current and streaming potential occur in general due to the charge displacement in the electrical double layer caused by an external force shifting the liquid phase tangentially against the solid" [24]. While capturing the

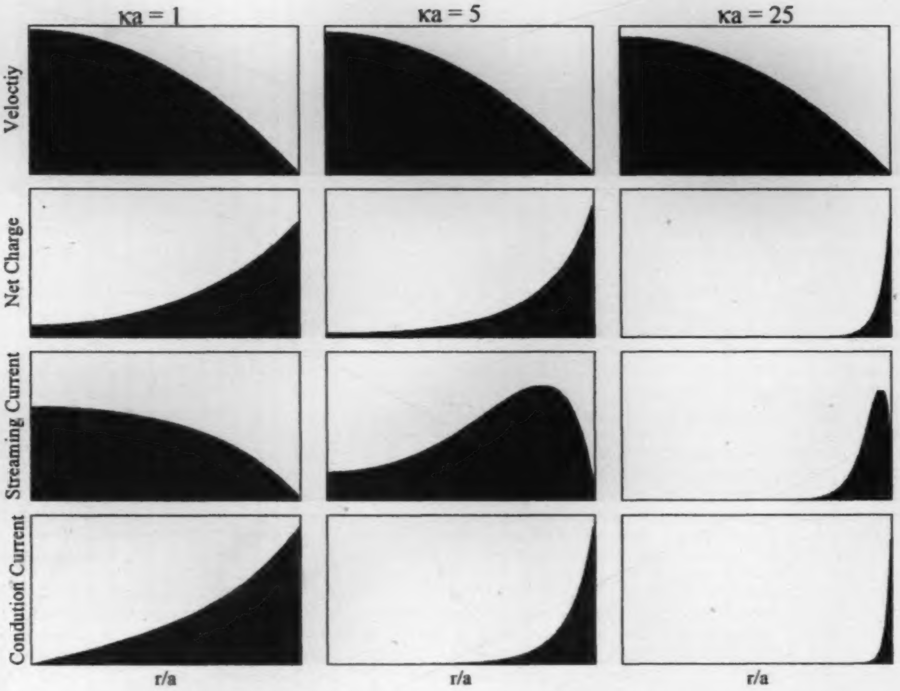

Figure 1.2: Qualitative comparison of velocity, free charge density, streaming current and conduction current profiles for a microchannel with $\kappa a = 1$, 5 and 25 in a steady state flow condition. The first row of the graph shows the parabolic velocity profiles induced by pressure driven flow in the microchannels; zero velocity at the wall (no-slip boundary condition) and maximum velocity at the center. Velocity profiles as expected are similar in different κa. In the second row, a negatively charged surface (ψ = -25 mV) attracts the counter-ions and repels the co-ions. In the third row, streaming current profile which is the product of free charge density and velocity. In large κa streaming currents are negligible and limited to transport of ions next to the wall. The last row represents the conduction current profiles. Since the electrical resistance of the double layer is relatively lower than bulk electrolyte, the conduction currents migrate through Stern and diffuse layers next to the charged wall.

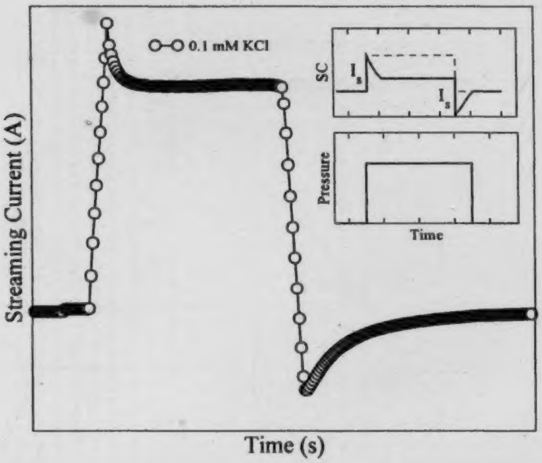

Figure 1.3: A typical run of the streaming current measurement in a porous media. Transient behavior of the streaming current and electrode polarization are depicted (electrolyte is 10^{-4}M KCl). The inset shows pressure versus streaming current for ideal (dash line) and real electrodes (solid line). Steady state external currents do not represent the streaming currents

essence of the streaming potential phenomenon, the above descriptions are primarily based on a steady-state analysis of the electrokinetic transport problem, and hence, they do not provide a complete picture regarding the transient nature of the streaming potential development. Furthermore, the descriptions do not summarize the roles of the different transport contributions to the development of the electrical potential. Most importantly, neither description emphasizes the difference between the general development of a transcapillary potential and the specific case of a streaming potential. One needs to identify streaming potential with the condition that the net current through the system be zero. To further understand the transient behavior of the streaming potential and to realize how and where an electrokinetic flow influences ion concentrations during evolution of the streaming potential, it is instructive to carefully observe the initial time steps of the potential development. We conducted afew simulations with very small time step increments to capture the initial stages of the flow immediately after the setting up of the pressure gradient (see Chapters 2 and 3 for details).

The Smoluchowski equation can be recovered when the total current; Eq. 1.15 is set to zero

$$\left(\frac{\Delta V}{\Delta P}\right)_{I=0} = \frac{\epsilon\zeta}{\mu\sigma^{\infty}F_{cc}} f(\kappa a, \beta), \tag{1.17}$$

where

$$\beta = \frac{\epsilon^2\zeta^2\kappa^2}{\mu\sigma^{\infty}F_{cc}},$$

and

$$f(\kappa a, \beta) = \frac{(1 - \frac{2A_1}{\kappa a})}{1 - \beta(1 - \frac{2A_1}{\kappa a} - A_1^2)},$$

In the above expression, V is the transcapillary potential, $A_1 = I_1(\kappa a)/I_0(\kappa a)$ and σ^{∞} is the bulk electrolyte solution conductivity. Eq. 1.17 allows calculation of ζ-potential from the streaming potential measurements. For a known applied pressure gradient and induced potential difference across the capillary (i.e. streaming potential), the ζ potentials can be obtained. Both streaming potential and streaming current techniques share the same basic physical setup and sample preparation, the former requires *a priori* knowledge of the surface conductance, which has to be determined independently, while streaming current does not require such information and hence has recently been employed for extensive ζ-potential measurements [49, 50]. Based on the results presented in this work (see Chapter 4) in addition to electrode polarization, several cautions should be taken into account with direct streaming current measurements particularly in porous media.

1.3 Objectives and Scope of the Thesis

Due to the emergence of micro and nanofluidics, researchers in pure and applied disciplines have become increasingly interested in electrokinetic phenomena, namely electrophoresis, electroosmosis and streaming potential. Despite many studies several issues associated with streaming potential and streaming current phenomena in terms of understanding (such as early-time transient behavior and evolution of currents, potentials and flow properties, different time scales and end effects) and applications (such as direct streaming current measurement in porous media) remain unclear. Therefore the focus of this work is mainly on the streaming potential and streaming current phenomena. Some of key objections are:

1- Improved understanding of the ion transport and analysis of transient trans-capillary potentials, migration, diffusion, convection and net currents leading to transient accumulation of charges at either end of a finite length microchannel with small "κa".

2- Developing an electrical analogy for transient behavior of a pressure driven flow inside a finite length microchannel and validate it against a full numerical model. Also providing a formulation to estimate the capacitance of a finite length circular microchannel and porous media

3- Studies on structured porous media including streaming current and streaming potential measurements

4- Analysis of electrokinetic energy conversion in a multi microchannel array (structured porous media) specifically coated with nano layer of gold on both sides

5- Developing an electrical analogy for transient behavior of a pressure driven flow inside a multi microchannel array and characterization of nano gold electrodes with the aid of analogy (similar to cyclic voltammetry)

This study is aimed to add to modern understanding of ion transport inside finite length microchannels, and to elaborate on evolution of streaming potential; a widely used concept. The pertinent electrical analogies are proposed to facilitate treating transient flow problems inside single and multi microchannels. Also a great deal of work is performed on streaming current measurement in structured porous media leading to the fact that experimental results are subject to several concerns and one should instead employ streaming potential technique. The findings are applicable to enhance the performance of electrokinetic energy conversion devices and possibly increase the maximum power and efficiency of the system.

1.4 Organization of the Thesis

A paper format is used for this thesis and hence each chapter is written independent of the others and includes their own introduction, methodology, results and conclusions. Chapters 2 and 3 deal with a single microchannel and Chapter 4 and 5 deal with structured porous media.

In Chapter 2, a time-dependent numerical model governed by the Navier-Stokes and Poisson-Nernst-Planck equations was developed and solved in a finite length microchannel domain. This model addresses the transient behavior and evolution of streaming potential in a finite length microchannel and clearly shows how and where an electrokinetic flow influences ions concentration during evolution of the streaming potential.

In Chapter 3, the analysis of streaming potential was continued by carefully following the transient behavior of convection, migration and net currents. Based on unsteady characteristics of the streaming current, capacitance and electrical resistance a parallel resistive-capacitive circuit to a DC current source was proposed as an equivalent electrical analogy of a finite length microchannel. The appropriateness of the electrical analogy was examined and a comparison was made between the charging behavior of a parallel plate capacitor and a finite length microchannel. In order to use the electrical analogy independently, sub-models were developed for current source, capacitive and resistive elements employing dimensional analysis.

On the experimental side in Chapter 4, streaming potential and streaming current techniques were studied and their benefits and drawbacks were examined. A custom experimental apparatus was employed to explore the consequence of changing the number of microchannels, electrolyte, placement and material of electrodes while using these techniques. Two types of electrodes (platinized platinum and silver mesh) served as conducting probes to measure either the electrical potential or current. Experimental observations were discussed and interpreted by aid of an equivalent electrical analogy. The proposed electrical analogy describes a general electrokinetic flow through porous media that is coupled with an external circuit to mimic and explain the physical phenomena at electrodes and nature of external electrical devices.

In Chapter 5, an extended study on electrokinetic energy conversion was made. A specifically made microchannel array coated with a nano layer of gold (Nanogold electrodes) was characterized as a streaming current device. Due to polarization and failure of the Nanogold electrodes in direct streaming current experiments, practical ways of streaming current measurements in porous media were proposed.

Finally in Chapter 6, a summary of this work is presented and possible directions of future works are outlined.

CHAPTER 2

EVOLUTION OF STREAMING POTENTIAL IN A FINITE LENGTH MICROCHANNEL: A TRANSIENT STUDY

2.1 Introduction

Microfluidic systems have profoundly transformed chemical analysis, separation, and detection techniques over the past decade by enabling rapid manipulation of extremely small volumes of fluid[1]. Development of microfluidics has attracted several research disciplines [51, 52], and has been the key factor for the resurgence of interest in electrokinetic transport phenomena. Electrokinetic (EK) flow, *i.e.*, flow of an electrolyte solution in narrow capillaries driven by the combined influence of electric field and pressure, is of significant interest in microfluidic devices [2]. Pressure driven flow of an electrolyte solution in narrow capillaries with charged walls is a sub-group of EK flow, and is still considered as one of common methods for moving fluids in microfluidic channel networks. Such a flow through narrow charged capillaries establishes a potential difference between the two ends of the capillary, which is referred to as the streaming potential [18]. The streaming potential is engendered by the flow of the ions relative to the stationary charged wall of the channel.

---

[1] Part of this chapter is closely related to the published work of "Ali Mansouri, Carl Scheuerman, Daniel Y. Kwok, Subir Bhattacharjee and Larry Kostiuk" in the Journal of Colloid and Interface Science, 2005 Dec 15;292(2):567-80

The theory of electrokinetic transport, particularly analysis pertaining to the calculation of streaming potential, has been thoroughly developed over the past century, with several textbook renditions [17, 18, 53–55] and numerous articles exploring different aspects of the governing transport phenomena [19, 20, 41–45, 56–60]. The above citations represent an extremely limited perspective of the enormous attention conferred to the theoretical interpretation of electrokinetic transport spanning the classical early works, to the more modern developments. Most of the above mentioned studies are based on a steady state analysis of the governing electrochemical transport equations and apply to microchannels of infinite length. These studies, barring [43, 58], do not address issues associated with the transient development of the electrical potential across the microchannel or consider the effects of charges present on the inlet and outlet of the capillary.

The necessity for detailed modeling of electrokinetic flow in narrow capillary channels was also perceived over four decades ago in the context of transport of electrolytes through reverse osmosis, ultrafiltration membranes and porous media [61]. It is well known that transport of an electrolyte through membrane pores results in a rejection of the ions, yielding a lower electrolyte concentration in the solution emerging from the pore. The space charge model was an outcome of the initial efforts at analyzing the transport of ions through narrow porous media, neglecting the entrance and exit effects [61–64]. Subsequently, appropriate conditions at the inlets or exits of a finite length capillary based on equilibrium thermodynamic partitioning effects [65–67] were developed. More recently, a considerable body of studies employing the so-called one-dimensional extended Nernst-Planck equations [68–72] have been used to study ion transport and rejection by membrane pores. Once again, most of these modeling approaches are based on steady-state analysis.

Electrokinetic flow in microchannels and transport through membrane pores are governed by the same fundamental equations, namely, the Navier-Stokes equations for the fluid flow, the Nernst-Planck equations for the ion transport, and the Poisson equation for the electrical potential and field distributions. Both types of transport problems essentially attempt to emulate a physical picture shown in Fig 2.1, where a capillary connects two reservoirs containing bulk electrolytes. However, when one scans the theoretical developments in these two areas, a couple of major discrepancies are encountered between the modeling approaches adopted to describe the physical system. These discrepancies can be summarized as described below.

Most of the analytical models for electrokinetic flow assume an infinitely long capillary, and ignore any axial variation of ion concentrations in the capillary [17, 42]. Such assumptions allow the use of a stationary radial ion concentration distribution in the capillary, which is obtained from the solution of the one-dimensional Poisson-Boltzmann equation. Most analytical solutions, and sometimes numerical simulations, of electrokinetic transport processes are obtained employing the undisturbed ion concentration profiles based on the Poisson-Boltzmann equation. The obvious limitation of such an approach is its inability to predict any axial concentration variation [39], and hence, any rejection of ions by the capillary. In contrast, the extended Nernst-Planck models applied to study ion transport through membrane pores predict a substantial axial variation of the ion concentrations in the capillary, and hence, a salt rejection.

The second discrepancy is related to the time scales required for achieving steady state in the electrochemical transport process. According to the electrokinetic theories [43, 58], the steady state streaming potential is attained within the time scales of the hydrodynamic relaxation. In contrast, the extended Nernst-Planck approach predicts establishment of the steady state over the time scale of ions diffusion. The diffusion time scale is several orders of magnitude greater than the hydrodynamic time scale. This leads to the question as to what is the true time scale for attainment of steady state during electrokinetic flow through narrow capillaries.

Considering the geometry of Fig. 2.1, the discrepancies between the two approaches, namely, streaming potential flow and transport through membrane pores, might appear to be an artifact of the boundary conditions prescribed in the exit reservoir. In analysis of streaming potential flow, it is more pertinent to use electroneutral electrolyte solutions of identical concentrations in both the inlet and exit reservoirs. In membrane transport problems, the concentration of the electrolyte solution in the exit reservoir is variable, and the commonly used boundary condition at the outlet reservoir boundary is that of a purely convective ion flux [72]. Such an approach allows establishment of a salt concentration in the outlet reservoir (also termed as the permeate), which is different from the inlet (or feed) reservoir, and allows calculation of the salt rejection. Furthermore, when implementing the extended Nernst-Planck approach, one solves the Navier-Stokes equations independently to obtain the pressure-driven velocity, and thus, completely decouples the convective transport from the electrokinetic transport model. Finally, the models of membrane transport often employ hindered diffusivities of the ions in the channels. However, the question as to whether use of such different boundary conditions, decoupled flow and ion transport equations, or different diffusivities indeed give rise to the discrepancies between streaming potential models and membrane transport models remains unexplored.

A straightforward resolution of the discrepancies between the streaming potential models and membrane transport models delineated above can be achieved through a coupled solution of the transient electrochemical transport equations for the geometry depicted in Fig. 2.1. Such a geometry allows exploration of the ion transport behavior in a finite length capillary, with different types of boundary conditions imposed at the outlet reservoir. More specifically, the geometry obviates the requirement of specifying the boundary conditions directly at the capillary entrance and exit. Furthermore, the transient solution can provide considerable insight regarding the time scales for the development of steady state flow characteristics. In this chapter, we describe such a transient solution of the electrochemical transport equations with an objective of assessing the common features of streaming potential flows and transport through membrane pores. The results from the numerical solutions of the governing equations also provide considerable insight regarding the deficiencies in the existing modeling approaches, and how such limitations yield slightly misleading viewpoints regarding the time scales of the flow development.

This chapter is organized as follows. First, the modeling approach is described, with descriptions of the modeling geometry, the governing equations and their non-dimensional forms, the pertinent boundary conditions, and the simulation parameters. Second, we describe the numerical solution methodology, and provide a validation of the steady-state numerical model by comparing the velocity profiles and streaming potentials against available analytical results. Third, the transient solutions of the governing equations are presented, showing how the electrical parameters and ion concentration distributions evolve with time. Following this, the implications of the transient results are discussed in light of existing understanding of electrokinetic flow through narrow capillaries

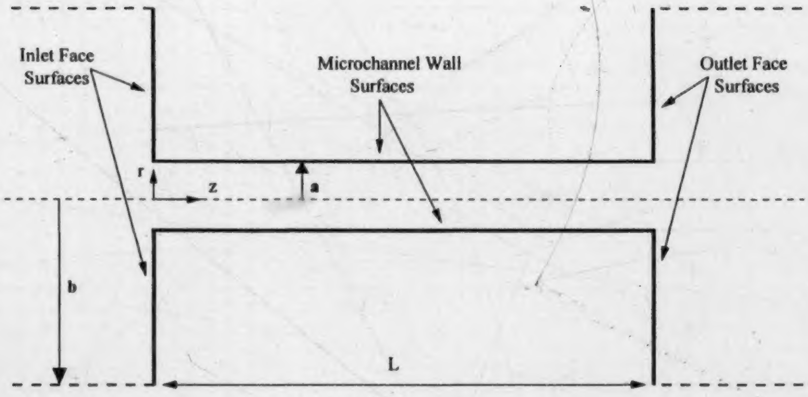
Inlet Face Surfaces
Microchannel Wall Surfaces
Outlet Face Surfaces
r
z
a
b
L

Figure 2.1: Schematic of microchannel pressure-driven flow geometry

and the affects of having charged inlet and outlet surfaces. Finally, the key conclusions from the present study are summarized.

2.2 Problem Statement

2.2.1 Geometry

The flow of an aqueous electrolyte solution is simulated between two reservoirs connected by a straight circular cylindrical microchannel of radius "a" and length "L" as shown in Fig. 2.1. This geometry captures the charge on the front and back surfaces besides those inside the channel surface. The key reason for using this geometry is to avoid formulation of artificial boundary conditions at the capillary inlet and outlet. Instead, this model allows for development of the appropriate entrance and exit conditions at the capillary entrance and exit, originating from the "bulk" conditions, which are defined sufficiently far away from capillary entrance or exit into the reservoirs. To our knowledge, the incorporation of the bulk reservoirs in this manner was first addressed in a recent study by Daiguji *et al.* [59]. However, their analysis involved a steady state problem.

2.2.2 Governing Equations

The hydrodynamic problem is modeled in the framework of the Navier-Stokes (N-S) equations. The general form of the N-S equations with an electrical body force, typically used in electrokinetic problems, is

$$\rho(\frac{\partial \mathbf{u}}{\partial t} + \mathbf{u} \cdot \nabla \mathbf{u}) = -\nabla p + \mu \nabla^2 \mathbf{u} - \rho_c \nabla \psi \tag{2.1}$$

where ρ is the fluid density, $\mathbf{u} = (u, v)$ is the velocity vector with u and v being the radial and axial components, respectively, μ is the viscosity, ρ_c is the net electrical charge density (charge per unit volume), and ψ is the electrical potential. It should be noted that as the Reynolds number is small, the convective term in the N-S equation can be ignored.

For calculation of ion transport and charge distribution, the Poisson-Nernst-Planck equations (PNP) were used. The charge density was related to the electrical potential by the Poisson equation

$$\nabla^2 \psi = -\frac{\rho_c}{\epsilon} , \tag{2.2}$$

where ϵ is the dielectric permittivity of the liquid, and

$$\rho_c = \sum \nu_i e n_i,$$

where ν_i is the valence of the i^{th} ionic species, e is the elementary charge and n_i is the ionic number concentration of the i^{th} species. As we are dealing with very dilute solutions (*e.g.*, 10^{-5}M), permittivity and other fluid properties are considered to be uniform and constant in the domain.

Ion transport in the electrolyte solution subjected to induced electrical fields is described by the Nernst-Planck equation

$$\frac{\partial n_i}{\partial t} = -\nabla \cdot \mathbf{J}_i \ , \tag{2.3}$$

Here $\mathbf{J}_i$ is the ionic flux vector and n_i is the ionic concentration. The total flux of ions in the solution is represented as a sum of convective, diffusive, and migratory fluxes, given by

$$\mathbf{J}_i = n_i \mathbf{u} - D_i \nabla n_i - \frac{\nu_i e n_i D_i}{k_B T} \nabla \psi \tag{2.4}$$

In Eq. (2.4), D_i and ν_i are the diffusivity and valence of the i^{th} ionic species, respectively, T is the temperature, and k_B is the Boltzmann constant.

It should be emphasized here that in our simulations, all time dependent terms are retained in the governing transport equations and the transient behavior of the system is tracked from an initially quiescent state (corresponding to zero flow) until the steady state flow conditions are attained.

Table 2.1: Nondimensional and scaled parameters

Pressure	$\bar{p}$	$\frac{\nu^2 e^2}{\epsilon k_B^2 T^2 \kappa^2} p$
Velocity	$\bar{\mathbf{u}}$	$\frac{1}{\kappa D} \mathbf{u}$
Ion concentration	$\bar{n_p}$,$\bar{n_n}$	$\frac{n_i}{n_\infty}$
Density	$\bar{\rho}$	$\frac{\nu^2 e^2 D^2}{\epsilon k_B^2 T^2} \rho$
Viscosity	$\bar{\mu}$	$\frac{\nu^2 e^2 D}{\epsilon k_B^2 T^2} \mu$
Time	τ	$\kappa^2 D t$
Electric Potential	ψ_d	$\frac{\nu e}{k_B T} \psi$
Free Charge Density	$\bar{\rho}_c$	$\nu e n_\infty (\bar{n_p} - \bar{n_n})$
Diffusivity	$\bar{D}$	$\kappa^2 D$
Surface Charge Density	$\bar{\sigma}$	$\frac{\nu e}{\kappa \epsilon T k_B} \sigma$
Gradient	$\bar{\nabla}$	$\kappa^{-1} \nabla$
Radial Coordinate	$\bar{r}$	$r \kappa$
Streamwise Coordinate	$\bar{z}$	$z \kappa$

2.2.3 Non-Dimensional Equations

To facilitate the transient solution, and to accommodate consideration of the electric double layer effects in the simulations, all the governing equations were non-dimensionalized employing a slightly different approach from other studies [60]. The characteristic length for this study is chosen to be the Debye length, κ^{-1}. The definition of the Debye length for a symmetric ($\nu : \nu$) binary electrolyte is

$$\kappa^{-1} = \left(\frac{\epsilon k_B T}{2 n_\infty e^2 \nu^2} \right)^{1/2} \tag{2.5}$$

All length parameters are scaled with respect to the Debye length. The scaled parameters used in the present model are shown in Table 2.1. It should be noted that we also assume the diffusivities of the different ions in the electrolyte solution to be equal (henceforth we will write $D_i = D$). While it is quite straightforward to incorporate different diffusivities of ions in the numerical model, we use a single diffusivity in our subsequent analysis to ensure facile comparison of the numerical results with existing analytical solutions.

By substituting the non-dimensionalized parameters into the momentum equation and ignoring the inertia term, one can obtain the non-dimensional form of the Navier-Stokes equation

$$\bar{\rho} \frac{\partial \bar{\mathbf{u}}}{\partial \tau} = -\bar{\nabla} \bar{p} + \bar{\mu} \bar{\nabla}^2 \bar{\mathbf{u}} - 0.5(\bar{n_p} - \bar{n_n}) \bar{\nabla} \psi_d \tag{2.6}$$

The non-dimensional form of the Poisson equation (2.2) is

$$\bar{\nabla}^2 \psi_d = -0.5(\bar{n}_p - \bar{n}_n) \ , \tag{2.7}$$

where $\bar{n}_p$ and $\bar{n}_n$ are the scaled concentrations of the ions. It should be noted that since the Poisson equation has no time dependent term, the transient development of the electric potential is based solely on the transient behavior of the ion concentration distribution.

Using the scaled parameters from Table 2.1 and considering $\bar{D} = \kappa^2 D$ $[s^{-1}]$, one can non-dimensionalize the Nernst-Planck equation for each ionic species. For the positive ions, the governing equation is

$$\frac{\partial \bar{n_p}}{\partial \tau} = -\bar{\nabla} \cdot \left(\bar{n_p}\bar{\mathbf{u}} - \bar{\nabla}\bar{n_p} - \bar{n_p}\bar{\nabla}\psi_d \right) , \tag{2.8}$$

while for the negative ions, we write

$$\frac{\partial \bar{n_n}}{\partial \tau} = -\bar{\nabla} \cdot \left(\bar{n_n}\bar{\mathbf{u}} - \bar{\nabla}\bar{n_n} - \bar{n_n}\bar{\nabla}\psi_d \right) , \tag{2.9}$$

As noted before, the ionic diffusivities (and mobilities) for both positive and negative ions are assumed to be equal.

2.2.4 Boundary and Initial Conditions

Boundary conditions employed for the governing equations are depicted in Fig. 2.2. All governing equations were written in a cylindrical coordinate system (r, θ, z), so that utilizing the symmetry in the θ coordinate, we can recast the problem as an axisymmetric two-dimensional model (r, z). In case of the N-S equation, the boundaries BC and FG in the Fig. 2.2(a) were assigned slip boundary conditions to emulate infinite reservoirs and allow the use of a 1-D uniform velocity and pressure at the boundaries AB and GH. Furthermore, the radius "b" shown in Fig. 2.1 was chosen such that the entry and exit regions of the capillary are sufficiently far away from the bulk reservoir boundaries (AB, BC, FG, and GH). It was observed that by setting $b = 5a$ one has practically vanishing influence of the capillary on these outer boundaries. With respect to the Poisson equation, on BC, FG and GH, the potential gradient is set to zero. The potential on AB is also set to zero. Once again, these boundaries represent the "bulk" conditions far from the inlet and exit of the capillary. Constant charge density conditions (-0.00019 μC/cm^2 (-1.04 nondimensional) is equivalent to a surface potential of -25 mV in the one-dimensional semi-infinite case of a solid-fluid interface) were applied on CD, DE and EF in most of the simulations. The constant surface potential boundary condition was only used for the validation of the numerical calculations against analytical results. For the Nernst-Planck equation, it was assumed that a flow with bulk concentration ($\bar{n}_p = \bar{n}_n = 1$) enters the channel at AB. At the exit boundary, GH, we impose two different types of boundary conditions. First, to emulate typical streaming potential flow conditions, the bulk ion concentrations were defined on GH as $\bar{n}_p = \bar{n}_n = 1$ (identical to the inlet boundary conditions). Secondly, to emulate the conditions employed in membrane transport problems, a normal outwardly directed convective flux ($\mathbf{J}_{exit} = \bar{n}_i\mathbf{u}$) condition was used at the boundary GH, implying that no concentration or electric potential gradient exists normal to GH. For all three equations, axial symmetry was imposed on the boundary AH.

A majority of the calculations were performed using a value of $\kappa a = 5$, which means that the capillary radius is five times the Debye length. The scaled radius of the inlet and outlet manifolds (r_d in Fig. 2.2) was five times the scaled capillary radius. The scaled length of the capillary (DE) was 50, giving a length to diameter ratio of 5. Finally, the scaled length of the inlet and outlet manifolds (BC and FG) was 25, yielding a total length of the capillary and manifolds (AH) of 100. For the transient flow simulation, the no flow, steady state results were used as initial conditions. Using the no flow equilibrium state

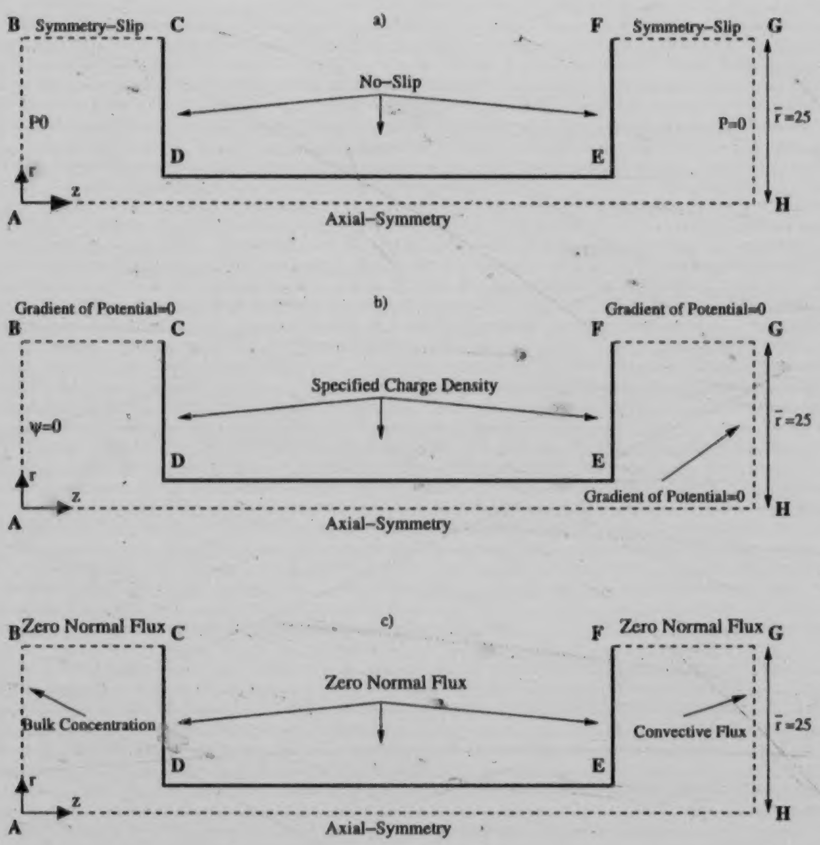
a)
B
Symmetry–Slip
C
F
Symmetry–Slip
G
No–Slip
P0
P=0
r̄ =25
D
E
r
z
A
H
Axial–Symmetry
b)
Gradient of Potential=0
B
C
Gradient of Potential=0
F
G
Specified Charge Density
ψ=0
r̄ =25
D
E
Gradient of Potential=0
r
z
A
H
Axial–Symmetry
c)
B
Zero Normal Flux
C
F
Zero Normal Flux
G
Zero Normal Flux
Bulk Concentration
Convective Flux
r̄ =25
D
E
r
z
A
H
Axial–Symmetry

Figure 2.2: Boundary Conditions for (a) N-S equation (b) Poisson equation and (c) Nernst Planck equations

as the initial conditions allows the question of how streaming potential and ion rejection come into existence in establishing a new equilibrium state under steady flow conditions. The following physical parameters were employed in the calculations: $e = 1.6021 \times 10^{-19}$ C, $n_\infty = 6.022 \times 10^{21} 1/\mathrm{m}^3$, $\epsilon = 78.5 \times 8.854 \times 10^{-12}$ CV^{-1}m^{-1}, $T = 298$ K, $\nu = 1$, $-\frac{\partial p}{\partial z} = 10^7$ Pa m^{-1}, $\rho = 10^3$ kgm^{-3}, $D = 10^{-9}$ m^2/s and $k_B = 1.38 \times 10^{-23}$ JK^{-1}.

2.3 Numerical Methodology and Validation

2.3.1 Numerical Solution Methodology

All governing equations were solved using finite element analysis employing a commercial code, Femlab(COMSOL Inc). The solution methodology involved a segregated solution of the Poisson-Nernst-Planck (PNP) and the N-S equations at the first time step, following which both sets of equations were solved in a coupled manner. At the outset ($t = 0$), the PNP equations were solved for the stationary case (no fluid flow) to determine the equilibrium distribution of the electric potential and the ion concentrations over the computational domain. Using the electric fields and the charge densities obtained from the PNP equations to compute the electrical body force, the N-S equations were then solved to obtain the velocity profile using the applied pressure gradient. Following this initial step, all the governing equations *i.e.*, Eqs. 2.6 - 2.9 were solved together in a time dependent mode. The transient solution was repeated for incremental time steps until the electrical potential difference between the two reservoirs obtained at two consecutive time steps became identical (to within a preset tolerance). This final value was considered to be the steady-state result. The steady state potential distribution obtained from the above transient solution procedure was compared against a steady-state simulation result obtained independently from the solution of the steady-state versions of the governing equations (by disregarding the time dependent terms). The simulations were performed on a personal computer with 1GB RAM and 3GHz processor.

The finite element calculations were performed using quadratic triangular elements. The mesh was refined near the channel walls as well as the channel centerline. The accuracy of the numerical results was strongly dependent on the finite element mesh. With respect to mesh sensitivity of the solution, one needs to consider two features of the coupled solution. First, near the channel wall, where the electric potential gradients are pronounced, a refined mesh is necessary to ensure accurate estimation of these potential gradients. Secondly, near the channel centerline, where the velocities are pronounced and critically depend on the accuracy of the electrical body force term, one needs to have a sufficiently refined mesh to capture the subtle changes in the electric field. Consequently, in our calculations, a finer mesh was used near the channel walls as well as along the center of the microchannel. Independence of the results to mesh refinement was studied and all results reported here are independent of measurable influence of mesh size. It was observed that the solution became mesh independent with approximately 10,000 elements. The results presented in this work were all obtained using a mesh containing 10,000 to 30,000 elements.

2.3.2 Analytical Model for Low Surface Potentials

To validate the finite element formulation, we compared the predictions from the steady-state numerical model against existing analytical results for streaming potential flow in an infinitely long capillary. The analytical results were obtained for the transport of a symmetric electrolyte in a straight circular cylindrical capillary of infinite length with low surface potentials on the capillary wall ($\nu e\psi_w/k_BT << 1$) [17, 42, 44]. Here we summarize the key steps of the pertinent derivation.

For low potentials and symmetric electrolytes, one can obtain the radial electric potential distribution employing the linearized Poisson-Boltzmann equation

$$\frac{1}{r}\frac{d}{dr}\left(r\frac{d\psi}{dr}\right) = \kappa^2\psi \tag{2.10}$$

with boundary conditions of $\psi = \psi_w$ at $r = a$ (at capillary wall) and $d\psi/dr = 0$ at $r = 0$ (capillary centerline). The solution of Eq. 2.10 subject to the above boundary conditions yields

$$\psi(r) = \psi_w \frac{I_0(\kappa r)}{I_0(\kappa a)} \tag{2.11}$$

for the electric potential distribution, where I_0 refers to the modified Bessel function of zeroth order of the first kind, and

$$\rho_e(r) = -\epsilon_r \epsilon_0 \kappa^2 \psi_w \frac{I_0(\kappa r)}{I_0(\kappa a)} \tag{2.12}$$

Incorporating the above solution for the linearized Poisson-Boltzmann equation in the momentum equation (corresponding to the axial flow), one can write

$$\mu\frac{1}{r}\frac{d}{dr}\left(r\frac{dv}{dr}\right) = -p_z + \epsilon_r \epsilon_0 \kappa^2 \psi_w \frac{I_0(\kappa r)}{I_0(\kappa a)} E_z \tag{2.13}$$

where $p_z = -dp/dz$, and E_z is the electric field component acting in the z direction. Using the no-slip condition at the channel wall ($v = 0$ at $r = a$) and utilizing the axial symmetry ($dv/dr = 0$ at $r = 0$), the solution of Eq. (2.13) is

$$v(r) = \frac{a^2 p_z}{4\mu}\left[1 - \left(\frac{r}{a}\right)^2\right] - \frac{\epsilon_r \epsilon_0 \psi_w}{\mu}\left[1 - \frac{I_0(\kappa r)}{I_0(\kappa a)}\right] E_z \tag{2.14}$$

Neglecting concentration gradients in the axial direction, and hence, the axial diffusion, the total current in the channel is given as a sum of the streaming and conduction (migration) currents as

$$I = 2\pi \int_0^a v\rho_c \, r dr + \frac{4\pi\nu^2 e^2 D n_\infty E_z}{k_B T} \int_0^a \cosh\left(\frac{\nu e \psi}{k_B T}\right) r dr \tag{2.15}$$

or

$$I = 2\pi \int_0^a v\rho_c \, r dr + \pi a^2 \sigma^\infty E_z F_{cc} \tag{2.16}$$

where $\sigma^\infty = 2\nu^2 e^2 D n_\infty/(k_B T)$ is the bulk electrolyte solution conductivity and

$$F_{cc} = 2 \int_0^1 \cosh\left[\frac{\nu e \psi_w}{k_B T} \frac{I_0(\kappa a) \cdot R}{I_0(\kappa a)}\right] R dR \tag{2.17}$$

with $R = r/a$. The factor F_{cc} is a correction accounting for the conduction current through the electrical double layer. When $F_{cc} = 1$, the conduction current becomes constant across the channel cross section. In most traditional analysis of streaming potential [42], the term F_{cc} is assigned a value of unity, which is a valid assumption for sufficiently large κa. F_{cc} is usually greater than unity for small κa.

At steady state, setting the net current to zero, one obtains the following condition [17]

$$\left(\frac{E_z}{P_z}\right)_{I=0} = \frac{\Omega}{\sigma^\infty F_{cc}} f(\kappa a, \beta), \tag{2.18}$$

where

$$\Omega = \frac{\epsilon \psi_w}{\mu}, \quad \beta = \frac{\Omega^2 \mu \kappa^2}{\sigma^\infty F_{cc}}$$

and

$$f(\kappa a, \beta) = \frac{(1 - \frac{2A_1}{\kappa a})}{1 - \beta(1 - \frac{2A_1}{\kappa a} - A_1^2)},$$

In the above expression for f, the term $A_1 = I_1(\kappa a)/I_0(\kappa a)$, where I_0 and I_1 are zeroth and first order modified Bessel functions of the first kind.

Equation (2.18) provides the conditions for the streaming potential flow. For a known applied pressure gradient, Eq. (2.18) provides the axial electric field engendered by the pressure-driven flow. From this field, one can determine the potential difference set up across the capillary, which is the streaming potential.

2.3.3 Comparison of Numerical and Analytical Results

The analytical approach described above employs several assumptions. These include application of the linearized Poisson-Boltzmann equation, linear superposition of axial and radial electric fields, neglecting the axial concentration gradients, and ignoring the entrance/exit effects. In the numerical model, none of these assumptions were made. Consequently, comparison of the numerical and analytical results is not straightforward. Nevertheless, if we focus our attention to the mid-section of the capillary (corresponding to $\bar{z} = 50$), which is sufficiently removed from the channel entrance and exit regions, it is likely that the local conditions at this section from our numerical results will closely emulate those existing in an infinitely long capillary. Therefore, we first compare the axial velocity profile obtained from the numerical simulation at $\bar{z} = 50$ with the corresponding velocity profile obtained using Eq. (2.14). Note that to compare the velocity profiles, one will need to employ values of E_z and p_z in Eq. (2.14) that are identical to the values of these parameters at the mid-plane of the numerical solution.

To perform the comparison of the velocity profiles, we conducted the numerical simulation for $\kappa a = 1, 5$, and 9 using a constant surface potential of -25 mV ($\bar{\psi}_w = -1$) at the capillary wall. On the entrance and exit faces (CD and EF), the surface potential was set to zero. From the steady-state solution

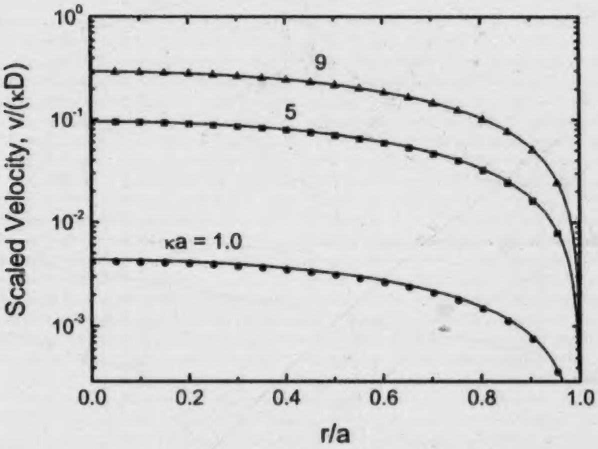

Figure 2.3: Comparison of the velocity profiles at the mid-plane ($\bar{z} = 50$) of the capillary microchannel. Solid lines are the predictions obtained from Eq. (2.14) while symbols are predictions from the numerical simulations. Results are shown for three values of scaled capillary radius.

of the governing equations, the values of p_z and E_z at $\bar{z} = 50$ and $\bar{r} = 0$ were determined. These values were then substituted in Eq. (2.14) to calculate the analytical velocity profile. The comparison of the numerical and analytical velocity profiles is shown in Fig. 2.3. It is evident from the figure that the velocity profile obtained numerically at the mid section of the channel ($\bar{z} = 50$) is in remarkably good agreement with the velocity profile obtained for an infinitely long cylindrical capillary using the analytical procedure.

The streaming potential in most experimental devices is recorded as the potential difference between the two reservoirs connecting the capillary. In the numerical simulations, a similar potential difference is set up between the two reservoirs at steady state, as shown in Fig. 2.4a. Figure 2.4a depicts the variation of the scaled potential with axial location along the centerline of the capillary ($\bar{r} = 0$) obtained for $\kappa a = 5$ and a scaled surface potential of -1

on the capillary wall. In the analytical calculations, however, one does not have a direct means of obtaining the streaming potential since the analytical model does not consider the reservoirs, and is applicable for an infinitely long capillary. Equation 2.18 only provides the ratio of the electric field and the pressure gradient that should exist at steady state for the streaming potential flow conditions. It is therefore instructive to explore how the potential difference obtained across the capillary in the numerical calculations, as shown in Fig. 2.4a, relates to Eq. (2.18).

To calculate a potential difference over a given length of the capillary using the analytical approach, the right hand side of Eq. (2.18) was evaluated employing identical capillary radius and other conditions applied to our numerical simulations. In these calculations, the value of F_{cc} was set to 1.0. From the numerical simulation, the pressure difference, Δp across a given axial distance (say L) was computed. Dividing this pressure difference by L provided the pressure gradient, $p_z(= \Delta p/L)$. Using the pressure gradient in Eq. (2.18) we then obtained the axial electric field, E_z. This value of the field was employed to calculate the potential difference over the length L using

$$\Delta\psi = E_z L$$

The potential difference thus calculated using the analytical expression, Eq. (2.18), is compared with the potential difference between the two reservoirs obtained from the numerical simulations for different values of scaled capillary radius κa in Fig. 2.4b. One should note that the comparison is based on the parameters evaluated along the centerline of the capillary. Accordingly, in the analytical calculations, we set $F_{cc} = 1$. Under these conditions, it is evident from Fig. 2.4b that the numerically and analytically evaluated potential differences across the capillary are in remarkably good agreement. The numerical results slightly overpredict the potential difference for lower values of κa. However, for $\kappa a \geq 5$ the two predictions are virtually identical.

The excellent agreement between the numerical and analytical results not only serves as a validation of the numerical model, but also provides considerable insight regarding the development of streaming potential across charged capillaries. First, the comparison of the two solutions were performed on the basis of conditions, particularly the velocities, determined at the mid-section of the capillary. Secondly, the streaming potential in the analytical solution was based solely on the streaming and conduction current, whereas in the numerical calculations, it was obtained considering all three modes of ion transport (convection, diffusion, and migration). Finally, the results corresponding to the channel centerline in the numerical simulation matches with the streaming potential obtained from the analytical results determined by ignoring any surface conductance effects (this is reflected in the use of the factor $F_{cc} = 1$ in the analytical solution).

It is of interest to determine the influence of the exit boundary conditions (defined at the plane GH) on the steady-state axial ion concentration distributions in the system and the streaming potential. Figure 2.5 depicts the variations of the ion concentrations and the electric potential along the centerline of the channel ($\bar{r} = 0$). The results are shown for a non-dimensional capillary radius of 5.0. It is evident from Fig. 2.5a that the axial variations of the ion concentrations are markedly different depending on the types of boundary conditions used in the model. However, the axial variation of the electrical potential obtained using the two boundary conditions (Fig. 2.5b) are quite similar in the inlet reservoir and the capillary. The potential in the outlet reservoir is slightly higher when the convective flux boundary condition is employed at the exit plane of the

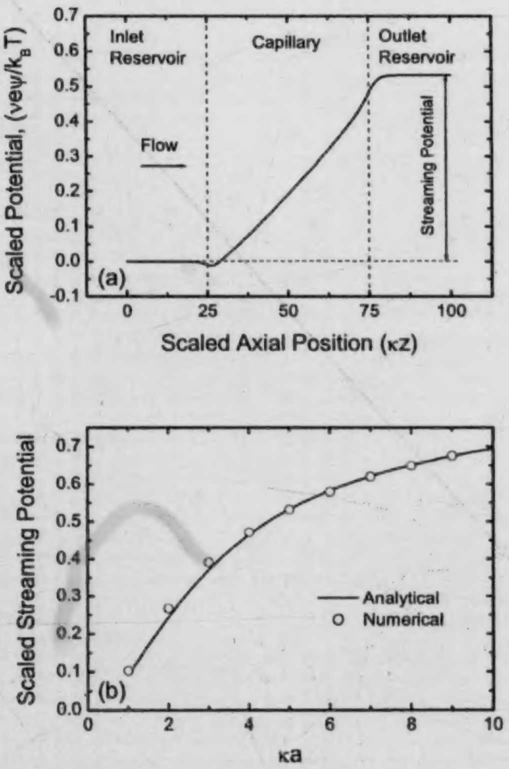

Figure 2.4: (a) Variation of the scaled electric potential with scaled axial position along the capillary centerline ($\bar{r} = 0$). The vertical dashed lines are the demarcations between the inlet reservoir, the capillary, and the outlet reservoir. The potential difference between the inlet and outlet reservoirs is denoted as the streaming potential. The result was obtained for $\kappa a = 5$. (b) Comparison of the numerical and analytical predictions of the streaming potential for different κa. See text for details.

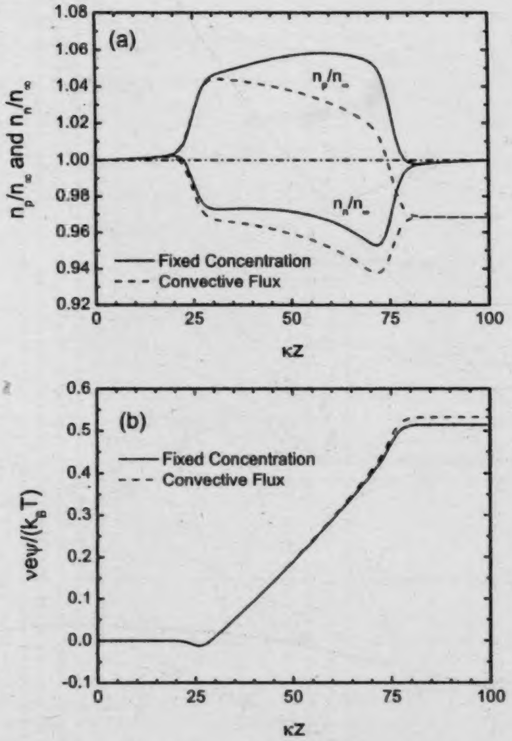

Figure 2.5: Influence of the exit plane boundary condition (at the plane GH in Fig. 2.2) on (a) ion concentration and (b) electric potential distributions along the capillary centerline ($\bar{r} = 0$). The results were obtained for $\kappa a = 5$.

system. A key feature of Fig. 2.5a is the pronounced axial variation of the ion concentrations. Such variations are not accounted for in the analytical models of electrokinetic flows based on the Poisson-Boltzmann equation. Consequently, Figs. 2.4b and 2.5a indicate that while the steady state streaming potentials obtained using the analytical approach and the detailed numerical simulations are very similar, the corresponding axial concentration variations are portrayed very differently in the analytical and numerical approaches.

2.4 Development of Streaming Potential: Transient Study

2.4.1 Transient Electrochemical Transport Behavior

In this section, we initially focus on how the electrokinetic flow is developed starting from an initially quiescent system after application of an axial pressure gradient. The first step in this analysis involves setting up the initial electric potential and ion concentration distributions in a charged capillary connecting two electrolyte reservoirs. The Poisson Nernst-Planck equations were solved using a zero velocity field to obtain these stationary distributions corresponding to $t = 0$. The simulations were performed for constant surface charge density on the capillary wall (DE) as well as on the entrance and exit faces of the wall (CD and EF). The scaled surface charge density was computed using the relationship

$$\bar{\sigma}_w = 2\sinh(0.5\bar{\psi}_w)$$

where $\bar{\psi}_w$ is the scaled surface potential of the capillary wall, taken to be -1. Once the initial distributions were obtained, the pressure gradient was applied across the capillary and the transient Navier-Stokes equations were solved fully coupled with the PNP equations starting from an initially quiescent system. The time stepping was performed using a backward difference scheme. The solution of the coupled NS and PNP equations were stored at regular time intervals. Finally, in these and all subsequent simulations, we employ the convective flux boundary condition on the exit plane of the channel (GH). The convective flux boundary condition is commonly employed in models of transport through membrane pores, and does not require specifying the electrolyte concentration in the outlet reservoir. It was also shown earlier that the difference in streaming potentials obtained by setting the outlet reservoir ion concentration equal to the inlet reservoir ion concentration and by employing the convective flux boundary condition is not substantial for the range of parameters studied.

The transient simulations were performed using a scaled time, τ, which is represented as $\kappa^2 Dt$, where t is the dimensional time. For the typical simulation parameters used in this study, a real time of 1 μs will yield $\tau = 0.1$. The above time scaling employs the diffusion time scale $\kappa^2 D$. If one were to non-dimensionalize the governing equations employing the time scale of the hydrodynamic relaxation, a convenient approach would have been to employ the pertinent hydrodynamic relaxation time scale, commonly represented as $\mu/(\rho a^2)$, where a is the capillary radius [58]. For aqueous solutions and a capillary radius of about 0.5 μm, the hydrodynamic relaxation time based on the above scaling becomes about 0.25 μs. Using the above definitions, one can assess the time scales of evolution of the electrochemical transport variables employing the values of τ reported in the following discussion.

Figure 2.6 depicts the predictions of the transient model spanning the initial stages of the developing electrokinetic flow. The figure depicts the scaled axial variations of the electric potential (2.6a), axial electric field component (2.6b), and concentrations of the co- and counter-ions (2.6c and d, respectively) along the capillary center line at different values of scaled time, τ, ranging from 0 to 10. The initial quiescent condition is depicted by the lines denoted by $\tau = 0$, while the final steady-state predictions are shown by the dashed lines. We note from Fig 2.6a and 2.6b that during the initial stages of the electrochemical transport process, the electrical parameters, namely, the potential and the field, undergo a major transition from the initial quiescent profiles to values very close to the steady-state results. It is, however, interesting to note that over the same time span, the corresponding ion concentration profiles (Figs. 2.6 c and d) show negligible variations from the initial quiescent profiles. All the solid lines in Fig.

2.6 c and d virtually superimpose. Thus, although the electrical parameters in the transient solution attain values that are within 10% of the final steady-state behaviour by $\tau = 10$, the ion concentrations do not even deviate measurably during this period.

The variation of the key electrochemical parameters over the later stages of the transient solution are depicted in Fig. 2.7. The layout of the figures are identical to Fig. 2.6, except for the different time range shown ($\tau = 50$ to 10000). At larger values of τ, we observe a transport that is exactly opposite to the phenomena observed in Fig. 2.6. In this case, the electric potential and the axial field component do not change substantially, although the ion concentration profiles undergo a dramatic nonlinear transition toward the final steady state values. A closer inspection of Figs. 2.7 c and d reveals that the concentration profiles of the ions at certain regions inside the capillary undergo a slow inversion with time. For $\tau < 1000$, the concentration of both co- and counter-ions increase in the leading section of the capillary, while for $\tau > 1000$, the concentration starts decreasing again. It is also remarkable that even at a scaled time of 10000, which roughly corresponds to about 0.1 s, the ion concentrations in the downstream reservoir are markedly different from the steady state concentrations. Our simulations show that it takes on the order of one second to attain the steady-state concentrations in the downstream reservoir.

The transient behavior of the electrochemical transport process described above clearly depicts an initial development of the electrical parameters followed by a more gradual and long term relaxation of the ion transport parameters associated with diffusion and migration. The potential difference across the capillary, or the transcapillary potential, attains values that are within 10% of the steady-state streaming potential within a very short time. Following this, the approach to the streaming potential slows down dramatically, and this process is primarily dictated by the dynamics of the ion transport in the system. The time at which the electrical potential reaches a steady-state value is not precisely known, although our simulations suggest that this steady-state potential difference is established in the order of 0.1 to 1 s. This time scale is several orders of magnitude larger than the time scale for the establishment of the purely hydrodynamic steady-state. We wish to point out here that reaching the hydrodynamic steady state *i.e.*, when the variations of pressure drop and flow rate with time are negligible, does not necessarily imply that the electrical potential difference across the channel has reached its steady-state value. The steady-state streaming potential is attained only when there is no net current.

The above discussion brings out a serious deficiency in existing analytical approaches for evaluating the transient electrokinetic flow behavior [43, 58]. These analytical approaches assume the existence of a stationary electric double layer in the channel during electrokinetic flow, and use the Poisson-Boltzmann equation to determine the radial ion distributions in the channel. This procedure completely eliminates any transient ion transport effects from the governing equations, and consequently, the evolution of the streaming potential and associated electrokinetic phenomena become strictly dictated by the time scales of the N-S equations. Such a behavior is clearly evident from the time scales depicted in [58], which are of the order of the hydrodynamic relaxation time. The numerical results presented here show that the attainment of the steady state streaming potential is a markedly complex process, and involves a rapid initial establishment of a potential gradient due to the imposed pressure driven flow, followed by a considerably slower relaxation of the ion concentration distributions in the axial direction. Indeed, the initial stages of the transport process causes negligible distortion of the electric double layer, as is evident from the ion

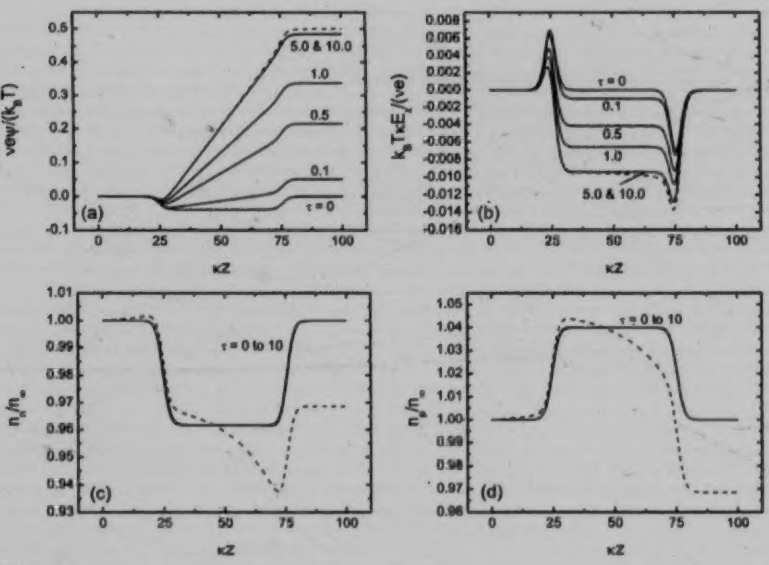

Figure 2.6: Axial variations of the (a) electric potential, (b) field, (c) co-ion concentration, and (d) counter-ion concentration along the capillary centerline ($\bar{r} = 0$) during the initial stages of the transient electrochemical transport. The results were obtained for $\kappa a = 5$. The scaled time is given as $\tau = \kappa^2 Dt$, where t is the time.

concentration profiles of Fig. 2.6. However, the potential difference established across the capillary at this initial stage of electrokinetic flow, while close to the streaming potential, is not representative of a steady-state process.

The present simulations also show how the electric field in the axial direction differs from the simple constant value that one imposes in most analytical solutions. The electric field is negligible in the two reservoirs during streaming potential flow. The field undergoes sharp changes at the capillary entrance and exit, while within the capillary, the field is uniform during the initial stages of the streaming potential development (Fig. 2.6b). At larger times, the electric field in the capillary varies slightly with axial position, as shown in Fig. 2.7.

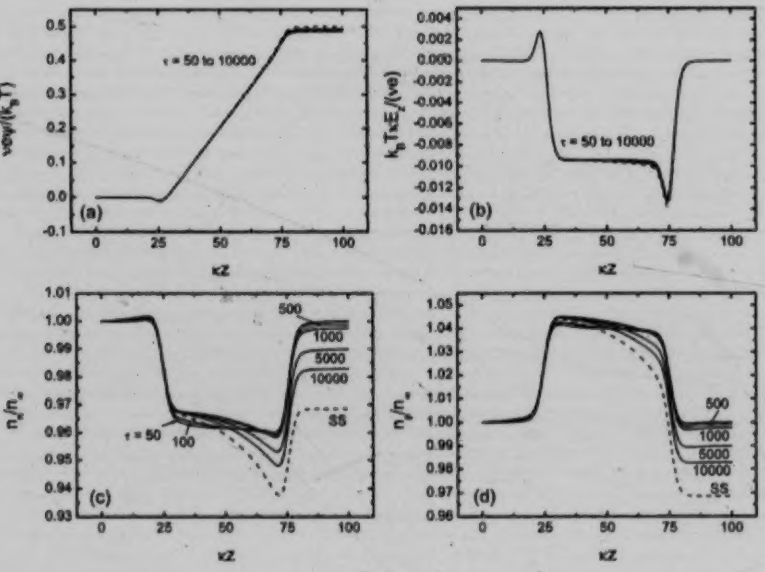

Figure 2.7: Axial variations of the (a) electric potential, (b) field, (c) co-ion concentration, and (d) counter-ion concentration along the capillary centerline ($\bar{r} = 0$) during the later stages of the transient electrochemical transport. The results were obtained for $\kappa a = 5$. The scaled time is given as $\tau = \kappa^2 Dt$, where t is the time.

2.4.2 Ion Concentration Variation with Time

The enormous difference in the timescales for the establishment of a sizeable transcapillary potential difference and the establishment of the steady state axial ion concentration distributions brings us to the question as to what causes the rapid increase in the potential difference at the initial stages. Notably, since the concentration distributions of the ions at different times are virtually indistinguishable from Fig. 2.6, it might appear that there is no variation in net charge transport with time through the capillary during the initial stages of the flow development. To assess how and where the pressure-driven flow influences the ion concentrations during the initial stages of the flow development, we plot the relative concentration differences of the ions from their initial concentrations, at each spatial location given by $[n_p(\tau) - n_p(0)]/n_p(0)$ for the counterions, and $[n_n(\tau) - n_n(0)]/n_n(0)$ for the co-ions. This representation yields a value of zero everywhere at $\tau = 0$ for the ion distribution along the capillary, and registers any subsequent changes of the ion concentration from the initial equilibrium distribution. Figure 2.8 depicts these concentration profiles along the centerline of the capillary at different values of the scaled time. Once again, these simulations were performed for $\kappa a = 5$, with all other conditions identical to those used for Figs. 2.6 and 2.7. Figure 2.8a depicts the relative concentration difference for the counter-ion, while Fig. 2.8b depicts the results for the co-ion.

It is evident from Fig. 2.8 that the ion concentrations do not differ from the initial Poisson-Boltzmann quiescent distribution in the reservoirs or the inner regions of the capillary. Only in the vicinity of the capillary entrance and exit ($\bar{z} = 25$ and 75), a marked change in the concentration distributions are observed. In case of the co-ion (Fig. 2.8b), the variation is registered as two antisymmetric peaks at the entrance and exit regions. These peaks grow in magnitude monotonically over the time interval shown. One should note that a positive peak represents an accumulation of the ion, while a negative peak shows a depletion of the ion. In case of the counter-ion, however, the relative concentration difference undergoes a more complex transition with time. A close inspection of Fig. 2.8a reveals that the peaks in the curves grow up to $\tau = 1.0$, following which, the trend is reversed. For $\tau = 5.0$ we observe that the magnitude of the primary peak has diminished, while a secondary peak appears just within the capillary. At $\tau = 10$, the directions of the peaks are completely reversed, and we observe an accumulation of the counter-ion at the capillary entrance, while the counter-ion is depleted from the capillary exit. It is worth noting, however, that there is no observable change in the ion concentration distribution within the capillary during this initial time period. In other words, there is no net accumulation or displacement of ions within the capillary during the initial stages of streaming potential development. It is the accumulation or depletion of charge at the capillary entrance and exit that gives rise to the transcapillary potential difference.

The foregoing discussion clearly establishes the paramount role of the capillary inlet and exit regions in governing the evolution the streaming potential. The interior regions of a uniformly charged capillary do not perceive any change in ion concentrations during the initial stages of the developing flow. The transcapillary potential solely reflects the altered charges at the capillary inlet and exit. During this initial period, the ion concentration distributions within the capillary (barring the entrance and exit regions) can be very accurately represented in terms of the undisturbed Poisson-Boltzmann distribution, as is done in most analytical models of electrokinetic flow. [42, 43, 58] However, one should note that such a distribution is eventually modified over a much longer period of time as shown in Figs. 2.7c and 2.7d.

To summarize, as soon as an axial pressure gradient is applied, and the fluid flow is set up, the ions are convected in the axial direction. This convection transports an essentially electroneutral solution toward the capillary entrance, which initially had a slight excess of positive charge (owing to the negatively charged walls of the capillary). Consequently, the capillary inlet becomes less positive compared to the initial time. On the other hand, at the outlet of the capillary, the net excess positively charged fluid residing just inside the capillary is convected into the outlet reservoir, resulting in a small excess of positive charge in this reservoir. Such a convective displacement of charge sets up the initial potential gradient between the two reservoirs. Thus, at the initial stages of the electrokinetic flow, convection of ions cause a local perturbation in the charge densities at the inlet and outlet, but not in the capillary itself Fig.2.9.

In the published literature, there are different interpretations of the physical meaning of streaming potential. A common textbook description of the streaming potential is "when a liquid is forced through a microchannel under hydrostatic pressure, the ions in the mobile part of the EDL is transported toward one end of the capillary. The accumulation of ions downstream sets up an electrical field with an electrical potential called streaming potential" [48, 53]. Another description of the phenomenon is, "the phenomena of streaming current and streaming potential occur in general due to the charge displacement in the electrical double layer caused by an external force shifting the liquid phase tangentially against the solid" [24]. While capturing the essence of the streaming potential phenomenon, the above descriptions are primarily based on a steady-state analysis of the electrokinetic transport problem, and hence, they do not provide a complete picture regarding the transient nature of the streaming potential development. Furthermore, the descriptions do not summarize the roles of the different transport contributions to the development of the electrical potential. Most importantly, if we consider the EK flow in the limit of $\kappa a \to \infty$, which is the Helmholtz-Smoluchowski limit, one has problem visualizing any tangential shift of charge causing an electric potential difference across the capillary, since the electrical double layer is almost immobile and no net charge exists in the bulk fluid flowing through the capillary. The calculations for smaller values of κa are clearly more instructive in terms of depicting the net shift in charge.

2.5 Effects of Surface Charge Variation of Microchannel Walls on Streaming Potentials

Given the importance attributed above to the entrance and exit regions in establishing the initial transcapillary potential, it is worth exploring the impact of the magnitude of the charge density on the various surfaces. The simulations conducted in this study employ three different surfaces, which represent the capillary wall, and the walls of the inlet and exit reservoirs (i.e., CD, DE, and EF in Fig.2.2). The charge density on each of these surfaces can be adjusted independently and thereby permit a discussion on their relative importance.

To study the influence of the charge densities of the channel walls on the streaming potential, we first compare the streaming potentials obtained by independently setting the charge densities on the inlet face (CD) and the outlet face (EF) to zero, while retaining the charge density on the capillary wall (DE) fixed. The comparison is shown in Fig. 2.10. The results from these cases are compared with the streaming potential when all the solid surfaces (CD, DE and EF) have the same charge density. It is observed that the electric potential variations along the channel obtained by setting different charge densities on

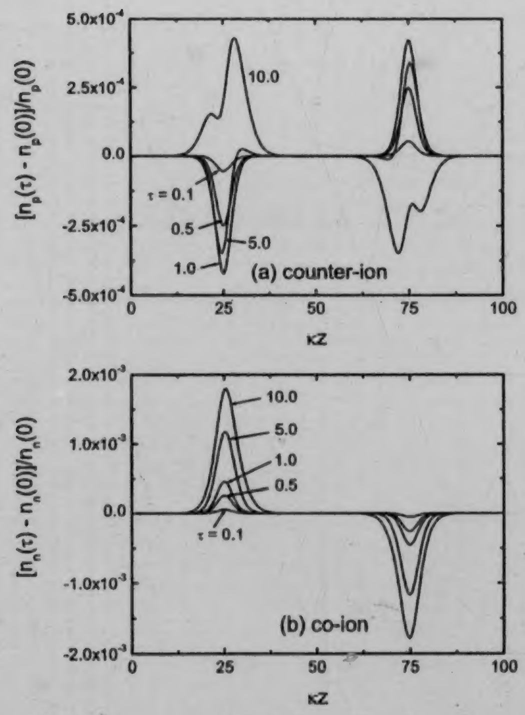

Figure 2.8: Changes in the ion concentrations relative to the initial concentration distribution along the channel centerline ($\bar{r} = 0$) at different instants. (a) counter-ion (positive ion in this case) and (b) co-ion (negative ions). All simulation parameters are identical to those used for Fig. 2.6. Due to near symmetry between inlet and outlet, the time labels are only identified once.

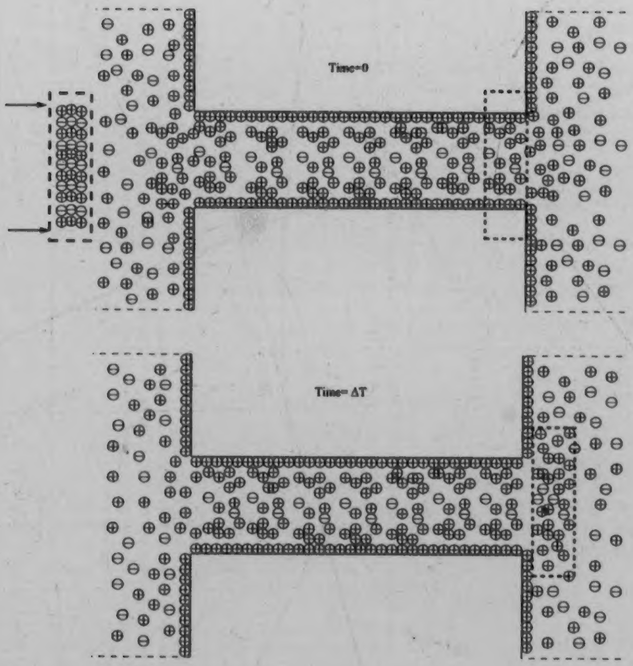

Figure 2.9: Local perturbation in the charge densities at the inlet and outlet of a finite length microchannel. This imbalance of charge manifests itself in Poisson equation and induces a transcapillary potential and conduction current. See text for detail.

the various walls is virtually indistinguishable. However, it should be borne in mind that in all these simulations, the maximum magnitudes of the charge densities were all based on a scaled surface potential of -1, and hence, represent charge variations that are relatively small. In another simulation, we applied zero charge density on the capillary wall, while retaining finite values of the charge density on the entrance and exit faces. The resulting potential distribution is also shown in Fig. 2.10. In this case, the potential difference set up across the capillary is an order of magnitude smaller compared to the potential difference obtained for a charged capillary wall. This indicates that the presence of charge on the capillary wall plays a dominant role in establishment of a transcapillary potential difference. The relative lack of importance of having a charge on either the inlet or exit faces is exploited in Chapter 5 where in experiments these surfaces are coated with a nano-layer of gold to act as electrodes right at the ends of the channel. Caution needs to be applied before generalizing these results to the conclusion that the effects of charge on the inlet and outlet surfaces are negligible, as the results presented here are only for κa=5 (i.e. a channel diameter of 1μm).

2.6 Conclusions

The finite element simulations of the electrochemical transport equations presented in this study identify, and attempt to bridge, some of the gaps in the theoretical approaches employed in traditional electrokinetic models for infinitely long capillaries, and those used for analysis of ion transport and rejection through membrane pores. Some of the key observations are: (i) The electrokinetic models for transport through infinitely long capillaries are capable of predicting the steady state streaming potentials across a finite length

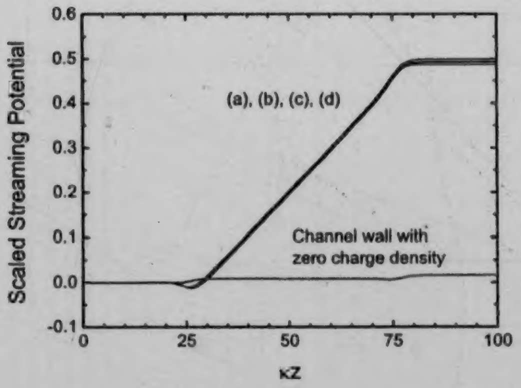

Figure 2.10: Variation of streaming potential with different surface charges on the inlet and outlet faces and the walls of the capillary. Considering the geometry of Fig. 2.2, the scaled charge densities on the boundaries CD (front face), DE (capillary wall), and EF (back face) were varied independently between zero and $\bar{\sigma}_w = 2.0\sinh(0.5\bar{\psi}_w)$, where $\bar{\psi}_w = -1$. Case (a): both front and rear faces with zero charge density. Case (b): back face with zero. Case (c): Front face with zero. Case (d): all faces equally charged. In (a) to (d), the capillary wall was always charged. For comparison, the simulation with capillary wall charge density set to zero, is also shown. In this last case, the front and back faces are charged.

capillary with remarkable accuracy. However, one should note that such comparisons involve using the conditions prevailing at the mid-section of the finite length capillary, where the flow has fully developed. (ii) The transient development of the streaming potential occurs rapidly during the initial stages of the flow development, followed by a gradual relaxation to the steady state. The ion concentrations in the capillary are not perturbed from the initial stationary distributions (governed by the Poisson-Boltzmann equation) during this initial stage. At later stages, however, the ion concentrations develop a sizeable axial gradient. This variation of ion concentrations is not associated with a substantial change in the electrical parameters. (iii) The resulting streaming potential in pressure-driven flow in a narrow capillary (i.e. a channel diameter of 1μm and κa=5) is dominated by the surface charges on the capillary wall, and not strongly affected by charge on the inlet and outlet surfaces

In addition to the above observations, it is demonstrated that once the vastly different time scales of development of the streaming potential and the steady-state ion concentrations are properly resolved, several anomalies between the streaming potential theories for infinite capillaries and membrane transport theories based on the extended Nernst-Planck model are resolved. Notably, the present simulations depict that pressure driven flow through a charged capillary indeed results in rejection of ions if the electrolyte concentration in the exit reservoir is allowed to change.

CHAPTER 3

TRANSIENT CURRENTS, CAPACITANCE AND ELECTRICAL ANALOGY OF A FINITE LENGTH MICROCHANNEL

3.1 Introduction

So far, discussion has focused on the transient behavior and evolution of streaming potentials, ionic concentrations and electrical fields. In this chapter[1] the material presented in Chapter 2 is extended to consider the ionic fluxes that create the transcapillary potential from a no-flow equilibrium state to its SSSF (steady state - steady flow) equilibrium state that are the focus of this chapter. The objectives of Chapter 2 were to resolve issues encountered in establishing appropriate boundary conditions for the complementary problems of EK transport and membrane filtration, to explore the development of streaming potential through the range of convective and migration time scales, and to establish the relative importance of the channel walls compared to the inlet and outlet faces. Missing in that chapter was any elucidation of the roles of the current flows during the development of the streaming potential, which thereby provides the base objectives of this chapter. By analyzing the components of currents (particularly, convection, migration and net current) in the context of the transport of charge, the ideas of system capacitance and resistance are explored. An electrical analogy is proposed where the main objective of the chapter is fulfilled by providing a simplified model for transient microchannel flow in terms of the nondimensional parameters that capture the characteristics features of the channel geometry, electrostatic interaction, hydrodynamics, and mass transfer [73].

---

[1] Part of this chapter is closely related to the work accepted for publication of "Ali Mansouri, Subir Bhattacharjee, and Larry Kostiuk" in the Journal of Physical Chemistry B, in press, 2007

The approach taken to achieve these objectives is through numerical modeling, and hence this chapter is organized as follows: In Sections 2 and 3, the geometry of interest is described and then modeled through a set of governing equations and boundary and initial conditions. This section also develops the expressions necessary to calculate the currents and other characteristic parameters for the system once the governing equations have been solved. In Section 4, the numerical solution methodology is described, and an extension to the validation of both the numerical model and the methods for computing the currents is provided. In Section 5, the transient results of the governing equations are presented, showing how the net current and its components, as well as the charge distributions, evolve to establish the SSSF streaming potential. Data on the spatial redistribution of free charge highlight the notion of these channels having an electrical capacitance, and a discussion is provided on the appropriateness of an electrical analogy for the system. Section 5 also includes a dimensional analysis of the key physical parameters relating to the geometry, fluid mechanics, electrostatics, and mass transfer data. A parametric study on the evolution of the system was completed in order to create the submodels necessary to use of the electric analogy in a predictive manner. Finally, in Section

6, the key conclusions from the present study are summarized.

3.2 Geometry

Fig. 3.1 shows the prototypical generic geometry of an aqueous electrolyte solution flowing between two reservoirs connected by a straight circular cylindrical microchannel having a radius a and length L. This geometry captures many of the key elements of typical microfluidic or membrane filtration applications, including a finite channel length with entry and exits flows, and having surface charge on the front and back surfaces, as well as the channel surface. This geometry avoids the formulation of artificial boundary conditions at the capillary inlet and outlet, but instead allows for development of the appropriate entrance and exit conditions for the capillary originating from bulk conditions in the reservoir. These bulk conditions were defined sufficiently far away from the capillary entrance or exit to have no influence on the results. This geometry is the same as that presented in Chapter 2 and II, JJ and KK represent three distinct cross sectional areas of reservoirs and microchannel.

3.2.1 Governing Equations, Boundary and Initial Conditions

The fluid mechanics was modeled within the context of the Navier-Stokes (NS) equations. The form of the NS equations, including an electrical body force used here, is given by

$$\rho(\frac{\partial \mathbf{u}}{\partial t} + \mathbf{u} \cdot \nabla \mathbf{u}) = -\nabla p + \mu \nabla^2 \mathbf{u} - \rho_c \nabla \psi \tag{3.1}$$

where ρ is the fluid density, u = (u, v) is the velocity vector with u and v being the radial and axial components, respectively, t is time, p is pressure, μ is the

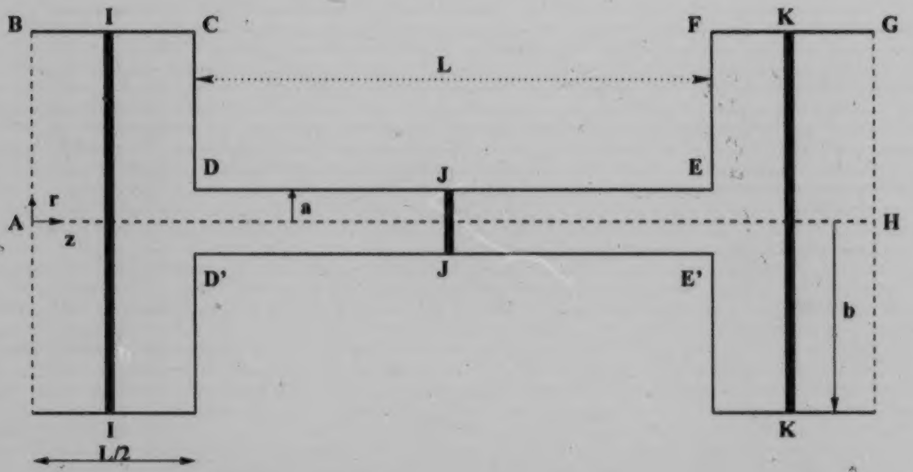

Figure 3.1: Schematic of pressure-driven flow geometry, which includes the microchannel, and inlet and outlet reservoirs. The planes II, JJ, and KK denote locations where the current is integrated over the channel cross section.

viscosity, ψ is the electrical potential, and ρ_c is the free electrical charge density given by

$$\rho_c = \sum \nu_k e n_k,$$

where ν_k is the valence of the k^{th} ionic species, e is the elementary charge, n_k is the ionic number concentration, and K is the number of ionic species. (In this work, K = 2, which later allows data on the positive and negative species to be designated by subscripts p and n, respectively.)

The distribution of charge and the transport of ions were modeled by the

Poisson-Nernst-Planck (PNP) formulation. In the absence of induced time-dependent magnetic fields, the charge density was related to the electrical potential by the Poisson equation

$$\nabla^2\psi = -\frac{\rho_c}{\epsilon}\ , \tag{3.2}$$

where ϵ is the dielectric permittivity of the fluid. The balance of species was described by the Nernst-Planck equation and captures convection, diffusion, and migration, respectively, according to

$$\frac{\partial n_k}{\partial t} = -\nabla \cdot \mathbf{J}_k = -\nabla \cdot (n_k\mathbf{u} - D_k\nabla n_k - \frac{\nu_k e n_k D_k}{k_B T}\nabla\psi)\ , \tag{3.3}$$

where J_k is the ionic flux vector, D_k is the diffusivity, T is the temperature, and k_B is the Boltzmann constant. As we are dealing with dilute solutions, the permittivity and other fluid properties are considered to be uniform and constant in the domain. By adopting the general form of Equations 3.1 - 3.3, no assumptions are made regarding the physical extent of the electric double layers. The boundary conditions for the fluid flow, electrical field, and ionic species that allow this set of governing equations to solve the geometry of interest were presented in Fig. 2.2. The boundary conditions for the fluid mechanics describe a pressure-driven flow through a channel with nonslip walls, and indicate that the channel of interest is sufficiently isolated from any neighboring channels that the boundary at distance b away form the channel axial has no normal component to its flow. The electrical boundaries involved setting a reference potential at the flow inlet, and giving all the surface the same surface charge density to mimic a single dielectric material in contact with an aqueous solution. No provisions were made to account for the second-order effect of surface charge density being altered by potential compositional variations in the system. The electrical boundary at the outflow was made as a far-field condition with no variation in the field. The boundary conditions for the ionic species were based on specifying an identical bulk concentration at the inlet and outlet of the reservoirs, emulating a streaming potential formulation as opposed to a classical membrane filtration situation in which ionic species allow changes from inlet to outlet. The differences in the transcapillary potential between these two situations have been shown to be very small, because perturbations to the concentration field are minor and the distances from the ends of the channel to the computation boundaries are large so that any diffusional effects of the different boundary conditions are small (see Chapter 2).

The transient behavior of the system was tracked from an initially quiescent state until the steady-state-steady-flow conditions were attained. Hence, the initial conditions were established by first solving the steady-state formulation of this problem with no flow. In this case, there is no need for the NS equation, and the time derivative in the Nernst-Planck equation was set to zero. Consequently, the initial conditions for the transient problem included the static electric double layers over all surfaces.

3.3 Current, Net Transported Charge, and Capacitance

Since the objectives of this study are associated with the transient evolution of transporting charged species, expressions for how the various currents are calculated need to be developed. The local current flux, a vector quantity denoted by i, is related to the flux of ionic species by

$$\mathbf{i} = e\sum \nu_i \mathbf{J}_i \tag{3.4}$$

To calculate the stream-wise current, the three terms (convection, migration and diffusion) that contribute to the ionic flux vector are integrated across the circular cross-section perpendicular to the axis of the channel to give

$$\mathbf{i}_{z,conv} = 2\pi e \int_0^R u_r \sum \nu_i n_i r dr \tag{3.5}$$

$$\mathbf{i}_{z,diff} = 2\pi e \int_0^R \sum D_i \nu_i \frac{\partial n_i}{\partial z} r dr \tag{3.6}$$

$$\mathbf{i}_{z,migr} = 2\pi \frac{e^2}{k_B T} \int_0^R \frac{\partial \psi}{\partial z} \sum \nu_i n_i D_i r dr \tag{3.7}$$

where $i_{z,conv}$, $i_{z,diff}$, and $i_{z,migr}$ are the stream-wise convection, diffusion and migration currents, respectively, and R, as the limit of integration is equal to "a" or "b" depending if the integration is performed in the channel or in the reservoir, respectively. The migration current is also know as the conduction current. The net stream-wise current is calculated as the sum of these components, such that

$$\mathbf{i}_{z,net} = i_{z,conv} + i_{z,diff} + i_{z,migr} \tag{3.8}$$

When considering the transient current in a flow of a dielectric medium it is important to remember that the conservation of current is not expressed by the divergence of current flux being zero. Instead, by combining the Poisson and free charge equations to eliminate the free electric charge density, the Poisson equation becomes

$$\nabla^2\Psi = -\frac{e\sum \nu_i n_i}{\epsilon} \tag{3.9}$$

Further, defining the electric field as $E = -\nabla\Psi$, and taking the time derivative of Eq. (3.9) to convert the expression to current results in the conserved form of current flux as

$$\nabla \cdot \langle \frac{\partial(\epsilon E)}{\partial t} + \mathbf{i} \rangle = 0 \ , \tag{3.10}$$

where the first term is referred to as the displacement current. Once the electric field stabilizes at steady-state, the divergence of the current flux becomes zero.

The net charge transported across a circular cross-section perpendicular to the axis of the channel, $Q_z(t)$, is calculated from the time integration of the net current and is given by

$$Q_z(t) = \int_0^t i_{z,net}\, dt, \tag{3.11}$$

For this work, the electrical capacitance (C) of the channel was analogously defined with that of a parallel plate capacitor as the ratio of the incremental displacement of charge through the channel to the resulting incremental change in potential difference, such that

$$C(t) = \frac{\partial Q_z(t)}{\partial \Psi(t)}, \tag{3.12}$$

The time dependence of the capacitance has been made explicit in Eq. (3.12) because the evaluation of its temporal characteristics is one of the objectives of this study. By using the transcapillary potential difference, the system capacitance was then characterized as

$$C(t) = \frac{\partial Q_z(t)}{\partial(\Psi_{GH}(t) - \Psi_{AB})} = \frac{\partial Q_z(t)}{\partial \Psi_{GH}(t)}, \tag{3.13}$$

where Ψ_{GH} is the potential at the GH-boundary (see Figure 3.1), while the potential at the AB-boundary was specified to be zero at that surface.

Lastly, a property complementary of the system capacitance that can be evaluated is the system conduction resistance (R). This characteristic system resistance is evaluated here by

$$R(t) = \frac{\partial \Psi_{GH}(t)}{i_{z,migr}(t)}, \tag{3.14}$$

3.4 Numerical Methodology and Validation

3.4.1 Methodology

The details of the numerical method for solving the governing equations were provided in Chapter 2, and are only summarized here. The governing equations, 3.1 - 3.3, were made nondimensional according to Table 2.1, and were solved by the commercial finite element code Femlab (COMSOL, Inc.). All the governing equations were solved together in a time dependent mode for incremental time steps until a steady-state result was achieved. The finite element calculations were performed using quadratic triangular elements. The mesh was refined near the channel walls and centerline to accurately capture regions of large potential gradients and the large impact on convective flux from subtle changes in the axial electric field, respectively. The independence of the results to mesh refinement was studied and necessitated meshes containing up to 10000 elements.

3.4.2 Validation

Evidence of the validity of the numerical results of this formulation was provided in Chapter 2 in a two step process. First, the potential distribution of the transient solution at large times was favorably compared to an independent steady-state solution that had no time-dependent terms. Second, the steady-state numerical model was compared to existing analytical results for streaming potential flow in an infinitely long capillary with low surface potentials on the walls. The analytical results were obtained for the transport of a symmetric electrolyte in a straight circular cylindrical capillary of infinite length and comparisons were made on the basis of the axial electric field and velocity profile at the mid-length of the channel. The quality of the comparisons provided considerable confidence in the subsequently presented results.

With the emphasis of this chapter being on the transport of charged species, further validation was required to provide assurance that the current was being captured accurately. The only time that the transport of charge is known with certainty is at steady state, and, at that time, the transport of negative and positive charges should be a constant everywhere in the channel and reservoirs. To evaluate the model in this respect, the physical parameters presented in Chapter 2 were employed, and the net current transport of the positive and negative ions through sections II, DD, JJ, EE, and KK were independently calculated. The mesh at these cross-sections was refined relative the bulk domain until the integrated results were made insensitive with respect to the mesh. Numerically the current was calculated by using second-order boundary integrations at the mentioned cross sections. The average net current and the range calculated at the different sections were $1.047 \times 10^{-12} \pm 5 \times 10^{-15}$ C/s and $1.045 \times 10^{-12} \pm 2 \times 10^{-15}$C/s for the positive and negative ions, respectively. These results validate the ability of the numerical method to converge to the steady state limit of conservation of species and current, and the idea that the integration across the flow area was numerical accurate in evaluating these quantities.

3.5 Results and Discussions

Detailed numerical results are first presented for a specific base case of geometry, pressure difference across the channel, and surface charge density in order to elucidate the transient transport occurring in the channel. On the basis of those results, an electrical analogy for the channel is presented that involves a current source, a resistor, and a capacitor, all in parallel. Subsequently, the focus of the results shift to tracking stream-wise currents at the mid-length of the channel and calculating the characteristic capacitance and resistance of the system, for a parameter study over a range of κa, L/a , Reynolds number (Re), Schmidt numbers (Sc), and surface potential (ζ). Finally, on the basis of a dimensionless analysis for the capacitance, convection current, and resistance

Parameter	Value	$i_{z,conv}$, pA	C, fF	R, Mohms
L/a = 10	L = 5×10^{-6} m	0.51	0.32	24 MΩ
L/a = 20	L = 1×10^{-6} m	0.51	0.16	48 MΩ
L/a = 100	L = 5×10^{-5}	0.51	0.032	240 MΩ
Re = 0.001	$\frac{\partial p}{\partial z} = 10^7$ Pa/m	0.51	≈ 0.32	24 MΩ
Re = 0.0005	$\frac{\partial p}{\partial z} = 5 \times 10^6$ Pa/m	0.256	≈ 0.32	24 MΩ
Re = 0.0001	$\frac{\partial p}{\partial z} = 10^6$ Pa/m	0.051	≈ 0.32	24 MΩ
$\kappa a = 5$	$n_\infty = 10^{-5}$ M	0.51	≈ 0.32	24 MΩ
$\kappa a = 7$	$n_\infty = 2 \times 10^{-5}$ M	0.4	≈ 0.32	12.5 MΩ
$\kappa a = 10$	$n_\infty = 4 \times 10^{-5}$ M	0.286	≈ 0.32	6.4 MΩ
$\frac{-e\zeta}{kT} = 1$	$\sigma = -0.00019 \frac{\mu C}{cm^2}$	0.51	≈ 0.32	24 MΩ
$\frac{-e\zeta}{kT} = 1.5$	$\sigma = -0.00028 \frac{\mu C}{cm^2}$	0.67	≈ 0.32	21.1 MΩ
$\frac{-e\zeta}{kT} = 2$	$\sigma = -0.00038 \frac{\mu C}{cm^2}$	0.85	≈ 0.32	18 MΩ
Sc = 100	$D = 10^{-8}$	0.51	≈ 0.32	2.4 MΩ
Sc = 1000	$D = 10^{-9}$	0.51	≈ 0.32	24 MΩ
Sc = 10000	$D = 10^{-10}$	0.51	≈ 0.32	240 MΩ

Table 3.1: Parametric study on five non-dimensional groups; L/a, Re, κa, $\frac{-e\zeta}{kT}$ and Sc for a single finite length microchannel. In all simulations a; microchannel radius kept constant (0.5 μm) and the rest of information extracted from numerical code.

predictive submodels associated with the electrical analogy are provided to allow the results from the parametric study to be generalized.

3.5.1 Behavior of Transient Currents; convection, migration and net currents

In this section, the numerical results of the base case (similar to the case presented in Chapter 2) are presented. The transient development of the transcapillary potential to a streaming potential and its relationship to the transport mechanisms will be elucidated by carefully observing the initial time steps of each transport components, namely, convection, migration, and diffusion currents. Simulations with small time-step increments were used to capture the initial stages of each of these current components immediately after establishing the pressure gradient. Fig. 3.2 shows the evolution of the convection current (Equation 3.2), the migration current (Equation 3.4), and the net current (Equation 3.1). Also shown in these panels are the currents decomposed into that transported by the positive and negative ions (denoted by np and nn, respectively). The diffusion current is not shown because it is always three orders of magnitude less than the other components.

By its nature, the convection current (Fig. 3.2a) is strongly coupled to the hydrodynamic time scale (Fig. 3.2f), and it reaches near the SSSF in a tenth of a microsecond. Owing to the negatively charged walls of the microchannel, more counter-ions are transported along the channel compared to co-ions. Consequently, the free electrical charge density field becomes distorted relative to the no flow situation, as depicted in Fig. 3.3. Fig. 3.3 shows a time sequence of the free electrical charge density at various times that has been subtracted from the corresponding charge density with no-flow, defined here as the flow field induced reorganization of free charge (polarization) and given by $(n_p - n_n)_t - (n_p - n_n)_0$. The key feature in Fig. 3.3 is that the entire inlet and outlet of the channel becomes covered by fluid with free charge densities that are respectively diminished and elevated compared to the no flow condition. Hence, any path along which the Poisson equation is integrated between the reservoirs results in the creation of the transcapillary potential difference (Fig. 3.2d) and this potential is initiated at the same time scale as hydrodynamics.

While the convection of a mixture with an imbalance of positive and negative ions establishes the transcapillary potentials, these same ions, under the influence of this newly created electric field, start to migrate. Fig. 3.2b shows that this migration does not establish itself to be significant until an order of magnitude greater in time than the hydrodynamics. With the migration of positive ions moving upstream being greater than the negative ions moving with the flow, an electroviscous effect is observed through the modest flow retardation that is seen in Fig. 3.2f. Returning to Fig. 3.2b, the migration current continues to evolve over yet another order of magnitude or more, until SSSF equilibrium is reached and there is no net current occurring (Fig 3.2c). The magnitude of the migration current and the transcapillary potential evolve synchronously, as shown in Fig. 3.2e.

In summary, the net current and transcapillary potential respond on a hydrodynamic time scale, and then they reach their SSSF values (i.e., no net current and the streaming potential) on a diffusion/migration time scale. Just as the transcapillary potential was initiated by a net current flow, it stops changing when the net current goes to zero. (Emphasis is given here that the transcapillary potential is only referred to as the streaming potential when under the steady state steady flow condition.)

Attention now switches to exploring the temporal resistive and capacitive characteristics of this microchannel. Fig. 3.4 depicts the time evolution of these characteristics. The time evolution of the channel resistance shown in Fig. 3.4a is determined from the transient transcapillary potential (Fig. 3.2d) divided by the corresponding migration current (Fig. 3.2b) according to Eq. (3.14). The corresponding capacitance of the channel (Fig. 3.4b) is obtained by dividing the time integral of the net current (Fig. 3.2c) by the corresponding transcapillary potential employing Eq. (3.13). Finally, in anticipation of a discussion on an electrical analogy for a microchannel, Fig. 3.4c shows the R-C time constant as a function of time. Because of numerical uncertainties, particularly to the denominators of Equations 3.13 and 3.14, at very early times, the temporal behavior of these quantities was chosen to be plotted from 0.1 μs.

The capacitance and resistive characteristics of this channel are not constants at all times. At very early stages in the flow development, the capacitance is

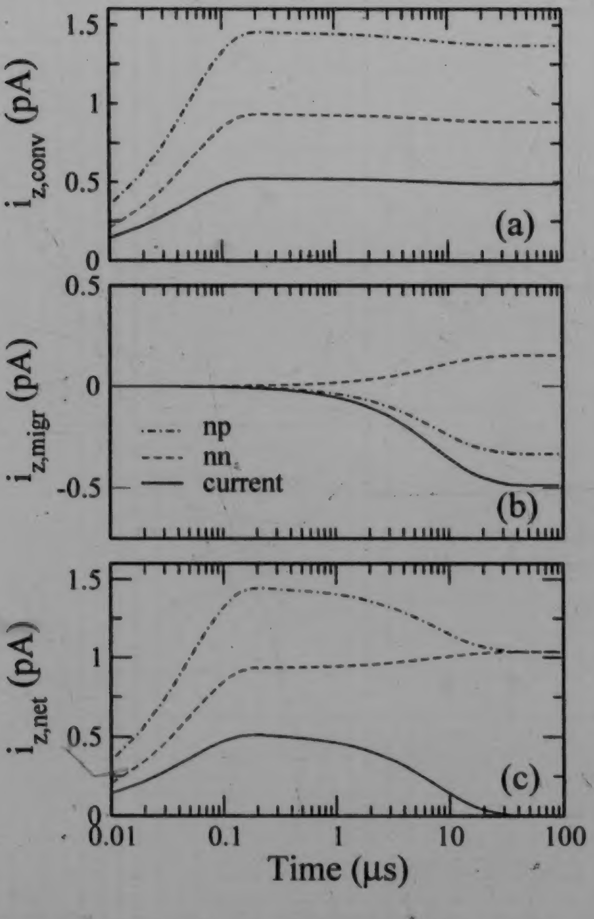

Figure 3.2: Transient numerical results for geometry and flow conditions for the base case. Panels (a)-(c) show the transient convective, migration and net currents calculated at the mid-length of the channel, and also include the transport of the positive and negative ions at the same location

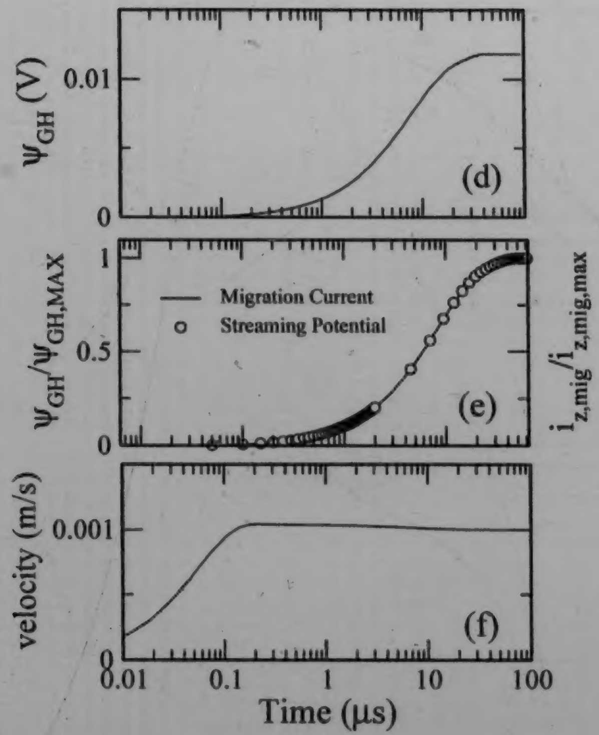

Figure 3.2: Continued, Transient numerical results for geometry and flow conditions for the base case. Panel (d) shows the transient transcapillary potential with the inlet reservoir defined as ground. Panel (e) compares the normalized rise in transcapillary potential to the rise in migration current at the channel mid-length. Panel (f) shows the transient development of the centerline hydrodynamic velocity at the mid-length of the channel

relatively large, while the resistance is relatively low, compared to later times. Defining the total time to reach SSSF as when the transcapillary potential reaches 99% of the streaming potential, the capacitance and resistance were within 10% of their SSSF values within 0.82% and 0.94% of the total time to reach SSSF, respectively. In regards to the RC time scale, it reached 90% of its final value within 0.18% of the total time to reach SSSF. Hence, even though the capacitive and resistive characteristics of a microchannel system are not ideal capacitors and resistors, a model based on these electrical elements may prove to be a useful tool in describing transient situations in all but the earliest times.

3.5.2 Equivalent Electrical Analogy

On the basis of evidence in Fig. 3.4, an electrical analogy for the flow through a microchannel is presented in Figure 3.5. A key element of the model was established by the strong correlation between the volumetric flow rate and the convection current over all times between the equilibriums of no-flow to SSSF. In the electrical analogy this is represented by a current source (S) equal to the convection current. Since no current leaves the system, the transported charge ($Q_z(t)$) accumulates near the ends of the channel and a responding transcapillary potential develops that is a function of the system capacitance (C), which relates the transported charge to a changing potential. The developing transcapillary potential creates a conduction current of a proportional magnitude, which is then captured by the resistive element (R). This resistive element represents the summation of bulk and surface conductance of the working electrolyte. Unlike the convection current, which responded on the hydrodynamics time scale, the capacitance and resistance of the microchannel system develop slower. Consequently, the constitutive properties of the resistor and capacitor were shown not to be constant for all times, but the time in which they are not

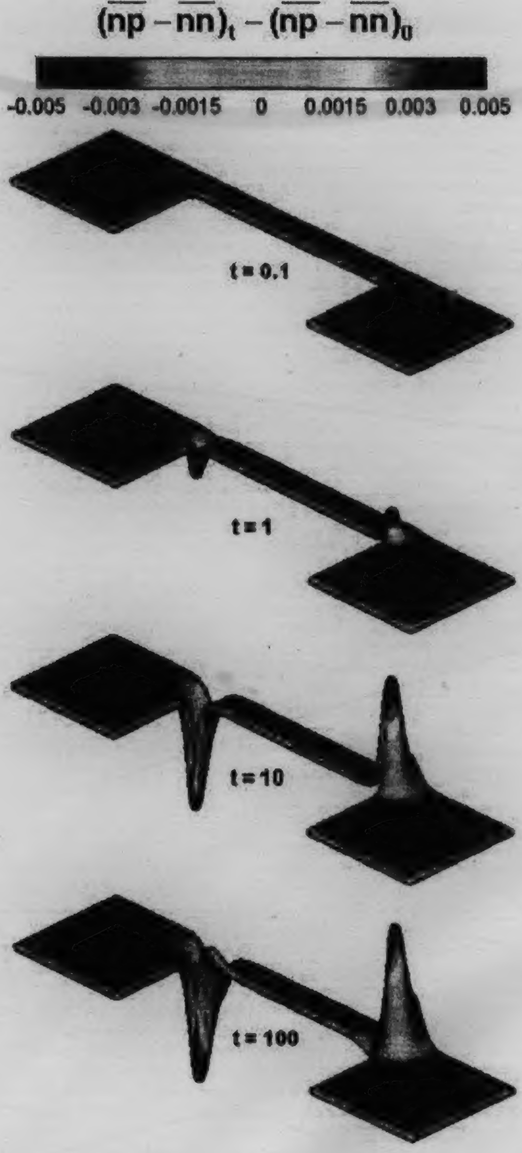

Figure 3.3: Time sequences (0.1, 1, 10 and 100 μs) of spatial variation in free charge density relative to the no flow (continued on next page).

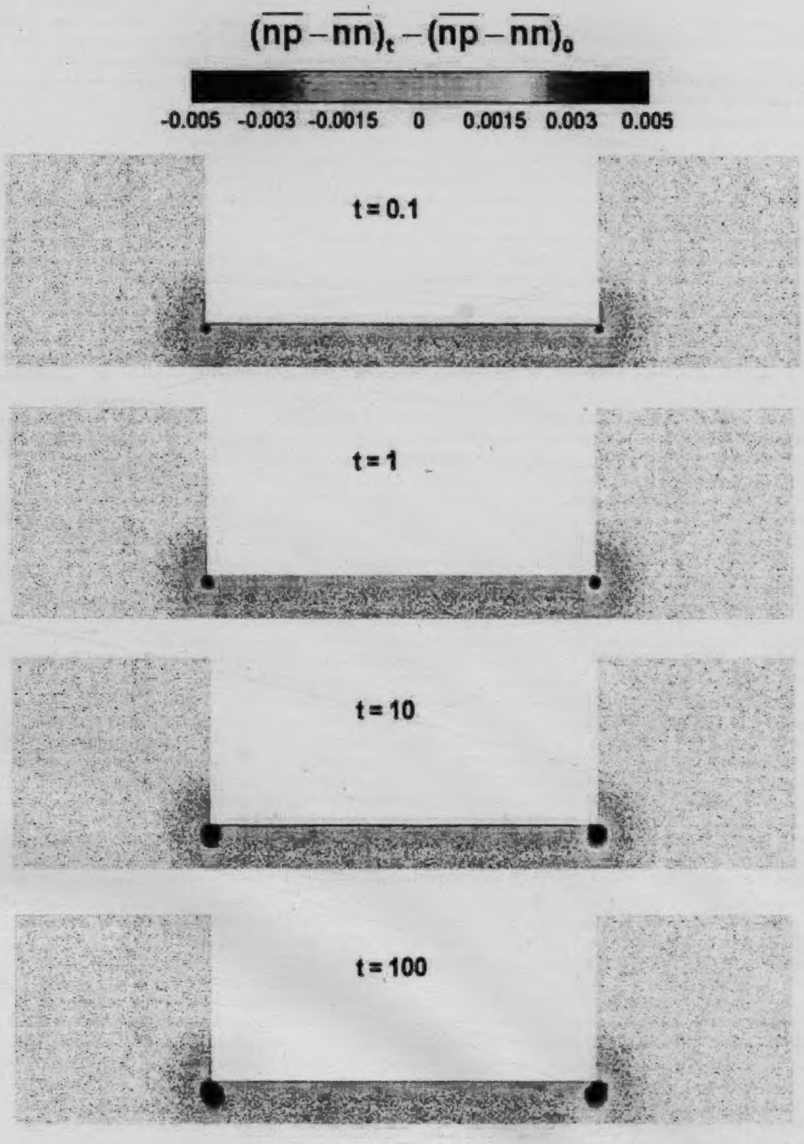

Figure 3.3: Continued: 2D representation of time sequences (0.1, 1, 10 and 100 μs) of spatial variation in free charge density relative to the no flow

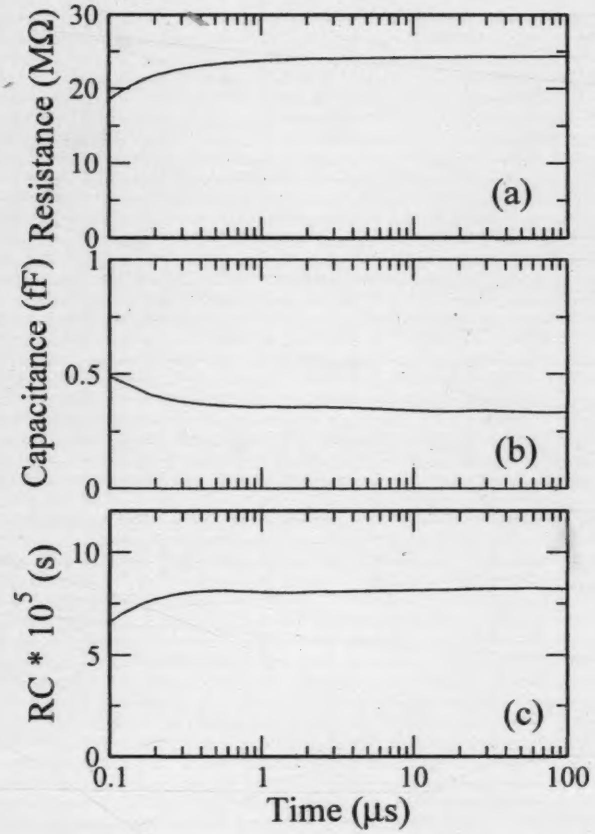

Figure 3.4: Temporal variation in (a) the characteristic resistance, (b) the characteristic capacitance, (c), and R-C characteristics of the microchannel system.

constant appears to be small compared to the overall time to come to SSSF conditions.

The importance of these properties not being constants needs to be explored to validate the quality of an electrical analogy when using time independent values for convection current, capacitance, and resistance. Fig. 3.6 shows a comparison of the evolution of the transcapillary potential differences from the full numerical simulation (base case) and the electrical analogy where the values for the current source, capacitance, and resistance have been specified to be 0.51 (pA), 0.32 (fF), and 24 (MΩ), respectively.

It is clear from Fig. 3.6 that a pressure-driven flow inside a charged microchannel and a current source connected in parallel to a resistive-capacitive circuit both generate similar transcapillary potentials despite their different governing equations. Moreover, it can be concluded that the transient decay of current in the capacitor and that of the net current in the microchannel are similar and governed by a similar time constant. The maximum error in transcapillary potential relative to full scale (i.e., the stream potential) between the full numerical model and the electrical analogy was 5.7% and 1.3% in transient and steady sates, respectively. The usefulness of this kind of an electrical analogy hinges on the ability to have predictive sub-models for the current source, capacitance and resistance. Data for those sub-models were developed through a parametric study described in the following section.

3.5.3 Parametric Study of Net Transient Current

In the previous section the case was made that complexities associated with solving the coupled set of transient Navier-Stokes and Poisson-Nernst-Planck equations could be effectively reduced to solving simple electrical analogy. The success of this analogy was validated for only one set of physical parameters.

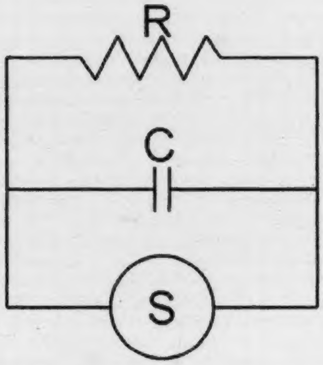

Figure 3.5: Electrical analogy of a microchannel. The current source, S, is analogous to the convection current, the capacitor (C) allows for the accumulation of charge and development of a potential difference, and the resistor (R) makes the migration current respond synchronously to the potential difference.

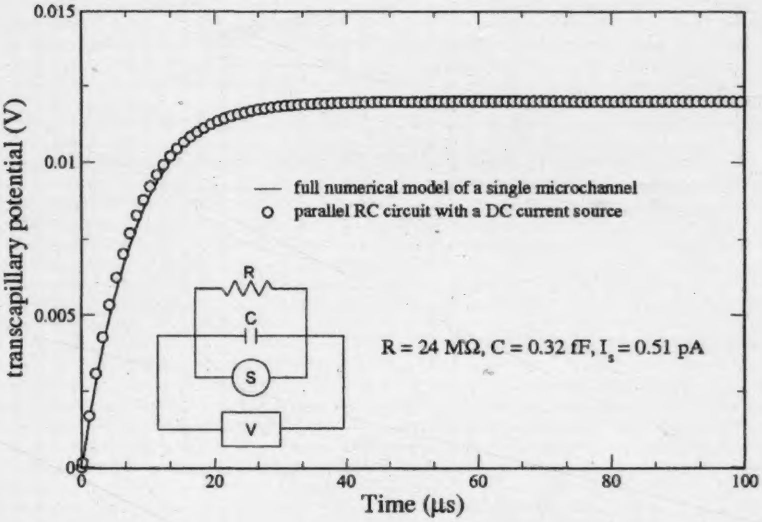

Figure 3.6: Comparison of Navier-Stokes, Poisson-Nernst-Planck model for transient microchannel flow with an electrical analogy based on a current source, capacitor and resistor in terms of the transcapillary potential, which is represented by a voltmeter; V, in the analogy.

In this section, a parametric space associated with the independent variation of the geometry (i.e., L/a), the fluid mechanics (i.e., Re), the electrostatics (i.e., κa and ζ), and mass transfer (i.e., Sc) around this validated case is explored numerically. The range of these variables explored was L/a = 10, 20, and 100 by changing L, Re = 0.0001, 0.0005, and 0.001 by changing the upstream reservoir pressure to change the mean velocity, κa = 5, 7, and 10 by changing the electrolyte concentration, nondimensional ζ; $\frac{-e\zeta}{kT}$ = -1, -1.5 and -2 by changing the surface charge density to create situations that are both inside and outside the domain of linear theory, and Sc = 100, 1000, and 10000 by changing diffusivity. Figs. 3.7 to 3.10 show the results of this parametric study in terms of temporal net current at the mid-channel and transcapillary potential. (The figure for varying Sc has not been presented because the orders of magnitude variations introduced in the time scale.) The values of the SSSF convection currents, capacitances, and resistances are compiled in Table 3.1. A review of Table 3.1 shows various dependencies worth noting before trying to model these results. Only the convention current was not affected by the channel length, as long as the flow rate was maintained, while the capacitance was only affected by the channel length. The resistance was affected by everything but the flow rate.

3.5.4 Sub-Models for Capacitance, Convection Current and Resistance

In order to use the electrical analogy, sub-models are required for the capacitor (C), the current source ($i_{z,conv}$) and the resistor (R). Given the number of independent variables that could potentially affect the magnitudes of these components, a dimensional analysis was performed. The list of independent physical variables considered included geometry (a, and L), hydrodynamics (u,

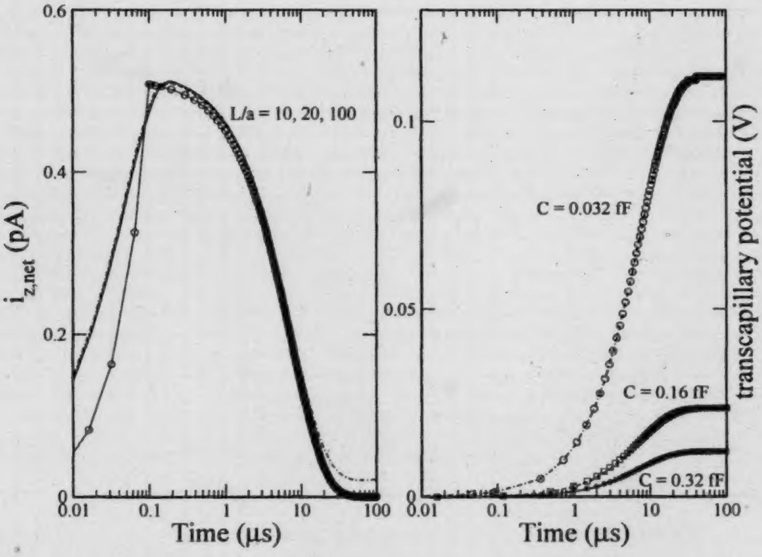

Figure 3.7: Transient response of net current at the mid-length of the channel and transcapillary potential for the systematic variation in the parameter L/a , which was altered through varying the channel length. The lines without symbols are the full numerical simulation results, while symbols connected by lines are the results of electrical analogy model. The capacitances shown are a calculated quantity.

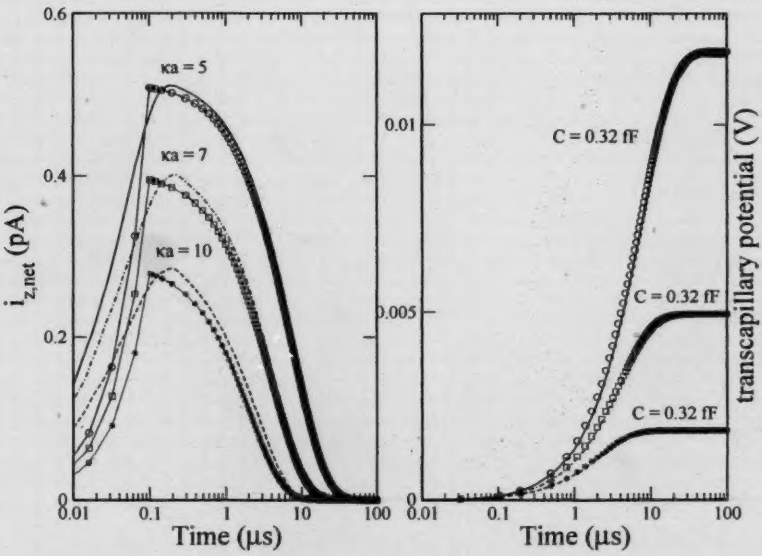

Figure 3.8: Transient response of net current at the mid-length of the channel and transcapillary potential for the systematic variation in the parameter κa, which was altered through varying the Debye length. The lines without symbols are the full numerical simulation results, while symbols connected by lines are the results of electrical analogy model. The capacitances shown are a calculated quantity independent of κa.

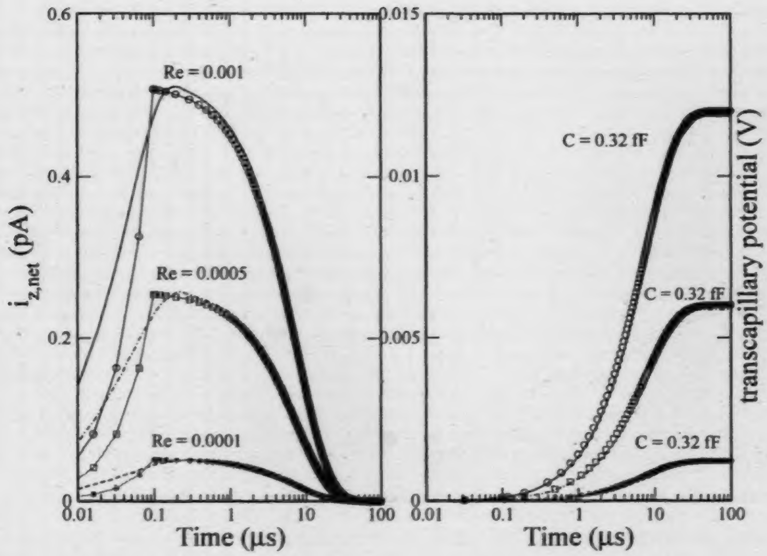

Figure 3.9: Transient response of net current at the mid-length of the channel and transcapillary potential for the systematic variation in Re , which was altered through varying the pressure difference across the channel. The lines without symbols are the full numerical simulation results, while symbols connected by lines are the results of electrical analogy model. The capacitances shown are a calculated quantity independent of Re.

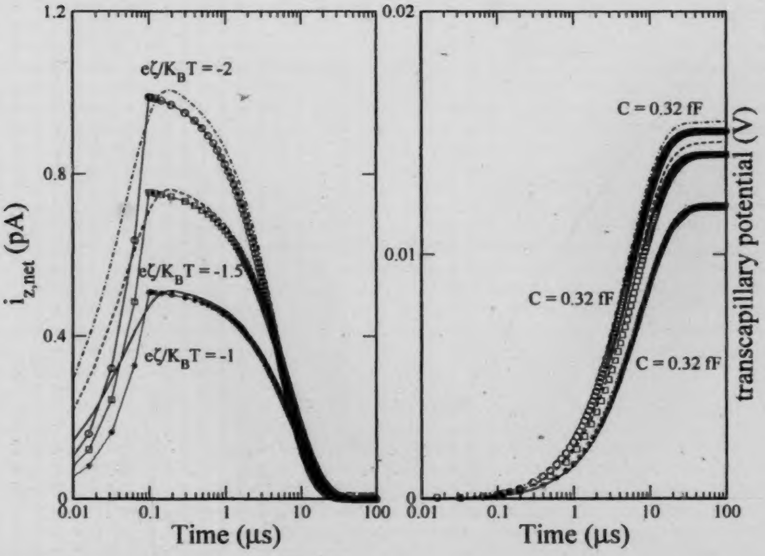

Figure 3.10: Transient response of net current at the mid-length of the channel and transcapillary potential for the systematic variation in the surface potential parameter, which was altered through varying the surface charge density. The lines without symbols are the full numerical simulation results, while symbols connected by lines are the results of electrical analogy model. The capacitances shown are a calculated quantity independent of the surface potential parameter.

ρ, and μ), electrostatics (ζ, κa and ϵ) where κ is the Debye length and already includes the e, k_B, T and n_∞, ζ is the surface potential and ϵ is the permittivity (ϵ = permittivity of space relative permittivity of dielectric material), and, finally mass transfer is dominated by diffusion, D. According to Buckingham's π theorem [74], variables can be grouped non-dimensionally by considering the mass, length, time, and charge in the context of the physics of interest, such for the case of capacitance,

$$\theta(C, a, L, u, \rho, \mu, \zeta, \kappa, \epsilon, D) = \theta(L/a, \kappa a, Re, Sc, \frac{\zeta\sqrt{\epsilon}}{au\sqrt{\rho}}, \frac{C}{\epsilon a}) \tag{3.15}$$

where Sc is the Schmidt number that relates the hydrodynamics to the mass transfer. Having both the Reynolds number (Re) and Sc means that the Peclet Number is effectively captured. It is interesting to note that the last term, *i.e.* $\frac{C}{\epsilon a}$ can be interpreted as non-dimensional capacitance of a parallel plate capacitor; $\frac{CL_c}{\epsilon A}$ in which A is either the surface area of the capacitor plates or cross-section of the microchannel, and L_c is the distance between physical locations of charges. Using the data presented in Table 3.1 and a least squared multivariate fit, the functional dependency between the various non-dimensional groups was found to be

$$\frac{CL}{\epsilon A} = 10.10(L/a)^{-0.002}(\kappa a)^{0.095}(Re)^{-0.019}(Sc)^{-0.140}(\frac{\zeta\sqrt{\epsilon}}{au\sqrt{\rho}})^{-0.134}, \tag{3.16}$$

$$\frac{CL}{\epsilon A} \approx Constant, \tag{3.17}$$

where the constant is on the order of 3. It can be inferred from Eq. (3.16) that "A" and "L" are the only parameters that alter the capacitance of a microchannel. Hydrodynamics can be safely ignored as long as Re < 1, Electrostatics plays a very small role since permittivity is a very weak function of concentration and zeta potential and mass transfer have essentially negligible effect on capacitance.

Similar approaches can be implemented for convection current. Physical parameters and non-dimensional groups for $i_{z,conv}$ are summarized below:

$$\theta(i_{z,conv}, a, L, u, \rho, \mu, \zeta, \kappa, \epsilon, D) = \theta(L/a, \kappa a, Re, Sc, \frac{\zeta\sqrt{\epsilon}}{au\sqrt{\rho}}, \frac{i_{z,conv}}{au^2\sqrt{\rho\epsilon}}) \quad (3.18)$$

employing the data presented in Table 3.1 yields

$$\frac{i_{z,conv}}{au^2\sqrt{\rho\epsilon}} = 0.410(L/a)^{-0.014}(\kappa a)^{-1.840}(Re)^{-1.007}(Sc)^{0.050}(\frac{\zeta\sqrt{\epsilon}}{au\sqrt{\rho}})^{0.980}, \quad (3.19)$$

$$\frac{i_{z,conv}}{au^2\sqrt{\rho\epsilon}} \approx \frac{0.7}{Re(\kappa a)^2}(\frac{\zeta\sqrt{\epsilon}}{au\sqrt{\rho}}), \quad (3.20)$$

where the second "approximate" expression adopts the nearest integer or root values with respect to the limited data sets used in the correlations. Since the manipulation of non-dimensional groups is permitted, convection current can be transfer to its well-known form; Smoluchoswki equation and given here

$$i_{z,conv} = au^2\sqrt{\rho\epsilon} \times \frac{\zeta\sqrt{\epsilon}}{au\sqrt{\rho}} \times \frac{2\rho ua}{\mu} \times \frac{3.14a}{4L} = \frac{\rho u^2\zeta\epsilon A}{2L\mu} = \frac{\epsilon\zeta}{\mu}\frac{\triangle pA}{L}, \quad (3.21)$$

Rewriting Eq.3.21 yields

$$i_{z,conv} = \theta(\frac{\epsilon\zeta}{\mu}\frac{\triangle pA}{L}, \kappa a) = \frac{\epsilon\zeta}{\mu}\frac{\triangle pA}{L}\theta(\kappa a) = \frac{\epsilon\zeta}{\mu}\frac{\triangle pA}{L}f(\kappa a), f(\kappa a) = 1 if \kappa a \gg 1, \tag{3.22}$$

Resistance of a microchannel has a more physical accessible interpretation and is only a function of electrolyte conductivity and geometry. Hence, the model proposed here does not require a model based on a multivariant fit, and can be express as

$$R = \frac{L}{A\sigma} \tag{3.23}$$

where L and A are the microchannel length and cross sectional area and σ is the electrolyte conductivity. We assume resistance of the inlet and outlet reservoirs are negligible compare to resistance of the microchannel. The resistance of the microchannel obtained from equation 3.14 and equation 3.23 compared to the base case and excellent agreement observed (2% error). Therefore equation 3.23 was considered for the purpose of this study. Using the models presented in Equations 3.17, 3.22 and 3.23, the results of the electrical analogy model (shown as data points) are compared to the full numerical simulation (shown as lines) in Figs. 3.7 to 3.10 in terms of the transient net current and the transcapillary potential. Based on these figures, the agreement between these two models in terms of the transcapillary potential difference was generally very good and at any time was within 2% (full-scale) of each other. The exception being the case of high surface charge density (i.e., $\frac{-e\zeta}{k_bT} > 1$), which requires further investigation. In terms of net current, the two models were generally in very good agreement, except, in particular, for the very initial times of the transient flow. For the range of conditions examined, the major differences in net current were restricted to the first 100 nanoseconds of initiating the flow, but this did not strongly impact the development of the transcapillary potential difference.

3.6 Conclusions

In this study, numerical simulations based on a Navier-Stokes-Poisson-Nernst-Planck model were used to elucidate the transient transport of charged species through a finite length cylindrical microchannel. The convection, migration, and net currents were of particular interest in how they contribute to the evolution of the transcapillary potential from no-flow equilibrium with no potential difference to the steady-state-steady-flow streaming potential. Observations of the unsteady characteristic electrical resistance (associated with the migration current) and capacitance (associated with the change in potential with respect to net charge transported) as well as the streaming current led to the proposing of an electrical analogy. A parametric study involving a range of geometries, fluid mechanics, electrostatics, and mass transfer situations allowed predictive sub-models to be developed on the basis of a dimensional analysis of the physically relevant properties.

The key conclusions were the followings: (a) The net current, convection current and transcapillary potential initially respond on a hydrodynamic time scale, but they reach their SSSF values on a diffusion/migration time scale. (b) The capacitive and resistive characteristics of a microchannel system were reasonably approximated as ideal capacitors and resistors for all but the earliest times in the development of the flow. (c) On the basis of a previous conclusion, an electrical analogy for a microchannel was proposed to be made up of a current source (to capture the convection current), which was placed in parallel with a capacitor (to capture the accumulation of charge) and a resistor (to capture the migration current) and (d) Sub-models for the current source strength, the capacitance, and the resistance were developed through a parametric study.

CHAPTER 4

INTERPRETATIONS OF STREAMING CURRENT AND POTENTIAL MEASUREMENTS IN A MULTI MICROCHANNEL ARRAY: AN ELECTRICAL ANALOGY APPROACH

4.1 Introduction

Flow[1] of an electrolyte solution through microchannels, membranes, and porous media is strongly affected by the electrical properties (e.g., surface charge density or potential) of the channel wall-fluid interface[2]. In order to measure the relevant electrical properties of solid-liquid interfaces, streaming current and streaming potential (SC/SP) techniques can be employed. SC/SP phenomena in well-defined single micro and nanochannels have been studied comprehensively both experimentally and theoretically [24, 49, 75–78] (also see Chapter 1). SC/SP techniques have been applied to characterize homogeneous and heterogeneous surfaces [23, 24, 77, 79], bio-polymers, [80] and self-assembled monolayers [25] to determine their interfacial properties. Characterization of complex porous media, with unstructured pore geometries, such as membranes and packed beds of granular materials are also routinely conducted employing these techniques [5]. There is, however, a fundamental difference between measurement of SC/SP across a single microchannel as opposed to porous media, the latter often represented as a bundle of capillary microchannels for mathematical modeling. In either case, the measurement of the electric potential or current is performed by placing conducting probes or electrodes into the two bulk electrolyte reservoirs located upstream and downstream of the single microchannel or the porous medium. In this context, two critical problems arise when one attempts to scale up the results obtained for single microchannels to the case of an unstructured porous medium. First, the porous medium will have a significantly lower electrical resistance compared to a single capillary simply because the conducting area of the fluid connecting the two reservoirs is so much larger. Second, the total volumetric fluid flow through a porous medium will be significantly larger than the flow through a single capillary, thus having a greater probability of disturbing the "bulk" solution of the reservoirs. This larger flow rate is particularly important if the reservoirs have insufficient volumes of fluid. The combined effect of these two factors makes the measurement of interfacial properties by SC/SP techniques extremely sensitive to external influences. For instance, the accuracy of such measurements may be affected by the nature of the electrodes, their placement in the reservoirs, the volume of the reservoirs, and the electrical resistance of the external circuit. However, conventional measurements of such processes do not confer much attention to these factors, instead focussing on the unknown pore structures of the porous media to analyze the results [81]. In this study the interactions between electrokinetic flows, electrodes and external circuits are explored with the aid of an electrical analogy. Hence, the objectives of this chapter are twofold: first to develop an electrical analogy of a general electrokinetic flow through an array of microchannels that is coupled with an external circuit that can mimic and explain physical phenomena at electrodes and nature of external electrical devices. Second, to conduct a series of SC/SP experiments in a multi microchannel array that potentially eliminates the complexities associated with working with porous media.

---

[1] The focus of this thesis is now moving to experimental studies. Interpretation of the data collected will rely upon the models and analogies developed in the previous chapters.

[2] Part of this chapter is closely related to a manuscript under preparation by "Ali Mansouri, Subir Bhattacharjee, and Larry Kostiuk" and to be submitted in the Journal of Colloid and Interface Science, 2007

In this study a specially designed glass microchannel array consisting of 3,437,500 circular and parallel microchannels is employed for SP/SC measurements. These experiments were designed in order to explore the consequence of changing the electrolyte, the placement and material of electrodes. Experimental observations are discussed and interpreted by aid of the electrical analogy.

4.2 Electrical Analogy of a Multi Microchannel Array

In order to create a robust electrical analogy for comparison with experimental results to be presented later, the geometry considered involves an array of parallel finite length channels that separate two semi-infinite reservoirs. The working fluid was modeled as an electrically neutral bulk solvent with a multitude of ionic species as solutes. The properties of the substrate material and fluid are such that in a no-flow state, an electrical double layer develops at their interface. The characteristic cross-stream dimension of the channel falls into the regime that a trans-capillary streaming potential would develop under pressure driven flow. The nature of the flow through the channels being considered was general and could be either transient or steady. Lastly, modeled electrodes were placed in the two reservoirs in order to simulate typical experimental data collection systems for measuring either the electrical potential difference across the electrodes or the current flow through an external circuit. The electrical analogy of a single microchannel connecting the reservoirs has been developed and analyzed (see Chapter 3). Here the model is expanded and adapted to consider an array of parallel microchannels.

4.2.1 Current Source: A Parallel Network of Microchannels

As evidenced from Chapter 3, the proposed electrical analogy model for a single microchannel was centered on the notion that the flow of the charged solutes could be seen as a current source. If the flow were from left to right, the flux of positively charged solutes would be current in that direction, while the transport of negatively charged solutes would be current in the opposite direction. For a single microchannel, the streamwise convection current associated with flow (I_{conv}) is the integral over the cross-sectional area (A) of the channel where accounting for variations in local bulk velocity (u), species' molar density (n_i) and the valance of the species (ν_i), such that

$$\mathbf{I_{conv}} = \int \mathbf{u} \sum e\nu_i n_i dA \tag{4.1}$$

For a multi microchannel array consist of N microchannels, the current is additive and the total current yields (see Fig.4.1);

$$\mathbf{I_{array}} = N I_{conv} \tag{4.2}$$

A parallel network of microchannels can be seen as a streaming current device. The energy conversion aspects of such device will be addressed in the

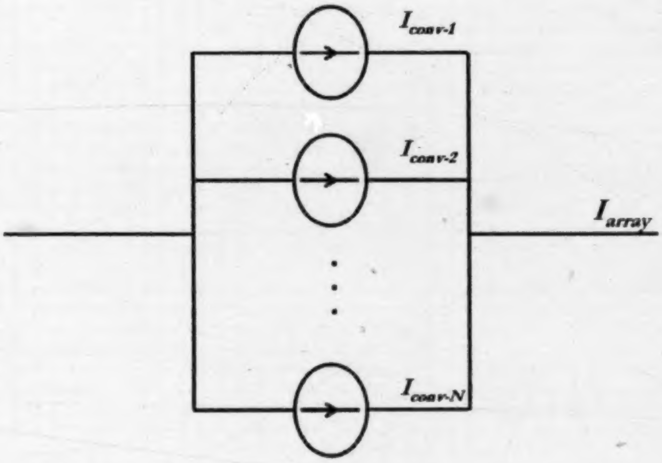

Figure 4.1: Parallel array of individual current sources which comprises a multi microchannel array. Since current is additive, the summation of all currents represents the total current; I_{array}

next chapter.

4.2.2 Capacitance, Resistance and Conduction Current

In the electrical analogy for a single microchannel (Chapter 3), the accumulation of charge between the physical locations was represented by a capacitor that extends across the regions where the relative accumulation or depletion of charge occurs. As a charge density difference develops across a capacitor, an analogous electrical potential difference is created. To capture the migration of current in the direction opposite to the convective current, a simple resistive element was used since the flux is linearly proportional to the electric potential difference. The models for the resistive and capacitive elements were provided in Chapter 3. To expand and employ these models for a multi microchannel array, one needs to multiply the capacitance and conduction current of a single microchannel by N; the number of microchannels and divide the resistance of a single microchannel by N. Therefore at the same time that the capacitance of a multi microchannel array is higher than a single microchannel, a multi microchannel array acquires a lower electrical resistance. These variations in electrical properties of porous medium create several issues in SC measurement as being addressed in the next sections.

4.2.3 Electrodes

The behavior of an electrode - in its simplest form - can be addressed by a resistive-capacitive circuit since electrodes are concerned with flow of current and charge accumulation [82]. In this study a parallel capacitive-resistive circuit considered for representation of electrodes in direct contact with electrolyte. The resistance and capacitance of the electrodes are influenced by several factors, namely the accessible electrode surface area, the chemical nature of the metal surface, the chemical nature of the solvent, and the types of ions present in the electrolyte.

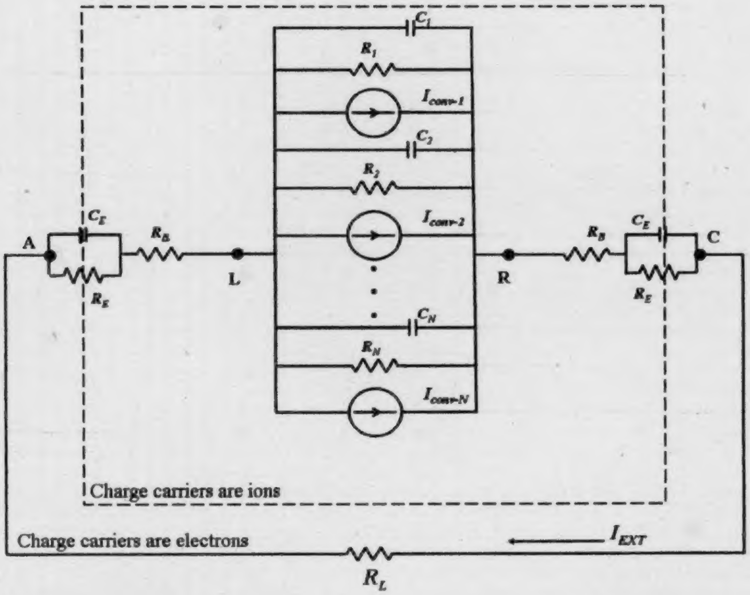
C_1
R_1
I_{conv-1}
C_2
R_2
I_{conv-2}
A
C_E
R_B
L
R_E
R
R_B
C_E
C
R_E
C_N
R_N
I_{conv-N}
Charge carriers are ions
Charge carriers are electrons
I_{EXT}
R_L

Figure 4.2: Schematic of the proposed electrical analogy for a multi microchannel array and electrodes associated with external circuits. The circuit is divided into two parts based on the whether the charge carriers are ions or electrons, and the interface in the surface of the electrodes (points A and C). Re-distribution of ions by flow fields at L and R planes induces the transcapillary-potentials. R_B and R_E are the bulk and electrode electrical resistance, respectively. R_L is the external load and the extremes of this load represents the ideal measurement devices such as a voltmeter ($R_L- > \infty$) or an ammeter ($R_L- > 0$)

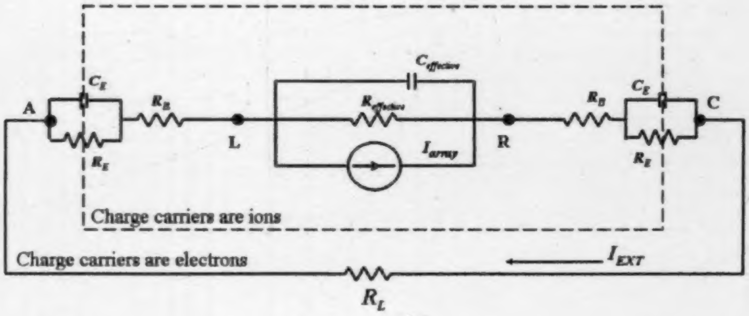
A
C_E
R_E
R_B
L
$C_{effective}$
$R_{effective}$
I_{array}
R
R_B
C_E
C
R_E
Charge carriers are ions
Charge carriers are electrons
I_{EXT}
R_L

Figure 4.3: Simplified schematic of a multi microchannel array and electrodes associated with external circuits. $R_{effective}$ equals to $\frac{R_1}{N}$ where R_1 and N are the electrical resistance of a single microchannel and number of microchannels, respectively. $C_{effective}$ equals to $N \times C_1$ where C_1 represents the capacitance of a single microchannel.

4.2.4 Measuring Electrical Potentials and Currents

The main objective of this analogy is to highlight the issues that arise when trying to measure the expected observable phenomena created by these electrokinetic flows. Typical measurements involve inserting highly conductive electrodes in the reservoirs to measure either the electrical potential difference between the electrodes or the current that passes through an external circuit connecting the electrodes. When there is zero current through the external circuit and the flow has reached SSSF, the measured potential difference is seen as an estimate of the streaming potential. When the potential drop across electrodes approaches zero (shorting the electrodes) the current flowing through the external path is seen as an estimate of the streaming current. Some important conclusions regarding the limits of interpreting standard streaming potential and current measurements can be made if one couples the electric circuit associated with the electrodes and a measurement device (e.g., voltmeter or ammeter) to the analogous circuit that describes the electrokinetic flow. For the purposes of developing this analogy a general resistive load (R_L) was used to externally connect the two electrodes. The extremes of this load are later used to represent the ideal measurement devices such as a voltmeter ($R_L \rightarrow \infty$), an ammeter ($R_L \rightarrow 0$) or a finite resistance between these limits in order to create electrical work in the external circuit. Since the electrodes are located somewhere in the bulk of the reservoirs, they need to be connected with a finite resistive load to where the trans-capillary potential is created. The inclusion of this resistor in the bulk of the reservoir introduces the possibilities of the electrodes being at different electrical potential than that at the ends of the channels. The physical processes invoked in this situation therefore includes the migration of charged species toward or away from the electrode, the potential for charge accumulation around the electrode and electrochemistry at the electrode surface in order to support the flow of electrons through an external circuit when R_L is not infinite. In Chapters 2 and 3 the driving force for the migration of each solute is the electric potential difference between what was established near the end of channel and the electrode. As a result, there is an analogous resistive element associated with the transport of each solute from the end of the channel to the electrode (R_B). Once at the electrode surface each solute must be given the opportunity to undergo electrochemical reactions.

Including these capacitive and resistive elements of the bulk fluid and electrodes, as well as the external resistance into the model for the array of channels, the resultant electrical analogy is shown in Fig. 4.2. The planes "L" and "R" now have physical representations as being the fluid at the effective left and right-hand ends of the channel where the distortion in the various ionic species concentrations occur (i.e., where the accumulation/depletion processes take place). The circuit is also divided into two parts based on the whether the charge carriers are ions or electrons, and the interface is the surface of the electrodes (points A and C represent the anode and cathode of the system). The simplified versions of the electrical analogy are shown in Fig. 4.3 for the general case and Fig. 4.4 for when the external resistance is infinite and the system has reached SSSF flow conditions.

4.3 Experimental Section

4.3.1 The Setup; Multi Microchannel Cell

4.3.1.1 Components

The multi microchannel setup, Fig. 4.5(inset) and Fig. 4.6 was constructed from three independent acrylic sections; an inlet reservoir, a cylinder that sur-

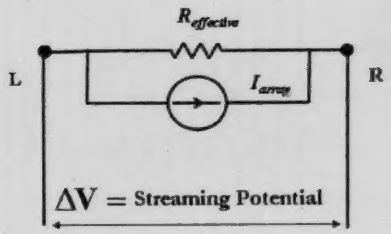
$R_{effective}$
L
R
I_{array}
ΔV = Streaming Potential

Figure 4.4: Schematic of an equivalent electrical analogy in the open circuit mode, namely, streaming potential.

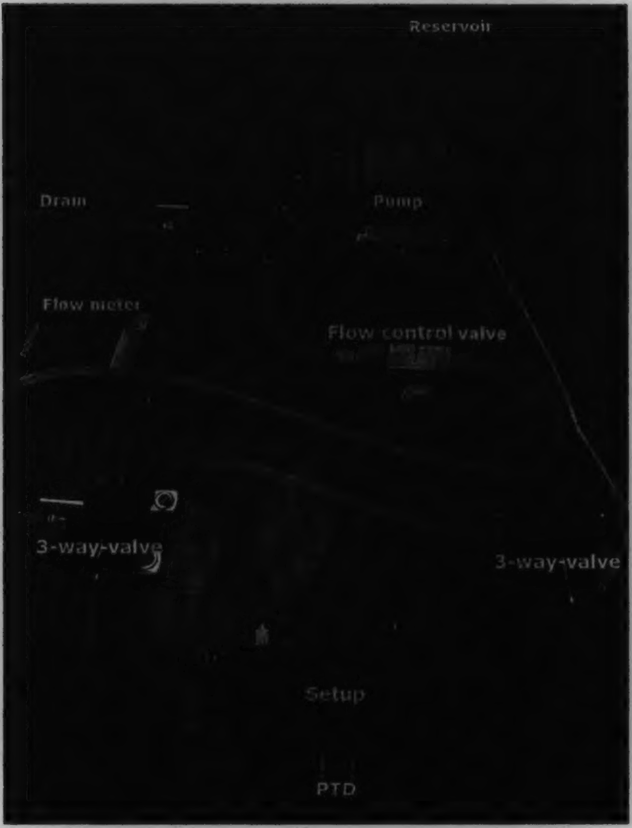
Reservoir
Drain
Pump
Flow meter
Flow control valve
3-way-valve
3-way-valve
Setup
PTD

Figure 4.5: A digital image of the experimental apparatus. Electrolyte is pumped from reservoir, controlled by a flow control valve, passes through the 3-way valves, the setup and the flow meter and finally returns to reservoir. The purpose of the 3-way valves are to enable an alternating flow direction in the setup. The inset shows the setup, constructed from three independent acrylic sections; an inlet reservoir, a cylinder that surrounded and held the microchannel array in place, and an outlet reservoir. The PTD, represents the pressure transducer.

rounded and held the multi microchannel array in place, and an outlet reservoir. Four threaded rods spanning the entire apparatus were used to compress these components together. Teflon O-rings were used to prevent leakage between the sections. The reservoirs on the two ends of the multi microchannel array were 36 mm long. The inlet and outlet reservoirs have sealable 1 mm circular co-axial ports at their ends to allow the introduction of various probes. In the experiments these ports provided access to hold and manipulate the axial position of various electrodes.

4.3.1.2 Electrodes

Two platinized Platinum mesh and two silver mesh electrodes were used in this study. The platinized Pt electrodes were prepared by electrodeposition at 50 mV from 2% chloroplatinic acid in 1 M HCl onto circular (25 mm diameter) pieces of pure platinum gauze (Pt gauze, 45 Mesh woven from 0.198 mm diameter wire, 99.9%, Alfa Asesar, MA, USA). Silver mesh electrodes were also circular discs of 25 mm diameter. The position of these electrodes in the two reservoirs, and hence, their distances from the microchannel array could be adjusted from 1 mm to 36 mm.

4.3.1.3 Pressure Drop Measurement

A pressure transducer (PX26-030DV, Omega Inc. USA) was connected across the reservoirs to monitor pressure difference across the multi microchannel array. Omega's pressure sensor is a four-active piezo-resistive bridge device. When pressure is applied, a different output voltage proportional to a pressure is produced. The generated voltages were then converted to pressure values employing a calibration curve supplied by the manufacturer. The accuracy of pressure transducer was 1% of full scale (100 psi or 30 mV).

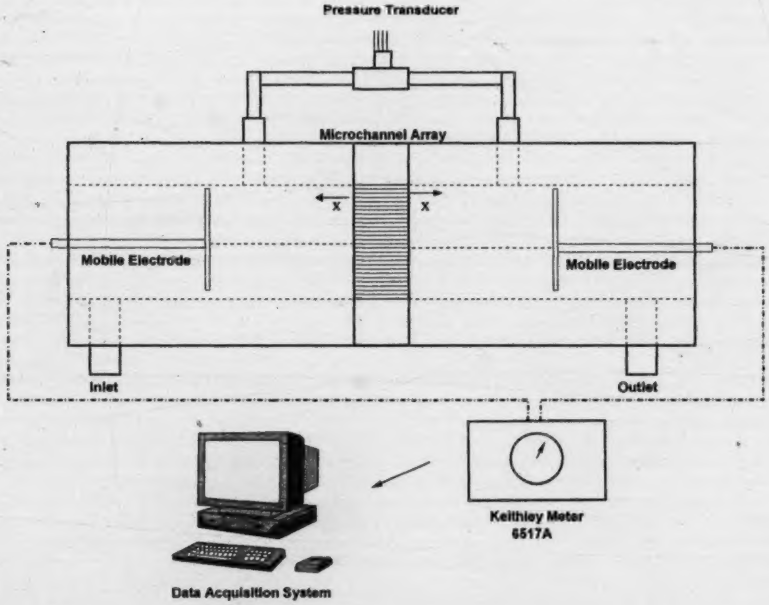
Pressure Transducer
Microchannel Array
x
x
Mobile Electrode
Mobile Electrode
Inlet
Outlet
Keithley Meter
6517A
Data Acquisition System

Figure 4.6: Schematic of the multi microchannel cell. The electrodes are movable across the reservoirs. The multi microchannel array thickness is 2 mm and the length of the reservoir is 36 mm. See text for details.

4.3.1.4 Multi Microchannels

Two microchannel arrays were employed in this study. The first sample was a microchannel array (Fig. 4.7) of 2 mm thickness and an effective diameter of 25 mm. It is made of untreated lead silicate glass (45 % SiO_2, 55% PbO)(Burle Electro-Optics, Sturbridge, Massachusetts) with approximately 3,437,500 circular and parallel microchannels, each of 10 μm diameter (Fig. 4.7). Number of pores and porosity obtained from manufacturer and the number of pores also verified experimentally through correlation between pressure losses and flow rates. The other sample used in this study was intended to emulate a single microchannel (microchannel with high electrical resistance) and comprises an array of 100 μm hexagonal pores. The effective diameter and length are 3 mm and 5 cm, respectively (Schott Inc). The sample is made of untreated lead silicate glass with approximately 550 pores.

4.3.2 Flow System

The experimental apparatus for characterizing the electrokinetic transport through the multi microchannel array is depicted in Fig. 4.5. The multi microchannel cell is connected to the other components of the system as described below:

4.3.2.1 Pump

Electrolyte solutions were drawn from a reservoir and forced through the multi microchannel array employing a positive displacement diaphragm pump (8000 series, Shurflo Inc. USA). The bypass pressure was 310 kPa. The pump was throttled across a valve to maintain a constant flow rate of 0.72 liter/minute.

4.3.2.2 Reservoir

The reservoir was a polyethylene cylindrical tank made by McMaster Inc. It had a translucent white color with 19 liter volume. The outer diameter and height were 0.28 and 0.39 meter, respectively. The tank includes a loose-fitting cover to prevent content contamination and evaporation. During the experiments half of the tank was filled with working electrolyte.

4.3.2.3 Flow Meter

The flow meter was a volumetric water flow meter (FLR-1620A, Omega Inc.). It continuously monitored the flow rate of system. The maximum readable flow rate was 1 liter/minute. The accuracy of flow meter was ± 2% of full scale.

4.3.2.4 Valves

As shown in Fig. 4.5 different types of valves were used in the apparatus. A shut-off valve was placed right at the pump outlet in order to stop the flow immediately. A flow control valve was placed after the shut-off valve to adjust the flow rate. Two three-way valves were installed before and after the multi microchannel cell to provide the ability to alternate the flow direction. Direction of fluid flow was reversed in fraction of a second when both valves were opened simultaneously.

4.3.3 Measurement System

Two electrometers (Keithley Inc., Model 6517A) were used to measure either the electric potential or current between the electrodes. For transient studies, the data acquisition was performed at the speed of 10 Hz with a resolution of 5 digits. In order to do so, in the configuration panel of the electrometer, the Number of Power Line Cycles (NPLC) (indicates how long an input signal is integrated to obtain a single measurement. Generally speaking, the longer a signal is integrated by the A/D converter, the more accurate the reading result) was set to be 0.8 PLC. A Labview program monitored and recorded the experimental data. The pressure drop and flow rate were also monitored. In addition, the response time and the accuracy of the measurements were verified employing a square wave generator.

4.3.4 Working Electrolytes

The experiments were performed for electrolyte concentrations of 4×10^{-5}, 1×10^{-4}, 10^{-3}, and 2×10^{-3} M KCl. The electrolyte solutions were prepared employing fresh DI water (not degassed) of 18.2 MOhm-cm specific resistivity (MilliQ 5, Millipore, MA). The pH and conductivity of electrolyte solutions were measured using Accumet Research AR50 meter (Fisher Scientific, CA). The experiments were conducted at constant temperature of 24°C.

4.3.5 Experimental Procedure

Before each experiment was performed, all samples, apparatus, pump, and connections were rinsed and washed with deionized water. The results were repeatable when the material was used as delivered from the manufacturer. To avoid contamination and reduction of the electrode polarization, the experimental protocol by Elimelech et al. [83] was employed by flushing the microchannel array with deionized water in both directions for a period of about two minutes to remove any trapped air bubbles. In SC/SP measurements, the electrolyte solutions were pumped into the array in alternating directions for a total of four times (two times in each direction) using the three-way valves.

Different modes of experiments were conducted using the apparatus. In the

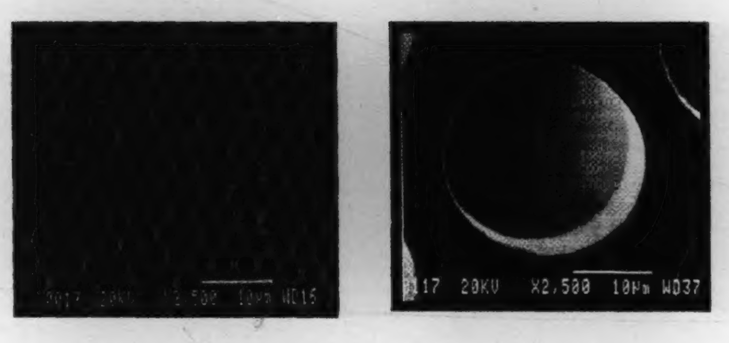

Figure 4.7: SEM images of a typical microchannel array which show an array of single, straight and circular microchannels. The array being used in this study has a pore size of 10 μm. Its thickness and diameter are 2 mm and 25 mm, respectively. Courtesy of Burle Electro-Optics, Sturbridge, Massachusetts.

SP mode of measurements, the electrodes (either platinized platinum or silver mesh) were connected to a voltmeter with a high input impedance. In the short circuit mode, the electrodes were connected to an ammeter. Apart from routine streaming potential and current experiments the multi microchannel cell allows the affects of electrode surface area and location to be explored. To systematically study the influence of electrodes placement on the extracted currents, several experiments were conducted. Platinized Pt electrodes initially were mounted 1 mm away from the array faces and streaming potentials and external currents were measured for selected electrolytes, then the electrodes were moved further to 2, 5, 10, 25 and 36 mm, respectively and data collection was repeated. The Rigidity of the Pt electrodes also allowed for accurate axial placement (±0.5 mm) and maintenance of the shape when subject to flow. In addition to experiments with platinized platinum electrodes, similar set of measurements were performed employing silver mesh electrodes.

4.4 Results and Discussions

4.4.1 Validation Tests

As primary validation tests, afew experiments were performed in the open circuit mode and the streaming potential versus pressure drop data were recorded and analyzed in the light of Smoluchoswki equation (Eq. 1.16). Streaming potentials were measured (employing the platinized platinum electrodes) for 0.1, 1 and 2 mM KCl all at pH of 6.6 ± 0.3 for a range of applied pressures (achieved by changing the flow rate). In the Smoluchoswki equation streaming potentials are proportional to applied pressures. Fig. 4.8 shows experimental data points fall very well in the regime of Smoluchoswki equation. Assuming double layer overlap and surface conductance effects are negligible, a ζ potential of -57 ± 3 mV was obtained when the working electrolyte was 2 mM KCl, pH of 6.6. The estimated ζ potential is similar to reported values in the literature [18] despite high percentage of lead in the glass.

4.4.2 Effect of Electrode Material, Surface Area and Location on the Measured Electrical Properties in a Multi Microchannel Array

Aside from electrode polarization there are other concerns about streaming current measurements in a multi microchannel array [84–86]. Fig. 4.9 depicts direct streaming potential/external current measurements employing platinized platinum and silver mesh electrodes for 1 mM KCl in identical flow rates. We interpret the experimental data by aid of electrical analogy presented in this chapter (Fig. 4.3 and Fig. 4.4). Contrary to the streaming potentials (Fig. 4.9a), the measured external currents depend on the electrode location, *i.e.* the closer the platinized platinum and silver mesh electrodes were to the array the

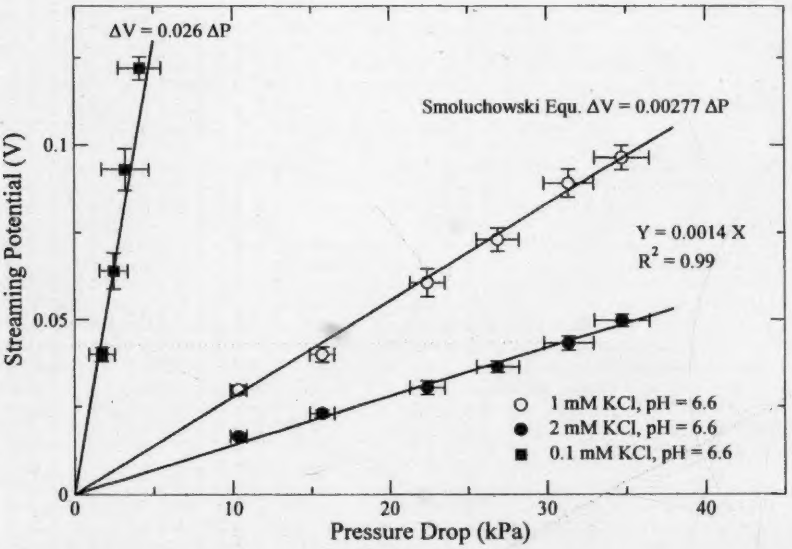

Figure 4.8: Streaming potentials vs. pressure drops, streaming potentials were measured for 0.1, 1 and 2 mM KCl all at pH of 6.6 ± 0.3 using the platinized platinum electrodes. ζ potential of the employed untreated glass was estimated to be -57 ± 3 mV at 2 mM KCl, pH =6.6. Comparison of Smoluchoswki equation and experimental data shows excellent agreement. Error bars are standard deviations.

smaller the R_B and the larger the external currents (Fig. 4.9b). Streaming potential measurements do not show these dependencies since they do not involve current flow in the reservoirs. When the channel length is very short and the porosity is high (*i.e.* millions of pores) the total conductance through the array becomes comparable to the conductance of the bulk fluid in the reservoirs where the electrodes were placed. In these cases, current drawn through a low resistance external electrical circuit connecting the electrodes in the two reservoirs (usually interpreted as the streaming current) becomes dependent on the location, material and surface area of the electrodes. From the electrical analogy point of view (see Fig. 4.3) in a steady state and based on Ohm's law one can write

$$\triangle V_{RL} = I_{array} \times \frac{R_{effective} \times (2R_B\frac{L}{A} + 2R_E + R_L)}{R_{effective} + 2R_B\frac{L}{A} + 2R_E + R_L} \tag{4.3}$$

where V_{RL} is the transcapillary potential across the multi microchannel array, R_B is bulk electrolyte resistance (MΩ-cm) in the reservoirs, R_E is the electrodes' resistance (Ω), R_L is internal resistance of measurement device (Ω) and L and A are the length and cross section area of the reservoirs and $R_{effective}$ is the multi microchannel array electrical resistance (Ω), respectively. In streaming potential measurements, R_L is extremely large *i.e.* $R_L \gg ((2R_B)\frac{L}{A} + R_{effective} + 2R_E)$ (see Fig. 4.4) and minor changes in the electrical resistance of system induced by the nature and location of electrodes do not influence the measurements of the electrical potentials. As such Eq. 4.3 simplifies to $\triangle V_{RL} = I_{array} \times R_{effective} \neq f(R_B, R_E)$. However, in streaming current measurements, ideally R_L is assumed to be zero and the external current, (I_{ext}) can be written as following,

$$I_{ext} = I_{array} \times \frac{R_{effective}}{R_{effective} + 2R_B\frac{L}{A} + 2R_E} \tag{4.4}$$

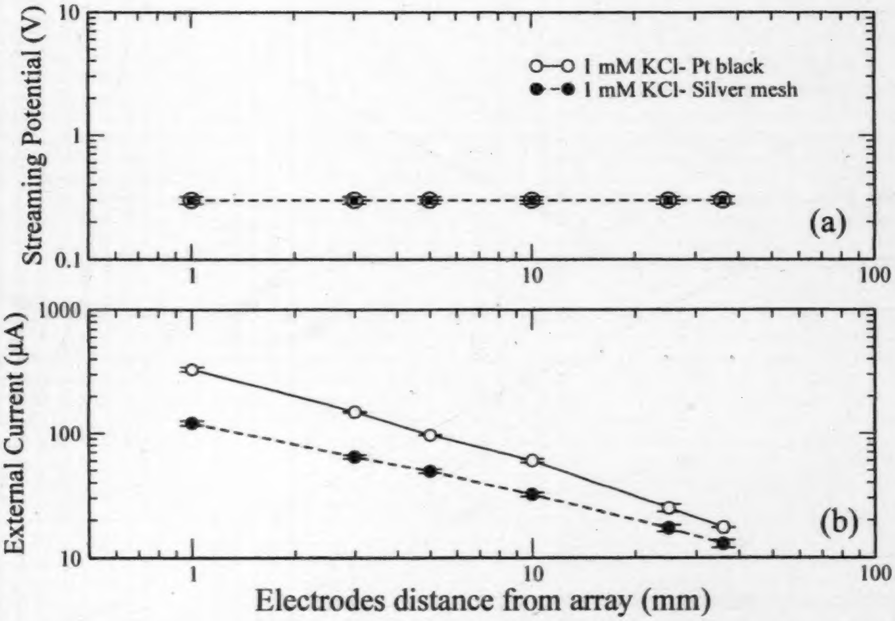

Figure 4.9: External current and streaming potential measurements in a multi microchannel array with 3,475,500 microchannels. The experiments were performed for 1mM KCl solution in identical flow rates, using platinized platinum and silver mesh electrodes. In order to avoid electrode polarization, the electrolyte solution was pumped into the array in alternating flow directions for a total of four times (two times in each direction)

In situations where $R_{effective} \simeq (2(R_B)\frac{L}{A} + 2R_E)$, the external current becomes a function of bulk and electrode electrical resistance; $I_{ext} = f(R_B, R_E)$. Therefore placement of the standard electrodes far away from multi microchannel array (L $\rightarrow \infty$, $R_B \rightarrow$ large, $I_{ext} \rightarrow 0$) or choosing non-standard electrodes and electrode polarization ($R_E \rightarrow$ large, $I_{ext} \rightarrow 0$), significantly affect the measured currents. In other words, in these situations the external currents are not representative of the streaming currents.

In Fig. 4.9b, it is clear that any displacement of the electrode, either platinized platinum or silver mesh significantly obscured measurement of the external currents. Also as evidenced by the same figure, a higher external current was captured by the platinized platinum electrode compared with the silver mesh *i.e.* the larger the surface area of electrode the smaller the R_E and consequently the higher are the corresponding currents. Fig. 4.10 shows external current measurements in another experiment for two different electrolytes (1mM KCl and 0.04 mM KCl) and identical flow rates (0.72 l/min). The change in the electrolyte concentration directly alters the bulk, R_B, and array, $R_{effective}$, electrical resistances. Consequently the higher the electrical resistance of bulk, the smaller are the external currents. We discuss and elaborate more on these issues in light of electrokinetic energy conversion devices in the next chapter.

4.4.3 Effect of Electrode Material, Surface Area and Location on the Measured Electrical Properties in Single Microchannels

Single microchannels are akin to wires with very high electrical resistance, and able to only conduct very low amounts of current ($\approx$ pA). Therefore detection of such currents is demanding and requires highly sensitive instruments. To circumvent the problem of low current, a multi microchannel array with only 550 pores was employed to boost the current while keeping the electrical resis-

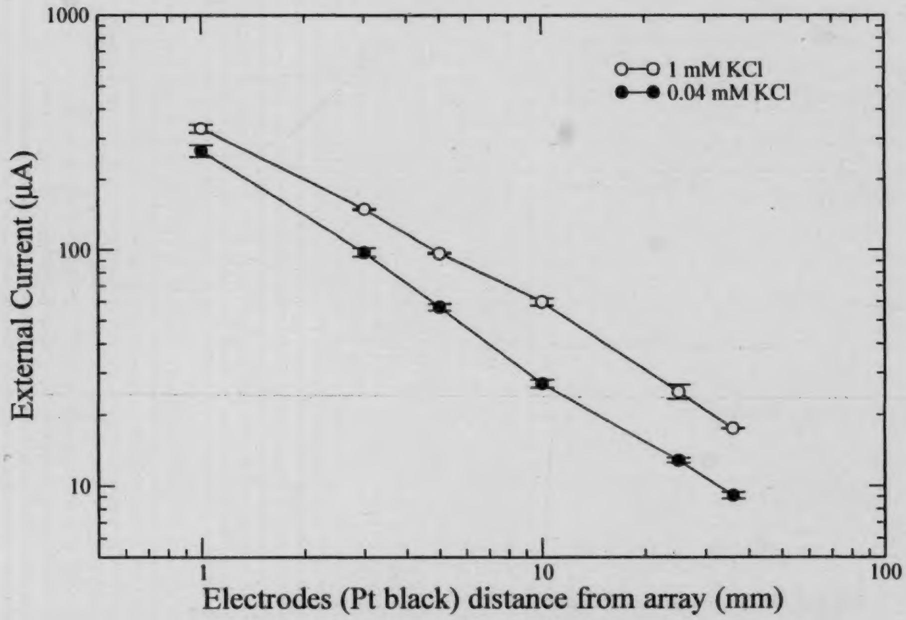

Figure 4.10: External current measurements in a multi microchannel array with 3,475,500 microchannels. The experiments were performed for 0.04 and 1 mM KCl solutions in identical flow filed conditions using platinized platinum electrodes. In order to avoid electrode polarization, the electrolyte solution was pumped into the array in alternating flow directions for a total of four times (two times in each direction)

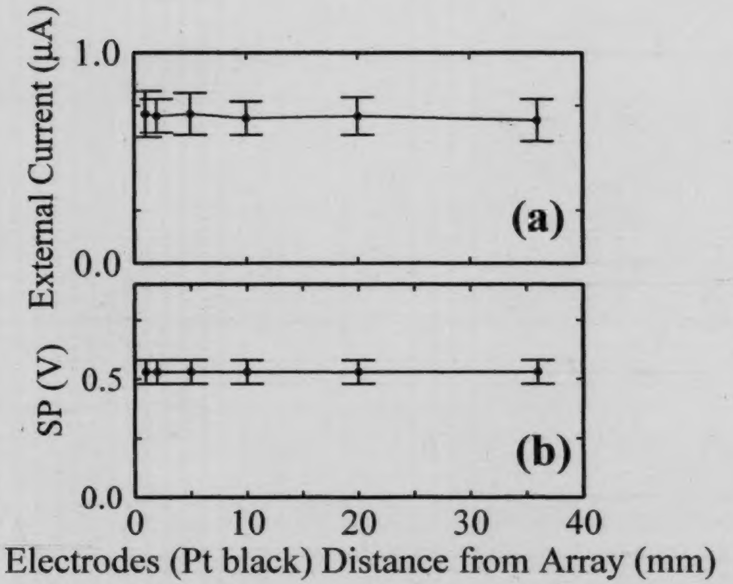

Figure 4.11: (a) Experimental external current values obtained for 1 mM KCl in a multi microchannel array with only 550 pores. (b) Experimental streaming potential values obtained for 1 mM KCl. Platinized platinum electrodes were used for both experiments. In order to avoid electrode polarization, the electrolyte solution was pumped into the array in alternating directions for a total of four times (two times in each direction)

tance high. Fig. 4.11 shows the measured streaming currents and potentials across the array. As seen when $R_{effective} \gg (2(R_B)\frac{L}{A} + 2R_E)$, (*i.e.* akin to a single microchannel) displacement of electrodes (*i.e.* L) and size of reservoirs (*i.e.* A) have negligible effect on total resistance, therefore external current measurements across the reservoirs remain constant similar to streaming potentials data. Electrode material and surface area still play an important role as electrode polarization is inevitable.

4.5 Conclusions

The magnitude of the measured currents in the external circuit was observed to be highly dependent on the location, material and surface area of electrodes when the array's electrical resistance is comparable to the electrolyte resistance and is therefore not representative of the streaming currents. Ideally, in streaming current measurements in multi microchannel arrays and porous media with low electrical resistance, there should not be any distance between electrodes and the media. In contrast, the streaming potential was found to be essentially independent of these parameters; however, estimating the total conductance introduces other problems. In single microchannels streaming current and streaming potential both are independent of the location of the electrode. With respect to ζ potential estimation the use of streaming current appeared to be rather complicated and difficult to accomplish especially in porous media. This complexity will be greatly simplified when one deals with streaming potential. Our results have important implications for estimation of ζ-potentials from streaming current methods and electrokinetic energy conversion devices (see next chapter).

CHAPTER 5

NANOGOLD ELECTRODES: CHARACTERIZATION AND ITS IMPACT ON STREAMING CURRENT DEVICES

5.1 Introduction

Energy conversion devices[1] based on electrokinetic phenomena have been studied over the past five decades [20, 43, 57, 75, 87, 88]. A recent study by Yang *et al.* [20] revived interest in this concept [89–91]. The core principle underlying many electrokinetic energy conversion devices is creating a streaming potential difference across a naturally charged porous medium. This potential is generated by a pressure driven flow of a conducting fluid through the porous medium [20, 57, 75, 88]. Provided the streaming potential can be maintained while current is drawn through an external electrical circuit, such a device maybe viewed as a system to directly convert flow work to electrical work. However, most studies reported very low power (nW) and efficiency (less than 1 %, sometimes as low as 10^{-3} %) [20, 57, 92]. One bottleneck in these devices originates from a lack of proper method for driving the current in an external circuit. The current is extracted through electrodes placed across the porous medium. Many recent studies placed these electrodes at arbitrary distances from the porous media [20, 81, 92–95]. However, based on observations in Chapter 4, it was concluded that streaming current measurements in a multi microchannel array with millions of channels are highly dependent on the location and material of the electrodes. Hence leaving any gap between the electrodes and the porous medium lessens the efficiency of energy conversion. In this chapter, a specifically made microchannel array coated with a 100 nm thick layer of gold (nanogold electrodes - NGEs) on both faces is utilized as a streaming current device. The objectives of this chapter are threefold: (i) to characterize NGEs employing an electrical analogy and to estimate the electrical resistance and capacitance of NGEs subject to an alternating flow of electrolyte solution (This process is similar to cyclic voltammetry which determines the capacitance of electrochemical interfaces); (ii) to perform streaming current and streaming potential measurements using NGEs; and (iii) to study the electrokinetic energy conversion using the gold coated array. The purpose of these nanogold electrodes (NGEs) was to provide a direct measure of the electrical properties right at the multi microchannel array faces, and serve as a benchmark to compare the electrical signals measured through the platinum electrodes placed in the reservoirs. Different modes of experiments were conducted using the apparatus. In the streaming potential mode of measurements, the electrodes (either platinum or NGEs) were connected to a voltmeter. In the streaming current mode of operation, the electrodes were connected to an ammeter. To provide better insight into the physical processes occurring, the electrometers connected to these electrodes were also switched between voltage measurement and current measurement modes during these experiments as required (See Fig. 5.1). Since in practice electrode polarization occurs, an equivalent electrical analogy was proposed to mimic the behavior of this streaming current device and to assess the polarizability of the NGEs in a range of electrolyte solutions. Electrical analogy

---

[1] Part of this chapter is closely related to a manuscript under preparation by "Ali Mansouri, Subir Bhattacharjee and Larry Kostiuk" to be submitted in Applied Physics Letters, 2007

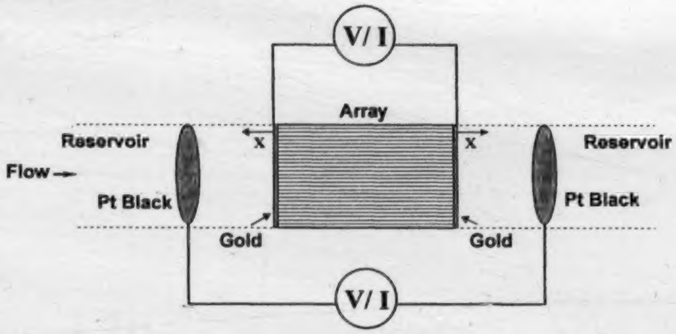

Figure 5.1: (a) Schematic of the experimental apparatus. 3,437,500 of parallel microchannels formed a multi microchannel array (25 mm effective diameter) akin to a porous medium. In experiments platinized platinum electrodes (25 mm diameter) were movable within the reservoirs. Nanogold electrodes (NGEs) were on the faces of the microchannel array. The microchannel array thickness was 2 mm and the length of the reservoirs was 36 mm, .

circuit was tailored to capture the transient response of the device when current and voltage were measured from the NGEs and platinum electrodes simultaneously. With the aid of the electrical analogy, electrokinetic energy conversion was studied and the maximum power of the device subject to an appropriate external resistance was estimated.

5.2 Experimental Apparatus

The details of experimental apparatus used in this study were provided in Chapter 4 (see Fig. 4.3 and Fig. 5.1). The porous medium comprises a 2 mm thick microchannel array of diameter 25 mm made of untreated lead silicate glass (45 % SiO_2, 55% PbO) (Fig. 5.2) (Burle Electro-Optics, Sturbridge, Massachusetts) and had approximately 3,437,500 circular and parallel microchannels, each of 10 μm diameter. The two surfaces of the porous microchannel array were uniformly coated with nano layers of Gold (Au) supported by an adhesion layer of

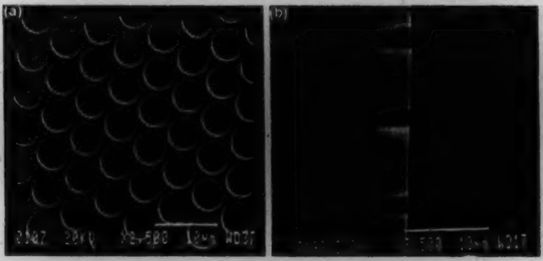

Figure 5.2: (a) A SEM image of a multi microchannel array coated with a nano layer of gold. It shows an array of single, straight and circular microchannels. It is made of untreated lead silicate glass with 55% porosity. (b) Longitudinal cross section of the microchannels. Metal penetration depth inside the capillaries is shown. Bright area indicates the gold deposited area. In the current sample the penetration depth is 0.3-0.7 times of channel diameters on both sides. Penetration depth is negligible compared to the thickness of the multi microchannel array (2 mm). The sample has a pore size of 10 μm and thickness and effective diameter of 2 mm and 25 mm, respectively. (Courtesy of Burle Electro-Optics, Sturbridge, Massachusetts.)

Nichrome. The thin metal coating had an overall thickness of 100 nm. SEM micrographs of the porous substrate are shown in Fig. 5.2. As evidenced from these micrographs, the sputtering process employed to deposit the metal coatings on the glass did not block the capillary entrance and exits. However, there was a penetration of the metal to an extent of approximately 10 μm from both ends into the capillary. Prior to the experiments, it was ensured that the sputtered layer of gold was continuous through electrical resistance measurements. Furthermore, it was ensured that no electrical connectivity existed between the gold coatings on the two opposing faces of the multi microchannel array. Electrolyte solutions of 0, 0.05, 0.1, and 0.5 mM KCl were pumped through the multi microchannel array in alternating flow directions using the 3-way valves (see Fig. 4.5). The transient response of electrical properties; either electrical current or potential were monitored and recorded using a Labview program. The data acquisition was performed at the speed of 10 Hz.

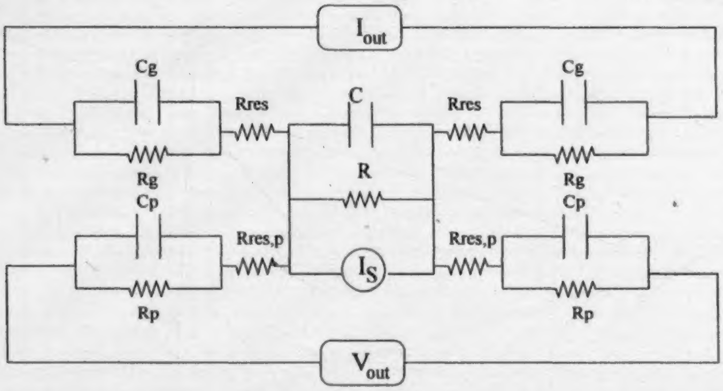

Figure 5.3: An equivalent electrical analogy of the streaming current device. I_s, R and C represent the current source, total electrical resistance and total capacitance of the multi microchannel array. R_g, C_g, R_p and C_p are the electrical resistance and capacitance of NGEs and platinum electrodes. R_{res} and $R_{res,p}$ are the bulk electrolyte resistance inside the reservoirs

5.3 Electrical Analogy of a Streaming Current Device

An electrical analogy circuit equivalent to the streaming current device is proposed to interpret the streaming current and streaming potential measurements and to assess the polarizability of the NGEs. The interactions between electrokinetic flows, electrodes and external circuits can be explained by the equivalent electrical analogy of the system. The electrical analogy circuit was tailored to capture the transient response of the device when current and voltage were measured from the NGEs (at the multi microchannel array faces) and the platinized platinum electrodes (located inside the reservoirs) simultaneously. Such an equivalent electrical circuit is shown on Fig. 5.3. I_s, R and C represent the current source, total electrical resistance and total capacitance of the multi microchannel array. R_g, C_g, R_p, C_p are the electrical resistance and capacitance of the NGEs and platinum electrodes. R_{res} and $R_{res,p}$ are the bulk electrolyte resistance inside the reservoirs. The resistance and capacitance of the

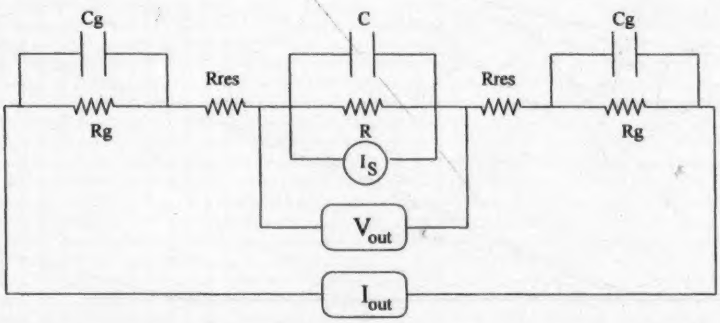

Figure 5.4: A simplified version of electrical analogy. See text for details

platinized platinum electrodes and bulk electrolyte resistance, connected to a voltmeter with high input impedance were negligible as a minuscule current passes through the platinum electrodes. In order to simplify the circuit and find its solution, simplified versions of our electrical analogy are depicted on Fig. 5.4 and Fig. 5.5. R_t and C_t show the total electrical resistance and capacitance of the NGEs, and $R_{res,t}$ is the total bulk electrolyte resistance. The circuit was solved using Laplace transforms. The current being measured by the ammeter can be written as $I_{out} = I_{source}.Y(s)$ where Y(s) is a Laplace transform function; $Y(s) = \frac{R+RR_tC_tS}{S(\alpha S^2+\beta S+\gamma)}$, where

$$\alpha = RC_tR_tR_{res,t}C_t$$

$$\beta = RR_tC_t + R_tR_{res}C_t + RC(R_t + R_{res,t})$$

$$\gamma = R + R_t + R_{res,t},$$

considering a step function as the input; I_{out} yields

$$I_{out}(t) = I_{source}(A + Be^{(-\frac{t}{\tau_1})} + De^{(-\frac{t}{\tau_2})}) \tag{5.1}$$

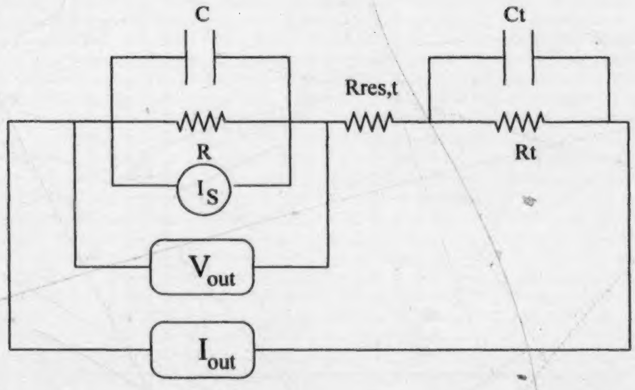

Figure 5.5: Final simplified version of the electrical analogy. R_t and C_t show the total electrical resistance and capacitance of the NGEs and $R_{res,t}$ is the total bulk electrolyte resistance.

where τ_1 and τ_2 are the time constants. Such a current induces a voltage across the array

$$V_{out}(t) = I_{source}R(1 - A - Be^{(-\frac{t}{\tau_1})} - De^{(-\frac{t}{\tau_2})}) \tag{5.2}$$

Since NGEs were employed, there was virtually no distance between NGEs and multi microchannel array. Therefore the electrical resistance of the bulk electrolyte, $R_{res,t}$ was assumed to be negligible. This assumption simplified our solution furthermore ($\tau_1 = \tau_2$) and $I_{out}(t)$ and $V_{out}(t)$ reduced to

$$I_{out}(t) = I_{source}(A + Be^{(-\frac{t}{\tau_1})}) \tag{5.3}$$

$$V_{out}(t) = I_{source}R(1 - A - Be^{(-\frac{t}{\tau_1})}) \tag{5.4}$$

where

$$A = \frac{R}{\gamma}$$

$$B = (\frac{RR_tC_t}{\beta} - \frac{R}{\gamma})$$

and the new time constant; τ_1 was written as

$$\tau_1 = \frac{\beta}{\gamma} = (\frac{RR_t}{R+R_t})(C+C_t) \tag{5.5}$$

The capacitance of NGEs; C_t is the parameter of primary interest in Eq. 5.5. The rest of the parameters, namely, the time constant and electrical resistance of the electrodes and multi microchannel array were obtained experimentally. The capacitance of the multi microchannel array was estimated based on numerical findings discussed in Chapter 3 and briefly given below.

5.3.1 Estimation of a Multi Microchannel Array Capacitance

In Chapter 3, we showed that the capacitance of a single circular microchannel obeys the behavior of a parallel plate capacitor and hence the capacitance solely is a function of geometry and permittivity. Capacitance of a single circular microchannel is given by

$$C = 3\frac{\epsilon A}{L} \tag{5.6}$$

where C is capacitance, L is microchannel length, ϵ is the primitivity of electrolyte solution and A is the cross-sectional surface area of a single microchannel. The above correlation implies that "A", "L" and permittivity are the only parameters that alter the capacitance of a single microchannel. Hydrodynamics, electrostatics, ζ potential and mass transfer have essentially negligible effects on permittivity and capacitance (Chapter 3). As capacitance is additive in parallel circuits, the total capacitance of a multi microchannel array is

$$C = 3N\frac{\epsilon A}{L} \tag{5.7}$$

where N is the number of microchannels. In this study, the capacitance of the multi microchannel array was estimated based on Eq. 5.7.

5.3.2 Estimation of a Multi Microchannel Array Electrical Resistance

Porous media and membranes are of interest in pure and applied science. Several AC and DC techniques have been employed to estimate the electrical properties of such media [96]. These techniques are instrumentally demanding and interpretation of such data are non-trivial due to phenomena such as concentration polarization, electrode polarization and frequency dependence of electrical impedance [84, 85].

Streaming potential phenomena, however, is considered as a DC phenomenon. In this study, the total electrical resistance of the multi microchannel array was estimated by performing two separate experiments namely streaming potential measurement and transcapillary potential measurement when an external resistance was paralleled with the cell. Based on Kirchoff's law and in a steady state one can write the following for the equivalent circuit shown in Fig.5.6 for two different external resistances; R_{ext1} and R_{ext2}

$$\frac{V_1}{V_2} = \frac{(R_{ext1} + 2R_{res} + 2R_1)(R + R_{ext2} + 2R_{res} + 2R_1)}{(R_{ext2} + 2R_{res} + 2R_1)(R + R_{ext1} + 2R_{res} + 2R_1)} \tag{5.8}$$

where V_1 and V_2 are the induced potentials with respect to the external resistances. There was virtually no electrolyte solution between the multi microchannel array and the NGEs and thus R_{res}=0. The electrode's resistance

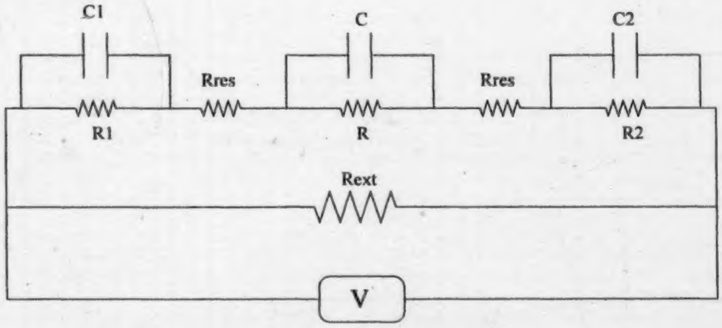

Figure 5.6: Equivalent electrical circuit of microchannel array coated with a nano layer of gold in parallel with an external resistance. R and C are the electrical resistance and capacitance of the multi microchannel array, R_1 and R_2 represent the nanogold electrodes resistance. R_{res} shows the reservoir electrolyte resistance. R_{ext} is the external resistance parallel to the multi microchannel array.

can be neglected since in one experiment streaming potential was measured and in another only a minuscule external current was extracted. It is known that as R_{ext1} approaches infinity, the measured potential approaches the streaming potential; $V_1 = StreamingPotential$ when $R_{ext1} \to \infty$. With these assumptions, Eq. 5.8 simplifies and yields the resistance of the multi microchannel array; R:

$$R = R_{ext2}(\frac{(StreamingPotential)}{V_2} - 1) \tag{5.9}$$

A series of experiments were conducted for KCl electrolyte solutions and resistance of the multi microchannel array was obtained using Eq. 5.9. The results were compared with theoretical values as depicted in Fig. 5.7. The theoretical value was obtained employing the following equation

$$R = \frac{L}{1000NAM \sum \lambda_i \nu_i} \tag{5.10}$$

where L, N, A, M, λ_i and ν_i are the length of the multi microchannel array (2

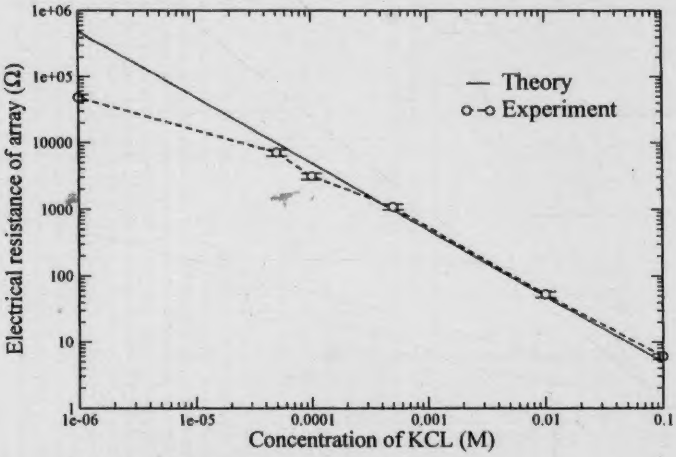

Figure 5.7: Electrical resistance of the multi microchannel array vs. Concentration of the KCl electrolyte solution.

mm), number of microchannels (3,437,500), surface area of a single microchannel (radius 5 μm), molarity of the electrolyte solution, molar electrical conductivity (K^+ and Cl^-, Sm^2/mol) and stoichiometric numbers of cations and anions, respectively. As can be seen, the agreement is excellent for higher salt concentrations ($> 10^{-4}$ M KCl). The deviation of curves at lower salt concentrations is believed due to estimation of theoretical values on the basis of bulk conductance and not considering the surface conductance. The 10^{-6} M KCl electrolyte solution was prepared by adding no salt to DIUF water (0 M KCl). Due to uncertainties associated with conductivity of 0 M KCl, it was only used for the study of electrokinetic energy conversion as one experimental evidence among other electrolyte solutions.

5.4 Capacitance and Resistance of Nanogold Electrodes

The experimental method being described here stems from the cyclic voltammetry technique [47]. Many of the voltammetric techniques deal with application of known potentials to an electrode and recording the resulting currents. The current response over a range of potentials is measured and then the direction of the potential scan is reversed back to the starting potential (cyclic pattern). The main difference between voltammetry and the method being used in this chapter is that the potential (transcapillary potentials) is induced by pressure driven flow of the electrolyte solutions rather than the external potential sources and cyclic patterns occur due to the alternating flows. In order to characterize and estimate the capacitance and resistance of NGEs, a series of streaming current experiments were performed. Ideally, the reduction - oxidation reactions at the NGEs interface will be fast enough that no charge will accumulate at the electrode interface. However, in practice, NGEs are susceptible to polarization (The extent of polarization increases with electrolyte concentration as evidenced by results shown later). The electrolyte solution of 0.05, 0.1, and 0.5 mM KCl were chosen for experiments and were pumped through the multi microchannel array in alternating flow directions. In these experiments platinized platinum electrodes detect the potentials developed across the multi microchannel array while the NGEs extract the currents. A typical run for such experiment is shown in Fig. 5.8. The repeatability of the data was excellent except for the first cycle of measurements in which it is believed that the presence of stationary electrical double layer attenuated measured currents.

We note that the evolution of the streaming current was ruled by the hydrodynamic time scale as evidenced by the numerical results presented in Chapter 2. However, decay of current due to accumulation of charge at electrode-electrolyte

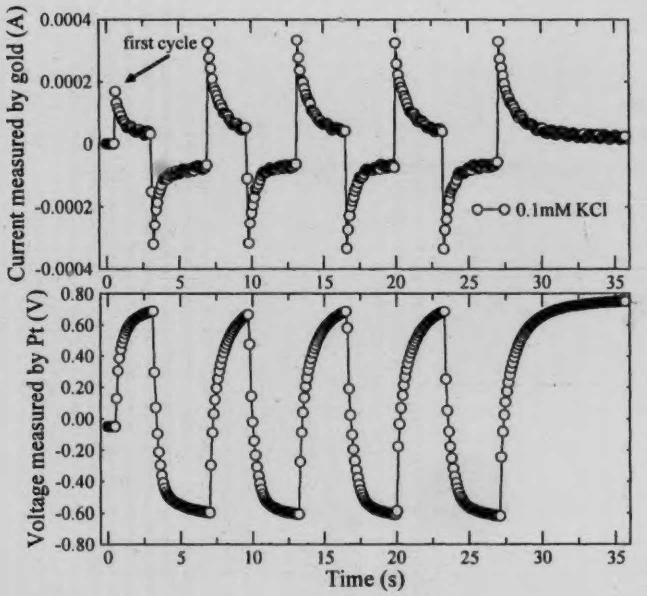

Figure 5.8: Simultaneous measurement of current and voltage by NGEs and platinized platinum electrodes across the multi microchannel array. An electrolyte solution of 0.1 mM KCl was pumped through the multi microchannel array in alternating flow directions. Since electrodes were unable to digest all the free charges, consequently a potential developed and detected by platinum electrodes. In streaming current measurements using NGEs, value of first peak was smaller compared to other peaks due to presence of stationary electrical double layer in first cycle of experiments.

Electrolyte	SP	SC	R	R_t	$R_{res,t}$	τ_1	C	C_t
mM KCl	V	μA	Ω	Ω	Ω	s	nF	μF
0.5	0.25	227	1102	10555	$\approx$0	0.25	$\approx$0.28	251
0.1	1	319	3133	9375	$\approx$0	0.4	$\approx$0.28	170
0.05	2.5	348	7185	6666	$\approx$0	0.51	$\approx$0.28	147

Table 5.1: Characteristics of NGEs and multi microchannel array for three different electrolytes. R and C represent the total resistance and total capacitance of the microchannel array. R_t and C_t are the corresponding total resistance and capacitance of NGEs. $R_{res,t}$ is the total bulk electrolyte resistance between NGEs and multi microchannel array. τ is the time constant of decay of current obtained from experimental data.

interface was governed by diffusion and migration time scales. Time constants of such decays was obtained by curve-fitting of Eq. 5.3 for working electrolytes. The response time of the electrometer and data acquisition system in the current mode was adequate enough to capture the behavior of the system (time constants were on the order of few seconds and the data acquisition was performed at the speed of 10 Hz). Eq. 5.5 was employed to quantify the polarization of the NGEs and to estimate the parameter of interest, namely, the capacitance of the NGEs, see Table 5.1. The electrical resistance of the NGEs was obtained by dividing the steady state potentials detected by the platinum electrode over the steady state currents detected by NGEs. As noted before, the capacitance of the multi microchannel array remains constant. However, the electrical capacitance and resistance of the NGEs increases with electrolyte concentration. The specific capacitances of the NGEs are very large compared to multi microchannel array capacitance. The reason for this is that the thickness of the double layers (physical distance between separated charges) is on the order of nm whereas the multi microchannel array thickness is on the order of mm (see Eq. 5.6). Moreover, capacitances of double layer reported in Table 5.1 are in good agreement with those obtained with cyclic voltammetry [47].

5.5 Estimation of Streaming Currents in a Multi Microchannel Array

So far we have evidenced the difficulties associated with direct streaming current measurements. Not only was electrode polarization a serious concern, but electrodes' location, material and surface area altered and attenuated the measured currents in the multi microchannel array. To our knowledge, only a couple of studies in the literature elaborated on this problem in detail [84, 85] and provided solutions. The idea developed by Bijsterbosch *et al.* [84] was to obtain the streaming potential, streaming current and conductance of a porous plug from a single experiment. However, their approach was dependent on the type of electrode and hence the estimation of streaming current was subject to inaccuracies [85]. We believe estimating both conductance and streaming current from a single experiment may not be practical. In this work, conductance and streaming potential were both obtained separately. As explained before in Section 5.3.2, the electrical resistance of the multi microchannel array was obtained by two separate experiments, namely, streaming potential measurement (external resistance approaches infinity) and transcapillary potential measurement (external resistance had a value of 9924 Ω). The conductances of the multi microchannel array was estimated using the electrical resistance values obtained by Eq. 5.9. In the limit of Smoluchoswki's equation (streaming potential and streaming current follow ohm's law), experimental data were used to create a line on a V-I plot. This line was positioned by a point (*i.e.* streaming potential) and the slope (*i.e.* conductance) as depicted in Fig. 5.9, Fig. 5.10 and Fig. 5.11. The intersection of the Y axis and Smoluchoswki equation represented an estimate of the streaming current in the multi microchannel array for the working electrolyte solutions (see Table 5.1). We furthermore compared the

Smoluchoswki equation with the current-voltage plot extracted from transient response of current and voltage (*i.e.* Fig. 5.10) measured by the NGEs and platinized platinum electrodes. It is evident from Fig. 5.9, Fig. 5.10 and Fig. 5.11 that the agreement is adequate. However, the extent of polarization varies. Such variations can be explained by comparison of the electrodes' capacitance and resistance, namely, electrode impedance (Table 5.1). In the case of dilute electrolyte solutions namely, $n_\infty < 0.05$ mM KCl, electrical resistance and capacitance of the electrodes were small, thus polarization was not significant. On the contrary, for concentrated electrolyte solutions, $n_\infty > 0.5$ mM KCl, electrical resistance and capacitance of electrodes were large enough to prevent the electrochemical reactions at electrode-electrolyte interface and resulted in an extensive polarization of electrodes. In order to prevent electrode polarization one simple but effective method (not applicable for concentrated electrolytes) was to reverse the flow direction. Such behavior can be seen in Fig.5.9, Fig.5.10 and Fig.5.11. It can be inferred that for dilute electrolyte solutions *e.g.* 0.05 mM KCl, reversing the fluid flow direction essentially resulted in a reasonable estimate of streaming current, however, in concentrated electrolytes *e.g.* 0.5 mM KCl failure of NGEs were obvious. The alternative method for $n_\infty > 0.5$ mM KCl was to use of Smoluchoswki equation.

In summary, it can be inferred from these cyclic measurements that the EK transport behavior of this NGEs becomes seriously affected by electrode polarization at higher ionic strengths. At lower ionic strengths, however, the results are in agreement with the Smoluchoswki equation and the transient spike of current caused by flow reversing provides a reasonable estimate of streaming current.

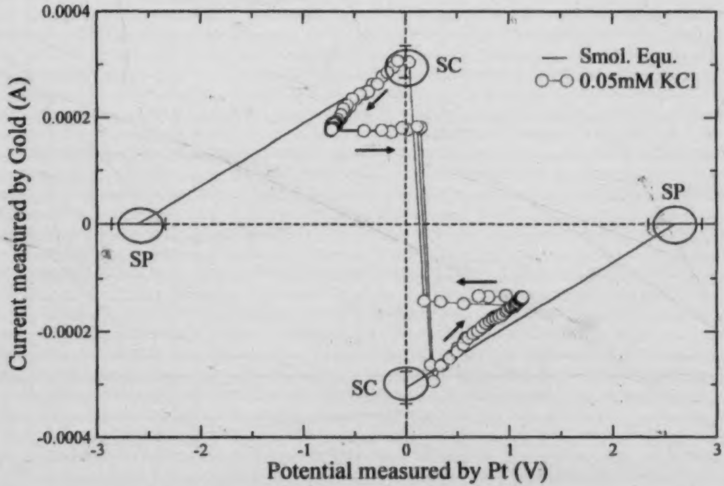

Figure 5.9: Comparison of Current-Voltage plot with Smoluchoswki equation. The Current-Voltage plot extracted from transient response of current and voltage measured by NGEs and platinized platinum electrodes simultaneously. Smoluchoswki equation was plotted using independent values of streaming potential and conductance of the multi microchannel array. The intersection of Y axis and Smoluchoswki equation represents an estimate of streaming current in the multi microchannel array for electrolyte solution of 0.05 mM KCl.

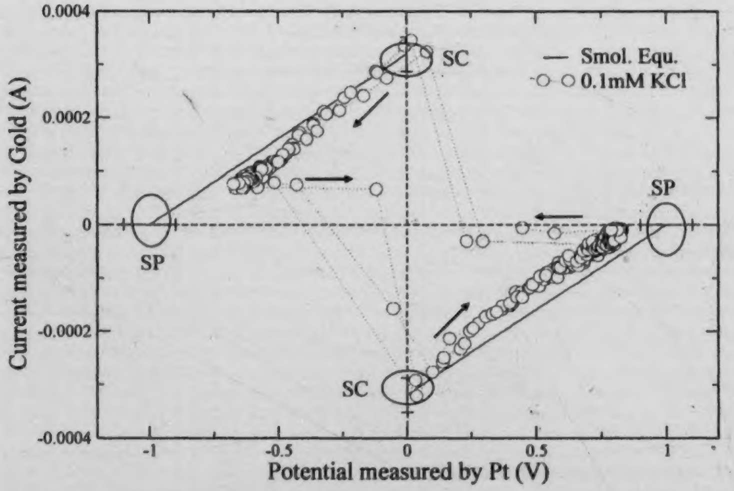

Figure 5.10: Comparison of Current-Voltage plot with Smoluchoswki equation. The Current-Voltage plot extracted from transient response of current and voltage measured by NGEs and platinized platinum electrodes simultaneously. Smoluchoswki equation was plotted using independent values of streaming potential and conductance of the multi microchannel array. The intersection of Y axis and Smoluchoswki equation represents an estimate of streaming current in the multi microchannel array for electrolyte solution of 0.1 mM KCl.

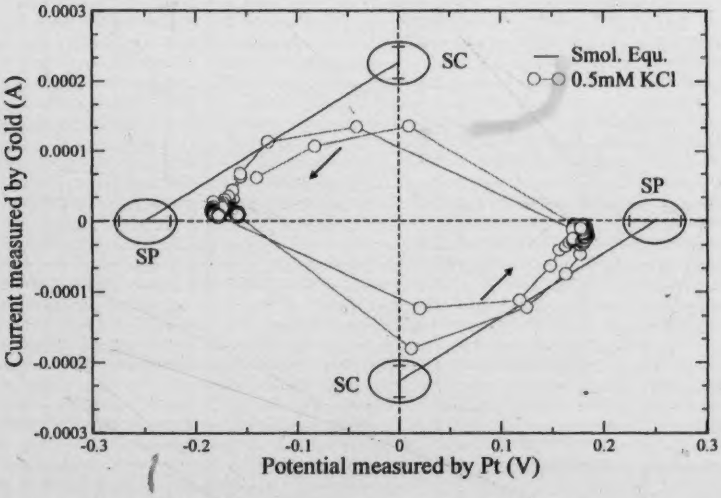

Figure 5.11: Comparison of Current-Voltage plot with Smoluchoswki equation. The Current-Voltage plot extracted from transient response of current and voltage measured by NGEs and platinized platinum electrodes simultaneously. Smoluchoswki equation was plotted using independent values of streaming potential and conductance of the multi microchannel array. The intersection of Y axis and Smoluchoswki equation represents an estimate of streaming current in the multi microchannel array for electrolyte solution of 0.5 mM KCl.

5.6 Energy Conversion in a Streaming Current Device

The demand for power generation at any scale and efficiency due to emergence of ultra-low power consumption devices is fast increasing. Devices that can scavenge power from human activity or derive limited energy from ambient heat, light, radio frequencies or vibration [97] or for instance a motor which runs only with 10 nA current [98]. In the context of streaming current devices, recent study by Yang *et al.* [20] renewed interest in this subject for electrokinetic flows. Followed by their work, there have been several works, both experimentally and theoretically [48, 75, 92, 93, 99–104]. Many recent studies placed the electrodes that derive the power from such devices arbitrarily at varying distances from the porous media [20, 92–95]. However, based on the observations in Chapter 4, it was concluded that streaming current measurements in porous media are highly dependent on location and material of electrodes and hence leaving any gap between the electrodes and medium obscure the measured currents.

We once again repeated these experiments on a multi microchannel array but this time coated with nano layers of gold on both faces (NGEs). In this case, the measured electrical properties inside the reservoir was compared with NGEs measurements for electrolyte solutions of 0 M KCl and 0.5 mM KCl. As depicted in Fig.5.12 similar behavior can be seen for the measurements inside the reservoir; constant streaming potentials and attenuated external currents across the reservoir. Streaming potentials measured by NGEs were in agreement with those measured in reservoir neglecting the residual potential of the multi microchannel array. However, the scenario for the measured currents by NGEs was different. Right at multi microchannel array faces the current measured by NGEs for 0 M KCl was larger than 0.5 mM KCl contrary to measured currents inside reservoir. In the light of electrical analogy model, as we discussed

Electrolyte	Conductivity	SP	SC	Max. Power	η
M	μS/m	V	μA	mW	%
Fresh 0 M KCl	50	15.5	260	$\approx$1	1.3
Old 0 M KCl	102	4.2	145	$\approx$0.152	0.2
0.05 mMKCl	450	2.5	100	$\approx$0.0625	0.02
0.1 mMKCl	1600	1	10	$\approx$0.0017	0.002
1 mMKCl	14600	0.07	0	$\approx$0	0

Table 5.2: Experimental data obtained by NGEs for various electrolytes. Values are average of four successive measurements. Streaming potentials/currents were measured after the interface between liquid-solid surface reached the equilibrium state. Steady state streaming currents and potential were reported. Maximum of power was estimated on the basis of external currents and streaming potentials. Efficiency was estimated based on the traditional definition of efficiency; $\eta = \frac{Electricalwork}{Flowwork}$

before, it is clear that the electrical resistance of bulk electrolyte attenuated the measured current data, particularly for the case of 0 M KCl. Therefore in the context of the streaming current device, NGEs should be employed instead of platinized platinum electrodes. Table 5.2 reports energy conversion results of the streaming current device. Maximum power of a streaming current device can be estimated by considering an equivalent external resistance parallel to the device (see fig.5.13). We note that power of streaming current device approached zero when the system was subjected to concentrated electrolyte solutions; $n_\infty \geq 1$ mM KCl. However, it is striking that 10 μm multi microchannel array generates a maximum power of $\sim$ 1 mW with respect to 26 kPa pressure drop. Efficiency was estimated from traditional definition of efficiency $\eta = \frac{Electricalwork}{Flowwork}$ and 1.3% efficiency was obtained by employing NGEs. The power density required by ultra-low power consumption devices such as wireless sensors and MEMS and NEMS devices is in the order of $\mu W/cm^3$ which interestingly meets the power generated by the streaming current device [20, 97].

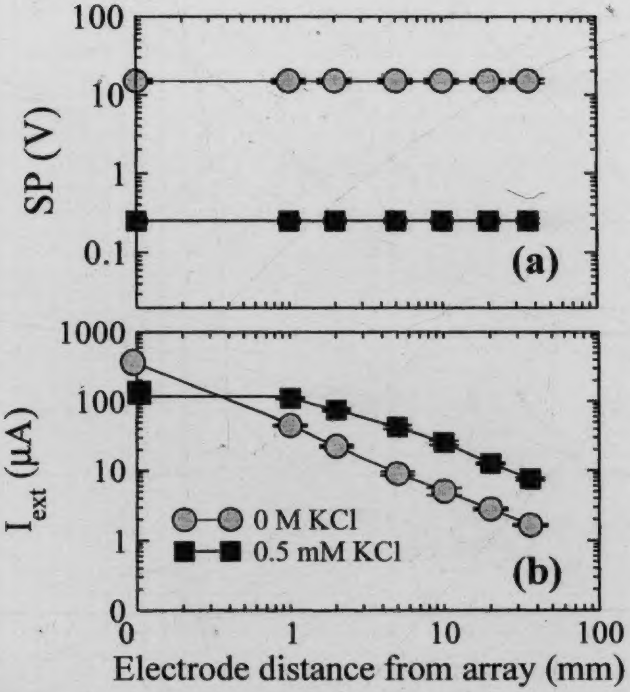

Figure 5.12: a) Streaming potentials measured with platinized platinum electrodes and NGEs across the reservoirs and right at the multi microchannel array faces for 0 M KCl and 0.5 mM KCl. b) Corresponding external current obtained by platinized platinum electrodes (inside reservoirs) and NGEs (at multi microchannel array faces) for the same electrolyte solutions. Experiments were conducted in an identical flow rate of 0.72 l/min.

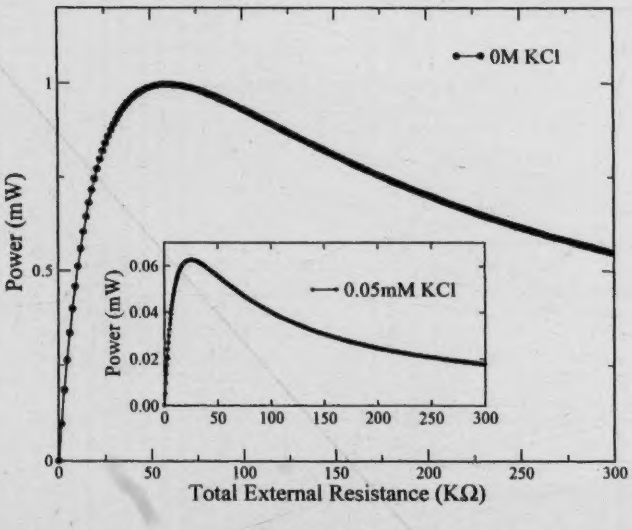

Figure 5.13: Power of the streaming current device vs. Total external resistance. The maximum power occurred at the point where total external resistance becomes identical to electrical resistance of the device. Addition of salt virtually reduced device performance (inset).

5.7 Conclusions

In this chapter the streaming potential and streaming current phenomena induced by pressure driven flows of electrolyte solutions through a multi microchannel array specifically coated with a nano layer of gold on both faces (nanogold electrodes) were studied. An equivalent electrical analogy was employed to interpret experimental findings. Some of key observations were:

1) Nanogold electrodes failed in direct streaming current measurements due to electrode polarization. If the electrolyte concentration, $n_\infty < 0.1$ mM KCl, reversing flow direction and recording transient response of current was an effective method to obtain an estimate of streaming current. However, for $n_\infty >$ 0.1 mM KCl, NGEs were essentially not functional.

2) It was shown that for electrolyte concentration, $n_\infty > 0.1$ mM KCl,

streaming currents can be estimated by aid of Smoluchoswki equation and two separate experiments namely streaming potential and conductance measurement.

3) The capacitance of the gold-electrolyte electrochemical interface was estimated by transient measurement of currents and induced voltages and application of proposed electrical analogy. Our approach mimics cyclic voltammetry and is applicable to other systems and electrodes.

4) The capacitance of the multi microchannel array was an order of magnitude smaller than the capacitance of polarizable NGEs. The capacitance of the NGEs increase with electrolyte concentration. However, capacitance of the multi microchannel array essentially remains constant with concentration variations. Electrical resistance of the multi microchannel array and NGEs both were influenced by the electrolyte concentration.

5) In terms of electrokinetic energy conversion, a maximum power of 1 mW obtained for 0 mM KCl electrolyte solution with 50 S conductivity. Addition of salt to electrolyte solutions lessened the system performance.

CHAPTER 6

SUMMARY AND FUTURE WORK

6.1 Summary

In this thesis, the underlying physics of streaming potential phenomena were explained and discussed in great details. In particular, the time-dependent behavior of fluid and electrical properties and the components contributed to evolution of streaming potential were considered and explained. The finite length microchannel selected in this work is a very genuine geometry and made the findings relevant to experimental results. It allowed the exploration of charge accumulation in inlet and outlet faces and observations of electrical properties in reservoirs. Moreover, observation of spatial variation in free charge density relative to the no flow, added to current understanding of streaming potential and provided a better picture of charge re-distribution. Based on a dimensional analysis a mathematical correlation developed to estimate the capacitance of a single microchannel. A simple, but effective equivalent electrical analogy proposed by incorporation of current, electrical resistance and capacitance of a microchannel.

The experimental exploration of this thesis was aimed to study the interactions between electrokinetic flows, electrodes and external circuits. Issues concerning streaming current technique were mentioned and electrokinetic energy conversion was considered in a specially made multi microchannel array coated with a nano-layer of gold on both faces. Findings were remarkable, for instance, the magnitude of maximum power and polarizability of NGEs were striking. The puzzled picture of streaming current measurements in porous media was solved by proposing practical approaches.

6.2 Future Work

6.2.1 Incorporation of Electrodes into Numerical Model

The full numerical model presented in this study was mainly employed for streaming potential simulation, namely, the open circuit mode. However, one needs to incorporate CMD equation, (convection, migration and diffusion) for electrodes and also accounts for electrochemistry at electrode-electrolyte interface to model the short circuit mode. By adding the electrodes into the problem issues such as electrode polarization can be addressed quantitatively. Moreover, electrokinetic energy conversion can be studied by adding a variable external resistance to such numerical model.

6.2.2 On the Electrical Analogy of Electrodes

It was shown that a capacitive-resistive circuit parallel to a current source is an equivalent electrical analogy for treatment of pressure driven flows in microchannels. Electrodes are mainly concern with current flows and charge accumulation and therefore naturally behavior of an electrode can be also addressed by a resistive-capacitive circuit. However, there are major differences between capacitance of a single microchannel and capacitance of an electrode. Further studies require to examine appropriateness of proposed analogy of an electrode and possibly to explore other equivalent electrical analogies.

6.2.3 Estimation of Streaming Currents using Magnetic Fields

Direct streaming current measurement, either in a single microchannel or in a multi microchannel array has been a challenge. In single microchannels magnitude of streaming currents is very small ($\approx pA$), therefore it is assumed that induced magnetic fields are negligible. However, in a multi microchannel array with relatively large number of pores (like current case study, 3,437,500 pores) streaming currents are in the order of $\approx mA$ and induced magnetic fields are possibly detectable. So the idea here was to detect magnetic fields of sufficiently large streaming currents and avoid direct streaming current measurements. The magnetic field strength around a current carrying wire is given by

$$B = \frac{m_0 I}{2\pi r} \tag{6.1}$$

where m_0 is the permeability if free space, B is the magnetic field strength, r is the distance from the wire and I is the current flowing through the wire. The current sensor employed in this study is an Integrated Parametric Current Transformer (IPCT) which works on the principle of the Direct Current, Current Transducer, DCCT and its current resolution is 100 times better than Hall-effect current sensors (see Fig.6.1). So far two experiments were performed employing this device, first, it was ensured that the IPCT measures the magnetic field induced by sum of low currents similar to streaming currents in a multi microchannel array. Second, it was shown that the ionic current namely streaming current does generate magnetic fields employing the IPCT. The experimental setup was placed (without the multi microchannel array) (see the

Figure 6.1: The Integrated Parametric Current Transformer (IPCT) employed in this study is a current sensor which works on the principle of the Direct Current Current Transducer, DCCT. Courtesy of GMW Associates, Inc.

inset in Fig. 4.3) through the aperture (69 mm) of IPCT. The setup then filled with 0 M KCL (ideally no free ions in the electrolyte solution). An external current of 1 mA applied across the setup using an external DC source and platinized platinum electrodes. No response recorded by IPCT *i.e.* no induced magnetic field as expected. However, by introducing an electrolyte solution of 1mM KCL (lots of free ions in electrolyte solution) into the setup, corresponding magnetic fields were detected by IPCT. Despite careful studies, we have not observed any magnetic field induced by streaming currents in the multi microchannel array and this needs further investigations.

6.2.4 Streaming Current Devices: What is next ?

On the basis of power density of the streaming current device ($\sim 1000W/cm^3$), such devices can possibly power lab-on-a-chips. We envisage that exploring the consequences of different electrolyte solutions and pore sizes on system performance are the next steps. One of the immediate suggestion is employing potassium fluoride; KF as working electrolyte solution. It is believed that F- does not chemisorb to the gold. Therefore, one might think electrode polarization substantially reduces and results in a better system performance.

BIBLIOGRAPHY

[1] Gad el Hak M. *The MEMS Handbook.* CRC Press, 2002.

[2] Harrison J. D., Fluri K., Seiler K., Fan Z. H., Effenhauser C. S., and Manz A. *Science*, 261:895–897, 1993.

[3] Zimmermann R., Osaki T., Schweib T., and Werner C. *Microfluidics and Nanofluidics*, 2:367, 2006.

[4] Li D. *Electrokinetics in Microfluidics.* Academic Press, 2004.

[5] Sbai M., Fievet P., Szymczyk A., Aoubiza B., Vidonne A., and Foissy A. *J. of Membrane Science*, 215:1–9, 2003.

[6] Pontie M., Chasseray X., Lemordant D., and Laine J. M. *J. of Membrane Science*, 129:125, 1997.

[7] Mak A. F. T. and Zhang J. D. *Journal of Biomechanical Engineering*, 123:66, 2001.

[8] Gross D. and Williams W. S. *Journal of Biomechanical Engineering*, 15:277, 1982.

[9] Raiman J., Hnninen K., Kontturi K., Murtomki L., and Hirvonen J. *J. Pharm. Sci.*, 92:2366, 2003.

[10] Beebe D. J., Mensing G. A., and Walker G. M. *Annual Review of Biomedical Engineering*, 4:261, 2002.

[11] Baker S. S. and Cull J. P. *Exploration Geophysics*, 35:41, 2004.

[12] Bryant I. D., Chen M., Raghuraman B., Navarro J., and Supp M. *SPE Annual Technical Conference*, page 102106, 2006.

[13] Revil A., Pezard P. A., and Glover P. W. J. *J. of Geophysical Research*, 104:20021, 1999.

[14] Jouniaux L., Bernard M. L., Zamora M., and Pozzi J. P. *J. of Geophysical Research*, 105:8391, 2000.

[15] Squires T. M. and Quake S. R. Microfluidics: Fluid physics at the nanoliter scale. *Reviews in Modern Physics*, 7:3:977–1026, 2005.

[16] Purcell E. M. Life at low reynolds number. *American Journal of Physics*, 45:3–11, 1977.

[17] Masliyah J. H and Bhattacharjee S. *Electrokinetic and Colloid Trasnport Phenomena*. Wiley, 2006.

[18] Hunter R . J. *Zeta Potential in Colloid Science*. Academic Press, 1981.

[19] Helmholtz H. L. F. *Wied.Ann*, 7:337, 1879.

[20] Yang J., Lu F., Kostiuk L. W., and Kwok D. Y. Electrokinetic microchannel battery by means of electrokinetic and microfluidic phenomena. *J. Micromech. Microeng*, 13:963, 2003.

[21] Yang J. and Kwok D. Y. Microfluid flow in circular microchannel with electrokinetic effect and navier's slip condition. *Langmuir*, 19:1047–1053, 2003.

[22] Yang J. and Kwok D. Y. Analytical treatment of flow in infinitely extended circular microchannels and the effect of slippage to increase flow efficiency. *J. Micromech. Microeng.*, 13:115–123, 2003.

[23] Gu Y. and Li D. *J. Colloid Interface Sci*, 226:328–339, 2000.

[24] Werner C., Korber H., Zimmermann R., Dukhin S., and Jacobasch H. *J. Colloid Interface Sci.*, 208:329–346, 1998.

[25] Schweiss R., Welzel P. B., Werner C., and Knoll W. *Langmuir*, 17:4303, 2001.

[26] Werner C., Zimmermann R., and Kratzmuller T. *Colloids and Surfaces A: Physicochemical and Engineering Aspects*, 192:205, 2001.

[27] Osaki T., Zimmermann R., Kratzmuller T., Schweiss R., and Werner C. *Langmuir*, 20:524, 2004.

[28] Roessler S., Zimmermann R., Scharnweber D., Werner C., and WorchKnight H. *Colloid and Surfaces B: Biointerfaces*, 26:387, 2002.

[29] Mala G. M., Li D. Q., Werner C., Jacobasch H. J., and Ning Y. B. Flow characteristics of water through a microchannel between two parallel plates with electrokinetic effects. *Int. J. Heat Liquid Flow*, 18:489–496, 1997.

[30] Levine S., Marriott J. R., Neale G., and Epstein N. Theory of electrokinetic flow in fine cylindrical capillaries at high zeta-potential. *J. Colloid Interface Sci.*, 52:136–149, 1975.

[31] Gortner R. A. and Briggs D. R. *Proc. Soc. Exper. Biol and Med.*, 25:820, 1928.

[32] Lachs H. and Biczyk J. *Z. Physik. Chem.*, 148A:441, 1930.

[33] Dubois R. and Roberts A. H. *J. Phys. Chem.*, 40:543, 1936.

[34] Erickson D., Li D., and Werner C. *J. Colloid Interface Sci.*, 232:186, 2000.

[35] Schweiss R., Welzel P. B, Werner C., and Knoll W. *Colloids and Surfaces A: Physicochemical and Engineering Aspects*, 195:97, 2001.

[36] Monaghan B. and White H. L. *J. Phys. Chem.*, 39:935, 1935.

[37] Broz Z. and Epstein N. *J. Colloid Interface Sci.*, 56:605, 1976.

[38] Wood L. A. *J. Of The American Chemical Society*, 68:437, 1946.

[39] Yang J. Lu F. and Kwok D. Y. *J. Phys. Chem. B*, 108:14970, 2004.

[40] Kirby B. J. and Hasselbrink E. F. Jr. *Electrophoresis*, 25:287, 2004.

[41] Osterle J. F. Electrokinetic energy conversion. *Journal of Applied Mechanics*, pages 161–164, June 1964.

[42] Rice C. L. and Whitehead R. *J. Phys. Chem.*, 69:4017, 1965.

[43] Morrison F. A. and Osterle J. F. Electrokinetic energy conversion in ultrafine capillaries. *Journal of Chemical Physics*, 43:2111–2115, Sept 1965.

[44] Burgrenn D. and Nakache F. R. Electrokinetic flow in ultrafine slits. *J. Phys. chem.*, 68:1084, 1964.

[45] Levine S., Marriott J., Neale G., and Epstein N. Theory of electrokinetic flow in fine cylindrical capillaries at high zeta-potentials. *J.Colloid Interface Sci*, 52:136, 1975.

[46] Michelmore A. P. and Hayes R. A. *PhysChemComm*, 6, 2000.

[47] Bard A. J. and Faulkner L. R. *Electrochemical Methods: Fundamentals and Applications*. John Wiley and Sons, 1980.

[48] Li D. Electro-viscous effects on pressure-driven liquid flow in microchannels. *Colloids and Surfaces A.*, 195:35–57, 2001.

[49] Renaud L., Kleimann P., and Morin P. *Electrophoresis*, 25:123, 2004.

[50] Bellaaistre M. C., Renaud L., Kleimann P., Morin P., Randon J., and Rocca J. L. *Electrophoresis*, 25:3086, 2004.

[51] Mitchell P. *Nature Biotechnology*, 19:717, 2001.

[52] Knight J. *Nature*, 418:474, 2002.

[53] Hunter R. J. *Introduction to Modern Colloid Science*. Oxford Science Publication, 1993.

[54] Probstein R.F. *Physicochemical Hydrodynamics: An Introduction (second ed.)*. Wiley, 1994.

[55] Russel W. B., Saville D. A., and Schowalter W. R. *Colloidal Dispersions*. Cambridge University Press, 1989.

[56] Smoluchowski M. V. *Bull. Int. Acad. Sci. Cracov.*, 8:182, 1903.

[57] Lewis A. F. and Myers R. R. The efficiency of streaming potential generation. *Journal of Phycial Chemistry*, 64:1338, Sept. 1960.

[58] Keh H. J. and Tseng H. C. Transient electrokinetic flow in fine capillaries. *J. Colloid Interface Sci.*, 242:450–459, 2001.

[59] Daiguji H., Yang P., and Majumdar A. Ion transport in nanofluidic channels. *Nano Lett.*, 4:137–142, 2004.

[60] Chang C. C. and Yang R. J. Computional analysis of electrokinetically driven flwo mixing in microchannels with patterned blocks. *J. Micromech. Microeng.*, 14:550–558, 2004.

[61] Gross R. J. and Osterle J. F. Membrane transport characteristics of ultrafine capillaries. *The Journal of Chemical Physics*, 49(1):228, 1968.

[62] Sasidhar V. and Ruckenstein E. *J. Colloid Interface Sci.*, 82:439, 1981.

[63] Sasidhar V. and Ruckenstein E. *J. Colloid Interface Sci.*, 85:332, 1982.

[64] Cwirko E. H. and Carbonell R. G. *J. Colloid Interface Sci.*, 129:513, 1989.

[65] Anderson J. L. and Malone D. M. *Biophys. J.*, 14:957, 1974.

[66] Deen W. M. *AIChE J.*, 33:1409, 1987.

[67] Donnan F. G. *J. Membrane Sci.*, 100:45–55, 1995.

[68] Smit J. A. M. *J. Colloid Interface Sci.*, 132:413, 1989.

[69] Basu S. and Sharma M. M. *J. Membr. Sci.*, 124:77, 1997.

[70] Starov V. M. Hall M. S. and Lloyd D. R. *J. Membr. Sci.*, 128:23, 1997.

[71] Nakao S. Tsuru T. and Kimura S. *J. Chem. Eng. Jpn.*, 24:511, 1991.

[72] Bhattacharjee S., Chen J. C., and Elimelech M. *AIChE J.*, 47:2733, 2001.

[73] Mansouri A., Bhattacharjee S., and Kostiuk L. W. *J. Physical Chemistry B*, 2007. In press.

[74] White F. M. *Fluid Mechanics*. McGraw-Hill, 2005.

[75] Heyden V., Frank H., Stein D., and Dekker C. Streaming currents in a single nanofluidic channel. *Physical Review Letters*, 95:116104, 2005.

[76] Ueda M., Takamura Y., Horiike Y., and Baba Y. *Jpn. J. Appl. Phys.*, 41:1275, 2002.

[77] Erickson D. and Li D. *J. Colloid Interface Sci.*, 237:283, 2001.

[78] Stein D. Heyden F. H. J. van der and Dekker C. *Physical Review Letters*, 95:116104, 2005.

[79] Chai J., Lu F., Li B., and Kwok D. Y. *Langmuir*, 20:10919, 2004.

[80] Werner C., Konig U., Augsburg A., Arnhold C., Korber H., Zimmermannb R., and Jacobasch H. *Colloid and Surfaces A*, 159:519, 1999.

[81] Gochin R. J. Alkafeef S. and Smith A. L. *Colloids and Surfaces A: Physicochemical and Engineering Aspects*, 195:77, 2001.

[82] Randles J. E. B. and Somerton K. W. *Trans. Faraday Soc.*, 48:937, 1952.

[83] Elimelech M., Chen W. H., and Waypa J. J. *Desalination*, 95:269, 1994.

[84] Van Den Hoven TH. JJ. and Bijsterbosch B. H. *Colloids and Surfaces*, 22:171, 1987.

[85] Van Der Linde AJ. and Bijsterbosch B. H. *Colloids and Surfaces*, 41:345, 1989.

[86] Canning J., Buckley E., Huntington S., and Lyytikainen K. Using multi-microchannel capillaries for determination of the zeta potential of a microfluidic channel. *Electrochimica Acta*, 49:3581, 2004.

[87] Hurd R. M. and Lane R. N. Principles of very low-power electrochemical control devices. *J. of the Electro-Chemical Society*, 104:727, 1957.

[88] Osterle J. F. Electrokinetic energy conversion. *Journal of Applied Mechanics*, page 161, June 1964.

[89] Heyden V., Bonthuis D. J., Stein D., Meyer C., and Dekker C. Power generation by pressure-driven transport of ions in nanofluidic channels. *Nano Lett.*, 7:1022, 2007.

[90] Daiguji H., Oka Y., Adachi T., and Shirono K. Theoretical study on the efficiency of nanofluidic batteries. *ELECTROCHEMISTRY COMMUNICATIONS*, 11:1796, 2006.

[91] Heyden V., Bonthuis D. J., Stein D., Meyer C., and Dekker C. Electrochemomechanical energy conversion in nanofluidic channels. *Nano Lett.*, 10:2232, 2006.

[92] Olthuis W., Schippers B., Eijkel J., and Van den Berg A. Energy from streaming current and potential. *Sensors and Actuators B: Chemical*, 111-112:385, 2005.

[93] Lu M., Satyanarayana S., Karnik R., Majumdar A., and Wang C. A mechanical-electrokinetic battery using a nano-porous membrane. *J. Micromech. Microeng.*, 16:667, 2006.

[94] Rastgol R. P., Srivastava R. C., and Singh S. N. Nonequilibrium thermodynamics of electrokinetic phenomena. *Chemical Reviews*, 93:1945, 1993.

[95] Alkafeef Saad F. and Alajmi Abdullah F. *J. Colloid Interface Sci*, 309(2):963, 2007.

[96] Skierczynska J., Spiewla E., Zolnierczuk R., Bulanda W, and Wardak A. The measurements of the membrane resistance of characeae by alternating and direct currents. *J. of Experimental Botany*, 24:1015, 1973.

[97] Paradiso J. A. and Starner T. Energy scavenging for mobile and wireless electronics. *Pervasive Computing, IEEE*, 4:18, 2005.

[98] Novotill S. Solar-powered motor runs on 10 na. In *EDN Magazine*. March 2004.

[99] Daiguji H., Yang P., Szeri A. J., and Majumdar A. Electrochemomechanical energy conversion in nanofluidic channels. *Nano Lett.*, 12:2315, 2004.

[100] Canning J., Buckley E., and Lyytikainen K. Electrokinetic air - silica structured multi - microchannel capillary batteries. *Electronics Letters*, 40:298, 2004.

[101] Chun M. S., Lee T. S., and Choi N. W. Microfluidic analysis of electrokinetic streaming potential induced by microflows of monovalent electrolyte solution. *J. Micromech. Microeng*, 15:710, 2005.

[102] Lee T. S., Chun M. S., Choi D. K., Nam S. W., and Lim T. H. The electrokinetic microfluidic flow in multi-channels with emergent applicability toward micro power generation. *Korean Journal of Chemical Eng.*, 22:528, 2005.

[103] Chun M., Lee T., and Choi N. Microfluidic analysis of electrokinetic streaming potential induced by microflows of monovalent electrolyte solution. *J. Micromech. Microeng.*, 15:710, 2005.

[104] Myung-Suk Chun, Min Suk Shim, and Nak Won Choi. Fabrication and validation of a multi-channel type microfluidic chip for electrokinetic streaming potential devices. *Lab on a Chip*, 6:302, 2006.